TECHNISCHE UNIVERSITÄT MÜNCHEN

Lehrstuhl Für Nanoelektronik

Nanodiodes and Nanoantennas Fabricated by Transfer Technology

Mario Bareiß

Vollständiger Abdruck der von der Fakultät für Physik der Technischen Universität München zur Erlangung des akademischen Grades eines

Doktors der Naturwissenschaften

genehmigten Dissertation.

Vorsitzende:

Univ.-Prof. Dr. Nora Brambilla

Prüfer der Dissertation:

1. Univ.-Prof. Paolo Lugli, Ph.D.
2. Prof. Dr. Wolfgang Porod,
   University of Notre Dame, Indiana/USA

Die Dissertation wurde am 10.10.2012 bei der Technischen Universität München eingereicht und durch die Fakultät für Physik am 05.11.2012 angenommen.

Zusammenfassung der Doktorarbeit

Im Rahmen der vorliegenden Doktorarbeit wurde ein optoelektronisches Bauteil zur Absorption von Infrarotstrahlung entwickelt und gefertigt. Das Bauteil wird aus einer großflächigen Anordnung von ungefähr 1 Millionen Nanoantennen und nochmal ein Drittel so vielen AC/DC Wandlern gebildet, die den induzierten hochfrequenten Strom gleichrichten sollen. Um eine solche große Anzahl von Antennen und Gleichrichter herzustellen wurde zudem eine Fertigungstechnologie entwickelt, die auf eine Drucktechnik basiert nämlich dem Nanotransfer printing. Es wurde ein Konzept für die Anordnung der Antennen und der Gleichrichter, die von quantenmechanischen Metall-Isolator-Metall (MIM) Tunneldioden gebildet werden, unter Bezugnahme der Fertigungsmöglichkeiten erarbeitet. Die Einzelkomponenten wurden bezüglich ihrer Geometrie und Materialien untersucht und optimiert. Das System von Antennen wurde derart ausgelegt, dass eine Absorption von Infrarotstrahlung bei 10,6 µm optimiert ist und demzufolge mussten die MIM Tunneldioden eine "cut-off" Frequenz bei mehreren zehn Terahertz besitzen. Dies wurde ermöglicht indem die Abmessungen der Dioden unterhalb von 100 nm waren. Mittels moderner Technologien konnten wir die Einzelkomponenten fertigen und untersuchen. Das optoelektronische Bauteil konnte erfolgreich auf ein Glassubstrat gedruckt und mittels eines CO_2 Lasers untersucht werden. Im Rahmen unserer Untersuchungen entdeckten wir, dass ein thermischer Effekt, nämlich der Seebeck Effekt für die Rektifizierung verantwortlich ist. Für zukünftige Forschungsgruppen ermöglich diese Erkenntnis eine Vereinfachung der konzeptionellen Auslegung des Bauteils, da auf die aufwendige Herstellung von Dünnschichtisolatoren verzichtet werden kann.

Abstract

In the frame of the present Ph.D. thesis, we designed and fabricated an optoelectronic device suitable for absorbing infrared light. The device consists of a large area arrangement of almost 1 million nanoantennas and in addition one third of this amount of AC/DC converter which are supposed to rectify the induced current. In order to manufacture such a high amount of antennas and rectifiers, we developed a new fabrication method based on a printing process, namely nanotransfer printing. A concept for the arrangement of the antennas and the rectifiers which consist of a quantum mechanical metal-insulator-metal (MIM) tunneling diode within the device with respect to the fabrication possibilities has been designed. The single components were optimized with respect to their geometry and the materials. The system of the antennas was design in such a way that the absorption of infrared light at 10.6 µm is optimized and thus, the MIM tunneling diodes had to feature a cut-off frequency in the several tens of terahertz regime. This was possible when the dimensions of the diodes were below 100 nm. Using modern technologies, the single components were fabricated and characterized. The optoelectronic device was successfully transfer printed on a glass substrate and investigated using a CO_2 laser. In the frame of our investigations, we found that thermal effect, namely the Seebeck effect is responsible for the rectification. For future research groups, this knowledge enables a simplification of the concept of such a device, since the challenging fabrication of the ultra-thin insulator can be omitted.

Contents

Chapter 1

Introduction

Nowadays, infrared (IR) light is an important spectral regime in medical, safety and energy applications [1–3]. However when using semiconductor materials for absorbing IR light, either the photon energy is too low to create excitons (e.g. in commercially availible Si photodetectors), or the devices are relatively expensive (e.g. photodetectors based on low-bandgap semiconductors, such as In(Ga)As) [4] and are helium-cooled. State of the art bolometers represent alternative devices that are able to detect IR radiation. However, bolometers lacks in spectral resolution, since a temperature induced resistivity change of a current through an irradiated conductor is detected. In addition bolometers are active devices and needs a power source. Photovoltaic is one of the most important renewable energy sources, however, in commercial Si technology the absorption range is limited because of the bandgap of 1 eV of silicon. In order to extend the absorption spectrum to the infrared range, efficient IR absorbing devices are required. A hybrid photovoltaic devices consisting of a conventional Si solar cell and a new IR absorbing device that increase the efficiency of the solar cell is a new concept in order to become more compatible to recent conventional energy sources.

We present here a new IR sensitive device that overcomes the drawbacks of infrared devices of the state of the art, namely an array of nano antennas coupled to high frequency rectifying devices. Indeed, these detectors offer full compatibility with complementary metal oxide semiconductor (CMOS) technology as well as high-speed and uncooled room-temperature operation. Electro-optical investigation reveal the outstanding antenna response that is similar to the best infrared antennas in the world and that the sophisticated design of the antenna array overcomes challenge with respect to destructive interferences within the array. Since infrared light features frequencies in the terahertz (THz) regime, the electrical currents that are induced in the antennas have the same high frequencies. For detecting these high alternating currents (AC), a rectifying device have to be included in the antennas. We present

here two devices that fullfil these requirements, a metal-insulator-metal (MIM) tunneling diode and thermo-couple based on the Seebeck effect.

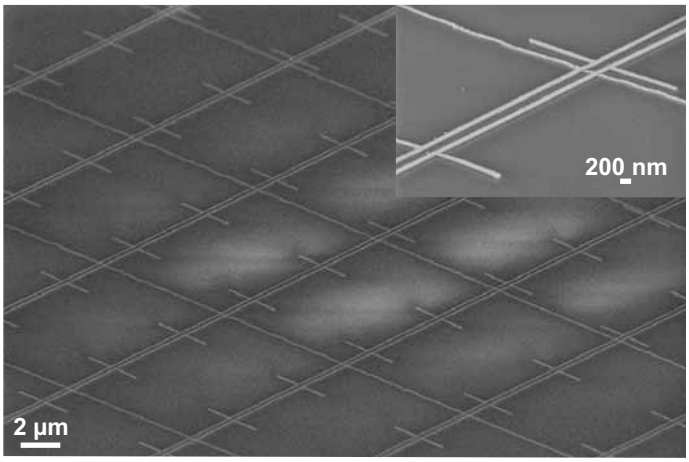

Figure 1.1: Scanning electron microscope image of transfer-printed nano antenna array. A zoom of one antenna including tunneling diodes is also shown.

In this work, a main focus has been set on MIM diodes, since they represent outstanding devices that are important in various electronic and optoelectronic fields besides the IR detection, like emission cathodes [5] and switching memories [6]. Of particular interest are devices operating at a few THz, a frequency range where sensing and communication are particularly attractive. Other applications of THz devices involve biomedical investigation of DNA or enzymes [7]. Several spatial designs of MIM diodes are presented and several solid and organic materials were investigated in order to build the most efficient device [8]. We used a new material fabrication method for manufacturing ultra-thin and high quality dielectric materials that features a thickness in the range of 2 to 4 nm.

All electronical and optoelectronical devices in the present work have been fabricated in a novel and highly efficient process, namely a nano transfer printing process (nTP). Nowadays, the state of the art fabrication method in CMOS technology is optical lithography. However, the word "optical" is used in this field for traditional reasons. Though in research ultra violet (UV) light near the optical wavelength regime (400-800 nm) is still the state of the art, in industry fabrication, the wavelength is far off this regime. In 2009, the company AMSL designed a mass production lithography machine working in the extreme UV (EUV) which provides a beam featuring a wavelength of 13.5 nm when reaching the surface of a sample. At universities or similar research institutes, the costs for EUV-setups including the lenses and other components suitable for such high photon energies are too high. Although, companies in chip industry are willing

to pay billions of dollars for such systems, a cost efficient alternative is required for nanoscale device fabrication.

Electron beam lithography [9] does not provide a suitable alternative in CMOS production technology, since in this technique every feature is fabricated individually. Consequently, the throughput is too low and thus the costs are even higher than using the EUV optical lithography.

We present here a new nano transfer printing method which provides a compatible nanoscale fabrication method that solves all named drawbacks of the optical and electron beam lithography. Additionally, the fabrication of nanoscale devices with nTP is a dry process that avoids the use of polymers, and even any type of solvents or chemicals can be omitted. The basic principle of nTP is the use of a stamp featuring 3-dimensional structures that has materials, stack of metals or devices thereon and a substrate, e.g. a CMOS chip, on which these structures are transferred directly. Since a whole array of devices can be fabricated over a large area of a target substrate with one simple step, the fabrication speed is very high. The stamp is than recycled and used several times which makes this process very cost efficient. It turns out that the key parameter in this fabrication method is the temperature which effects interfacial molecular structuring. By tailoring this parameter, we were able to fabricate single and multiple layers of several conductive and non-conductive material features. The applications for nTP-fabricated structures are numerous and include the fields of semitransparent electrical contact grids [10], cross bars in switching memories [11], optical and magnetic quantum dots [12], antennas [13] and many more [14, 15].

In this thesis, we show that the fabrication of nano antenna arrays and metal-insulator-metal diodes with nTP is beneficial with term of the fabrication yield and that the devices show an excellent electronical and optoelectronical performance. Indeed, the working range of the devices is not limited to the infrared regime. In fact, by amending the spatial dimensions of the antennas, the sensitive range can be shifted to other wavelengths. With respect to the new fabrication method, namely nano transfer-printing, a fast and efficient method is presented to fabricate precisely classical and quantum devices in various fields of nanoelectronics.

Chapter 2

State of the art

In this chapter, a brief overview of the state of the art of nanotechnology and infrared devices is given. Several fabrication methods like optical lithography and electron beam lithography are evaluated and a motivation for the novel nanotransfer printing technique is given. Further, state of the art infrared devices are presented and compared.

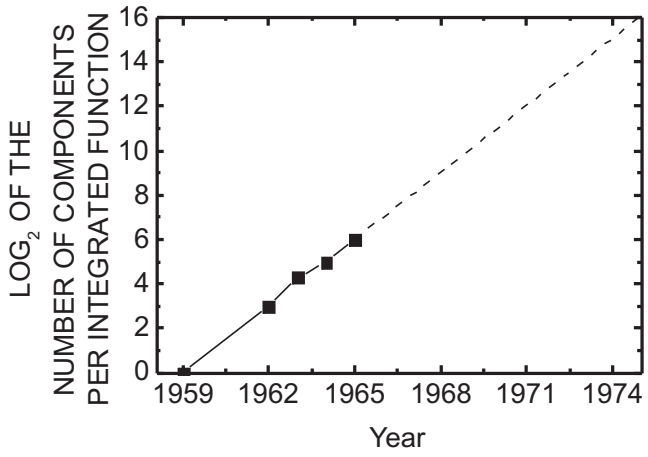

Figure 2.1: Based on just a few data points, shown in the plot above, Gordon Moore accurately predicted in 1965 that the number of components on an IC would double every year for the next 10 years-a prediction that became known as Moore's Law [16].

In 1947, the invention of the transistor by William Shockley and his colleagues Bardeen and Brattain started a new era in the world of electronics [17]. Companies started to build integrated circuits (IC) by including transistors, and nowadays, computers without these devices are unimaginable.

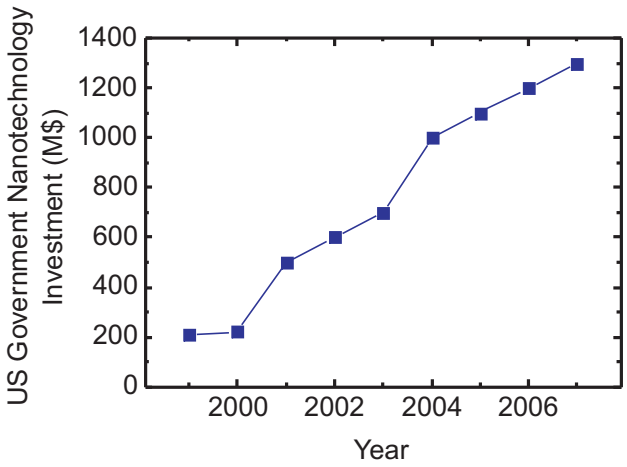

Figure 2.2: The historical growth of the National Nanotechnology Initiative [23].

In the sixties, Gordon E. Moore then R&D director at Fairchild Semiconductor and a former colleague of Shockley quantified in a formula the growth of the number of semiconductor in a simple formula. He recognized that manufactures had doubled the amount of components in integrated circuits (IC) in regular intervals (Figure 2.1) [18]. In order to increase the capabilities of e.g. computers or mobile phones, the memory density and thus the device density in ICs has to be increased continuously as predicted by Moore´s law [19]. Since the dimensions electronic of devices are usually limited, the size of integrated transistors or other devices in ICs has to be scaled down. In the late sixties, the transistor size was 100 µm [20]. In nowadays, channel width and lengths in transistors in the range of a few nanometers are achieved in research [21], and industrial companies such as IBM, Intel, Toshiba and AMD also entered the field of nanotechnology and use extreme ultraviolet (EUV) light source in order to fabricate 22 nm nodes [22]. The importance of the nanotechnology is proven by the fact the US National Nanotechnology Initiative has allocated more than 1.2 B$ for 2007 the budget (Fig. 2.2) [23].

In order to be able to fabricate nanoscale devices, several fabrication steps are needed. The most promising fabrication technology in industry is the optical lithography to which also the EUV lithography counts. The first practice of optical lithography is attributed to *Niepce*, who discovered in 1852 that certain types of asphalt are sensitive to ultraviolet radiation. He applied these materials to the etching of metallic decorations [24]. Although industry uses expensive optical lithography systems for the fabrication of nanoscale structures, in research this technology is in general used for structuring surfaces in microscale regime [25] at a few micrometer at the best. Using this technique, polymer masks are

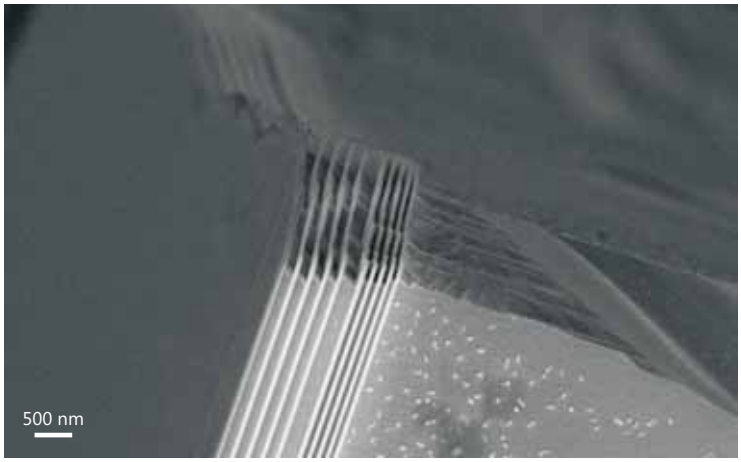

Figure 2.3: Image of a MBE grown stamp suitable for NIL

produced on various substrates which allows selective etchings or targeted metal deposition on the substrates. Indeed, not only bare substrates, such as Si wafers, can be structured using optical lithography, but also thin layers like carbon nanotubes (CNT) layers [26], organic layers [27], or oxides [28] can be partly removed.

Electron beam lithography is a more precise technique for patterning surfaces featuring a higher resolution in the nanoscale regime [29, 30]. However, since every structure that is produced has to be written individually by the electron beam, this manufacturing method is expensive and slow and thus not used in high throughput semiconductor production in industry [31]. However, because of its flexibility this approach is heavily used in research for the investigation of individual prototype devices.

An alternative, high throughput, low-cost and fast fabrication method in nanotechnology which is not yet established in semiconductor industry is the nanoimprint lithography (NIL). In 1995, *Chou* presented for the first time a successful fabrication of 25 nm structures using this novel approach [32]. As claimed in these initial publications, NIL was a further development of the compression molding technology used in Compact Disk manufacturing that was used in this large scale manufacturing but was not employed in semiconductor fabrication. In the NIL process, an imprint mold is fabricated using conventional technologies, such as electron beam lithography and etching techniques. The topography of the mold is then transferred by imprinting into a resist layer prepared on the substrate. Subsequent etching steps allow the transferring imprinted patterns from the polymer layer into the substrate [23]. Several types of stamps have been designed since than including Si wafer stamps [33],

molecular beam epitaxy (MBE) grown stamps (Fig. 2.3) [34], carbon nanotubes stamps [35] or flexible PDMS stamps [36]. Although this technology is not yet implemented in semiconductor nanotechnology, in 2003 the International Technology Roadmap for Semiconductors (ITRS) also announced the inclusion of NIL onto their roadmap as a candidate technology for future IC production [37].

So far, we described the several fabrication methods in semiconductor technology and nanoelectronics based on top-down methodologies [38]. Nanoelectronics obtained through the bottom-up approach of molecular-level control of material composition and structure may lead to devices and fabrication strategies not realizable with top-down methods [39]. Self-assembled monolayers (SAM) [40] and DNA-based devices like transistors [41, 42] are prominent representatives for top-down methods. In the case of SAM, electronic devices can be fabricated taking advantage of the fact that the SAMs are self-assembling on a surface, and can form in this way e.g. a nanometer thin dielectric layer [43].

Nanotransfer printing (nTP) is novel semiconductor fabrication technology that takes advantage of both concepts, namely the top-down and bottom-up. The dimensions of the structures and devices that are manufactured with this technique vary between centimeter [44] and nanometer [45]. In this technique, either rigid stamps [2] or flexible PDMS stamps [46] are used. A rigid stamp is usually fabricated via optical lithography or electron beam lithography in order to reach 3-dimensional structures on the surface of the stamp. Metals and insulators are deposited on the stamp and directly transfer printed on target substrate. The main advantage with respect to conventional top-down fabrication methods is that a photoresist or any other polymer is not required. In general, the whole fabrication process of nanoscale devices can be accomplished without the need of any chemicals or liquid solvents [7]. SAM can be placed on the target substrate prior transferring which either can increase the adhesion to the materials to be transferred and can also serve as a dielectric [47]. In addition, SAM are also used to form an anti-adhesion coverage on the stamps which promotes the transfer process. In this way, nanotransfer printing combines the advantages of both semiconductor fabrication methodologies and represents a fast and low-cost fabrication method suitable for nanoelectronics. Indeed, in the case when multiple nTP steps are needed for the fabrication of a device, the alignment to structures that are already transfered onto the substrate is challenging.

So far, we gave an overview of the most important nanoscale fabrication methods in semiconductor technology. Further, we explained that downscaling is an important issue in the field of transistors. But also in optics, nanostructures and nanodevices are required. The applications are numerous in the fields

of quantum cryptography where single photon source have to be fabricated featuring nanostructures [48], organic light sources [49], detectors for sensing applications [50], or data transfer [51].

Recently, the need for infrared (IR) detectors increased since this important spectral regime is useful in medical, security, and energy applications [4]. In terms of security, infrared sensors were installed in a high amount during the past years [52]. These optoelectronic devices are able e.g. to look for hidden weapons under clothes and also explosives which feature absorption lines in the infrared range [53]. Also with respect to night vision cameras, infrared detectors are useful since heat dissipated by a specie can be detected without the need for light in the optical range [54]. For energy applications, solar cells are the state of the art devices absorbing energy from light irradiated by sun, and convert it into electrical power [55]. However, in conventional Si solar cells the absorption range is limited because of the physical properties of Si, namely the bandgap [3]. The combination of an infrared absorbing device with a conventional Si solar cell can increase the overall cell efficiency.

Table 2.1 gives a comparison of IR detectors. In general, infrared sensor can be divided into two main categories: sensors that are sensitive to the wavelength of light (temperature based sensors), and sensors that convert photons (particles) into a signal [56]. There are several advantages and disadvantages in the two types of sensors. The main advantages in temperature-based detectors, such a bolometers [57], is their low-cost fabrication, their operation at room temperature and their CMOS compatibility. In contrast, photonic based detectors feature the opportunity of selecting a high amount of materials which makes bandgap tailoring easy.

In 1968, a new infrared sensor based in the wavelength nature of light has been proposed by the group of *Javan* [58], namely a rectenna. This sensor combines an antenna with a high-frequency rectifier, namely metal-insulator-metal (MIM) tunneling nanodiode. A MIM diode consist of a thin dielectric (a few nanometers thick) sandwiched between two metal electrodes. When an external bias is applied on the diode, the electronic current flowing from one electrode to the other one is different than in the reversed due to the nonlinear I-V characteristics [59]. In the case that different metals featuring a different work function are used, the current in forward and reverse polarity is asymmetric even around zero volts [60]. The area of the diode must be in the nanoscale regime in order to feature a cut-off frequency in the terahertz range [61]. In summary, a rectenna feature an antenna that absorbs the electromagnetic wave and a MIM diode which is able to convert the induced terahertz currents into DC. In the case of a MIM diode with dissimilar work functions, the infrared absorber works even as an unbiased device. Up to now, only single rectennas have been

demonstrated [62].

Detector type	Advantages	Disadvantages
Thermal	Light, rugged, reliable, and low cost	Low detectivity at high frequency
	Room temperature operation	Slow response (ms)
Photon		
Intrinsic		
IV-VI	Available low-gap materials	Poor mechanical
	Well studied	Large permittivity
II-VI	Easy band-gap tailoring	Non-uniformity over large areas
	Well-developed theory and exp.	High cost in growth and processing
	Multicolor detectors	
III-V	Good material and dopants	Heteroepitaxy with large latt. mismatch
	Advanced technology	
	Possible monolithic integration	
Extrinsic	Very long wavelength operation	Low temp. operation
	Relatively simple technology	
Free carriers	Low cost, high yields	Low quant. efficiency
	Large and close packed 2D arrays	Low temp. operation
Quantum wells		
Type I	Matured material growth	Low quant.efficiency
	Good uniformity over large areas	Complicated design and growth
	Multicolor detectors	
Type II	Low Auger recombination rate	Complicated design and growth
	Easy wavelength control	Sens. to interfaces

Table 2.1: Comparison of infrared detectors [56, 63]

In fact, based on the state of the art infrared sensors, a rectenna array that is sensitive in the infrared regime has not been realized prior this work [62]. Such arrays could lead to promising applications in the field of high resolution infrared detectors or in the field of energy harvesting, when light irradiated by the sun is converted to electrical power [64]. In order to be compatible to recent infrared sensor technologies, the fabrication of these rectenna arrays must be in a fast and low-cost way. Therefore, nanotransfer printing is here the fabrication technique of choice. Large arrays of devices can be printed within one process step over large areas. Even thin dielectric layers feature are not loosing their quality after the printing process [65]. The high-yield fabrication of large area rectenna arrays with nanotransfer printing is a novel fabrication method that is promising for future infrared applications.

Chapter 3

Fabrication methods

Several physical and chemical fabrication methods were used in this work. The technical details of the most important processes are briefly explained here. The detailed process parameters are given in the appendix A–C.

3.1 Thermal Evaporation

The deposition of materials such as metals or insulators onto a target substrate via evaporating the material is called evaporation. In this work, the materials were placed into a boat which is heated by a current. This technique of evaporation is called thermal evaporation.

The UNIVEX 350G High Vacuum Experimentation Systems from Leybold is the metal deposition machine that was mainly used in the present work. This thermal evaporator is located inside a Glovebox guaranteeing a Nitrogen 5.0 atmosphere. Since the amount of oxygen and water is decreased to less than one part per million, oxidation and degradation of devices is avoided. Another advantage with respect to the process speed, is the decrease of the pump time in order to reach a suitable vacuum. Evaporation is usually done at pressures around $1 \cdot 10^{-6}$ mbar. The pump time in oder to reach this high vacuum is around 5 min. A high vacuum is necessary during evaporation since metals that are not noble, especially Al, would oxidize during metal deposition. This would lead to a high resistivity.

The evaporator features two individual pockets for two boats, so two different materials can be deposited one after another without the need for opening the evaporation chamber. The boats, consisting of tungsten or molybdenum, are filled with a metal of choice and the substrate is placed topside down over the boats in a holder. The holder can be rotated with different speeds in order to guarantee a homogeneous metal coverage of the substrate. Since the holder

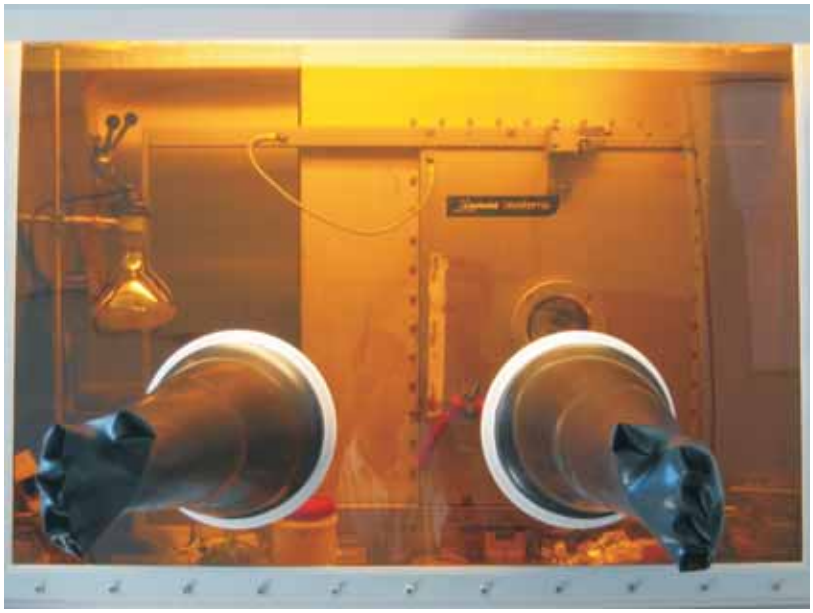

Figure 3.1: Photograph of UNIVEX 350G: The thermal evaporator is located inside a glovebox in order to guarantee a nitrogen atmosphere. Oxidation of metals or degradation of polymers is slowed.

can also be tilted, the deposition of metals under different angles is possible. Using this technique, shadow evaporations on the nanoscale size are possible [66].

After reaching the target pressure for metal deposition, a current usually between 160 A and 300 A is flowing through the boats and heat them, and the metals that are placed therein to temperatures above the boiling point of the metals. Two shutters, one above the sources and one below the substrate, are controlled remotely. The first shutter above the sources is opened and the deposition rate is measured with an oscillating quartz crystal. After the target deposition rate is reached (rates between 0.4 Å/sec and 10.0 Å/sec) the second shutter below the substrate is opened and a feedback guarantees a constant deposition rate. Once the target sheet thickness is reached, both shutters close automatically and the heating current is decreased slowly. The chamber can then be opened and the substrate comprising the deposited metal layers can be taken out.

Important material combinations are briefly discussed here. Since Au an Pt are noble metals and thus feature a low reactivity, the adhesion on substrates is generally very weak. Therefore, adhesion promoter are co-deposited in order to provide a good adhesion of said materials. These are mainly Ti, Cr or Al, wherein the latter one provides the least adhesion of the three materials. For the

printing processes that will be discussed later, the inverted layer arrangement is advantageously. There, first a layer of Au is deposited on a stamp and than the adhesion promoter in order to get easily rid of the materials from the stamp and transferred onto a target substrate.

In order to cover only certain areas on a substrate with metals during evaporation, parts can be covered by a metal plate or a plastic foil which is called a shadow evaporation. A photoresist is structured on the substrate featuring windows in the range of a few micrometers or nanometers where the deposited metals can directly be placed in the surface. After removing the resist, namely a lift-off process, only the metals that could reach the surface remain and thus only certain areas are covered with metals.

3.2 Sputtering

Another possibility of depositing materials onto a target substrate is sputtering. This deposition technique is faster than evaporation since a non-high vacuum is required and the deposition rates are faster. A solid target is cannonade by ions and material is sputtered from the solid material in the chamber onto the target substrate.

In the present work, a sputter machine of the company JEOL was used. The purpose was mainly to cover surfaces with a thin conductive layer for investigations with a scanning electron microscope (SEM) (see section 4.4). A sample is placed in a chamber under a metal target, namely gold. After evacuation, argon as a process gas is introduced in the chamber. After applying an electric field, the argon atoms are ionized. The Ar-ions are accelerated on the gold target, and gold is deposited from the target on the surface of the sample. The pressure in the chamber is around 0.1 mbar. This process features the advantage of high speed, but the surface roughness of the deposited materials is higher than with an evaporation system.

3.3 Lithography

The lithography process is the standard process to pattern certain areas of a flat surface. First, a polymer that is located on a substrate is patterned. Afterwards, the whole surface can be treated with wet chemicals, or can be exposed to ions for etching. The patterned polymer protects parts of the substrate. After removing the polymer, the surface of the substrate is patterned.

3.3.1 Optical lithography

A plane substrate, e.g. Si wafer or glass, is placed on a spincoater and covered with a photoresist using a syringe. Depending on the rotation speed, the thickness of the photoresist on the substrate can be tailored. In order to provide a good adhesion between the substrate and the polymer during spin coating, the substrate can be covered by an organic adhesion promoter, namely a self-assembled monolayer, or activated by a brief plasma treatment. After spincoating, the substrate comprising the photoresist is placed in a maskaligner and covered with a mask. After exposing the photoresist, the portions of the photoresist exposed to light are chemically changed. This makes the exposed areas either soluble (for "positive" resists) or non-soluble (for "negative" resists) to a certain developer depending if a positive or negative photoresist is used, respectively.

Positive photoresists are used when, in a subsequent step, the surface is treated with a wet chemical or exposed to reactive ion etching, since the edges of the resist do not feature an undercut (see Figure 3.2). In wet chemical processes, an underetching of the structures is avoided. Negative photoresists are used for lift-off processes, since the undercut guarantees that the metals in the substrate and on the resist are not connected.

3.3.2 Electron beam lithography

Electron beam lithography (EBL) has the same process steps than optical lithography for the coverage of the substrate with a polymer. The exposure of the resist is here done by an electron beam and the features are directly written into the polymer. The development of the resist is similar to the optical lithography. Small structures below 10 nm can be realized in the polymer and in a subsequent process step transferred in the target substrate. Since this fabrication method lacks in speed and is expensive, the state of the art fabrication method in semiconductor industries is still the optical lithography.

3.4 Nanoimprint lithography

Nanoimprint lithography (NIL) is a relatively new fabrication technology which seems to compete with the conventional fabrication methods such as OL or EBL. Usually, the feature size of structures that can be fabricate with OL is limited due to the wavelength of the UV light. Using additional processes invoking masks and lenses, resolutions well below the UV-sources wavelength can be reached, but at high costs. EBL overcomes the challenge with respect to the possible feature size, however, this fabrication method lacks in cost and speed efficiency. NIL represents a solution for both, fabrication of nanostructures

Figure 3.2: Optical lithography process is schematically shown. A substrate (black, e.g. Si) comprising an additional layer (gray, e.g. SiO_2) is covered by a photoresist (green, e.g. positive resist). By illuminating the photoresist through a mask, certain areas of the resist are exposed, and chemically changed. In the case of a positive resist, the exposed areas become soluble in a developer (usually a base). This creates a window in the resist and further structuring of the surface can be done, like chemically etching of the additional layer. After removing the remaining resist in e.g. acetone, a microscale structured surface is obtained.

and cost efficiency. The basic technology and the common techniques for the fabrication of stamps are described below.

3.4.1 Concept of nanoimprint lithography

The initial step of NIL is similar to OL and EBL. A plane substrate is covered e.g. via spincoating with a polymer. The usual thickness of the resist is between 100 nm and 400 nm. After a softbake, the substrate is placed into a nanoimprinting machine and a stamp featuring a structured surface is placed thereon. In general, NIL processes can mainly be divided into two categories which are presented in the following sections.

Thermal NIL: The polymer on the substrate is heated above its glass transition temperature. In this way, the imprint polymer becomes liquid. Usual glass transition temperatures are around 160°C. Then, the stamp is pressed against the substrate featuring the plastic resist at a given pressure for a specific time. The polymer is than cooled down below its glass transition temperature while still applying the pressure. After cooling down, the applied pressure is decreased until zero bar and the features of the stamp are transferred into the imprint resist.

Ultra-violet (UV) light NIL: Instead of heat, an UV-sensitive crosslinker is used in the imprint polymer. After placing the stamp and the substrate in the nanoimprinting machine over each other, the pressure is directly applied and a UV source is switched on. The UV sensitive crosslinker cures the polymer resist and the structures remain in the polymer after demolding. Since in this process the polymer has to be exposed to UV light, at least a transparent substrate, such as glass, or a transparent stamp, such as a quartz stamp, have to be used.

Figure 3.3 shows the main steps of both imprint techniques. First an imprint polymer is deposited onto a suitable substrate. When performing thermal NIL, the polymer is heated up above its glass transition temperature. No heating is necessary in a UV based NIL process. The second step comprises the pressing of the stamp featuring the desired patterns into the polymer which is partly deformed and partly compressed. After that, the polymer is cured by either cooling down (thermal NIL) or by UV radiation and the structures are transferred into the hard polymer. However, even when using a stamp featuring structure heights that are larger than the polymer thickness on the substrate, the whole polymer underneath the stamps while imprinting is not eliminated. The remaining layer of the resist, called "residual layer", has a thickness around 5–10 nm and is removed in a subsequent brief oxygen plasma treatment.

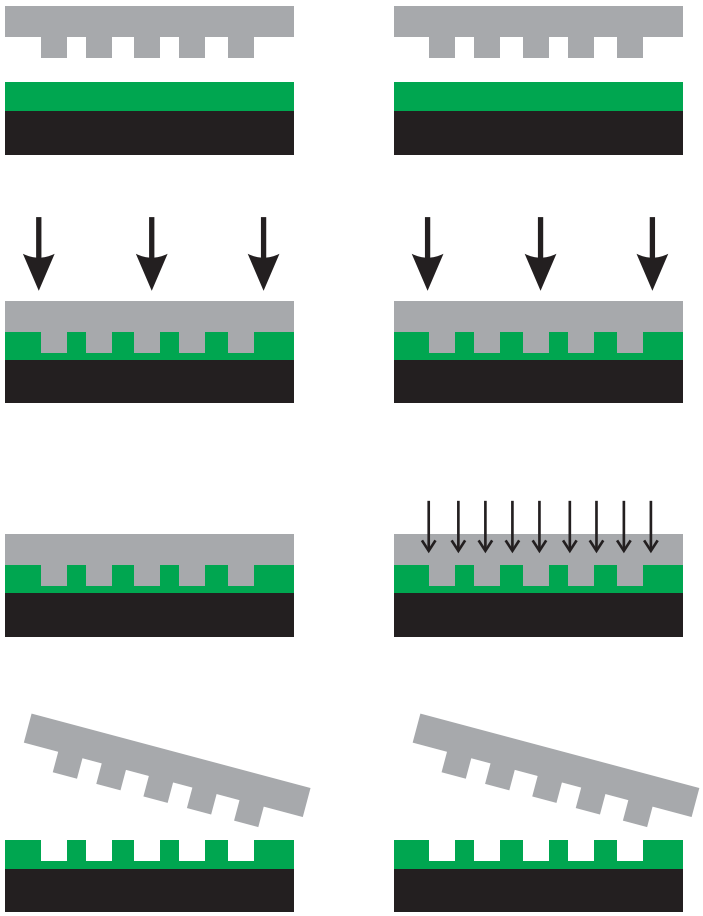

Figure 3.3: Working principle of thermal NIL (right) and UV NIL (left): Alignment of mold and substrate, imprint step, cool down/UV-curing and mold removal [23]

3.4.2 Stamp fabrication

We have to types of stamps. One stamp consist of a plane Si wafer that has a structured surface. This type of stamp is ideal for patterning large areas. Another type of stamp that we used is a molecular beam epitaxy stamp. This stamp does not have the same amount of structures than the Si stamp, but the structures can be made to be very small (few nanometers).

Flat Si wafer stamps are fabricated in either an OL or an EBL process. The OL process allow a fast fabrication of microscale structures on a Si wafer. After structuring the UV-sensitive polymer with a maskaligner and developing, a RIE process transfers the structures into the Si. For nanoscale structures, an EBL process forms precisely patterns on a e-beam sensitive resist which are also transferred into the Si. Common companies that are specialized on NIL stamps are IMS Chips (Stuttgart, Germany) or NIL Technology (Denmark). The common feature sizes are in the range of 30 nm to 45 nm.

Molecular beam epitaxy (MBE)-stamps feature a high precision and a large aspect ratio of the structures. The fabrication takes place in a MBE machine. An AlGaAs/GaAs superlattice is grown on a GaAs wafer. Since the materials are lattice matched grown, strain does not limit the possible layer thicknesses. The resolution of MBE growth is in the molecular regime. After the growth, the wafer is cut into peaces of 5 mm x 8 mm. The layers of AlGaAs an GaAs are selectively etched which is possible since the Al to Ga ratio is 80%. AlGaAs is etched by 5% HF and GaAs by citrid acid. The resulting patterns are used as stamp features resulting in ultra-thin lines. Also larger peaces can be cut out of the GaAs wafer, and the aspect ratio of the structures can be increased to 1 nm (feature width) by 2 inches (wafer size).

3.4.3 Advantages of NIL with respect to EBL

In contrast to EBL wherein the use of light or electron beams forms overcuts or undercuts when using positive or negative resists, respectively, NIL forms straight sidewalls of the structured polymer (see Fig. 3.4). This is due to the fact NIL is a mechanical process and the stamps feature straight structures wherein in the case of the beams, the triangular form of the beam results in that non-perpendicular resist exposure. In lift-off processes, metals are deposited on the substrate comprising the structured polymer. Since the sidewalls of the imprinted structures are straight and care is taken that the evaporation is perpendicular to the surface, the metals on the polymer and on the substrate are not connected to each other. Hence, when removing the polymer, the metals on the substrate remain there untouched. Thus, an imprint polymer can be used for booth types of processing.

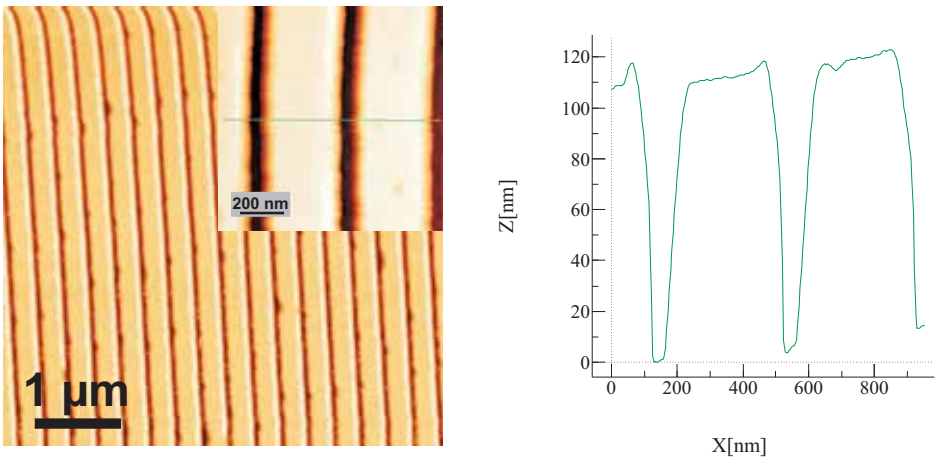

Figure 3.4: Atomic force microscope image of an imprinted NIL-resist. The resist had a thickness of 100 nm and the graph shows the topography of the imprinted structures (green line). The sidewalls are almost perfectly straight allowing either wet chemical treatments of the surface or also lift-off processes with deposited metals.

With respect to cost efficiency and speed, NIL is a fabrication method that patterns a large area of a polymer within minutes (thermal NIL) or seconds (UV NIL). The size of the area that can be structured is only limited by the available stamps and capability of the Nanoimprinter with respect to the process chamber. In the present work, a NIL Nanoimprinter 2.5 from the company Obducat was used wherein flat stamps up to 2.5 inches in diameter can be loaded. However, there are also machines which accommodate stamps up to 8 inches. With respect to the cost efficiency, stamps are cleaned after several processes by acetone and isopropanol and can be used for hundreds of processes. Thus, the cost of EBL-fabrication of NIL stamps is divided by a factor of several hundreds.

Further, when using MBE stamps, small structures with molecular resolution can be fabricated. In addition, because of the fabrication process, the aspect ration (length/width) can take values of 10^7.

3.5 Reactive-Ion Etching

Reactive ion etching (RIE) is used to etch materials without the need of liquid acids. A sample is placed in a chamber which is evacuated to a pressure around 10^{-5} bar. The chamber is than flowed with one or several process gases. An electrical high frequency (HF) field is generating ions that are accelerated perpendicular to the surface of the substrate. In addition to the HF field, a negative potential can be applied below the sample to further increase the velocity of the ions and to increase the etching rate. Depending on the process gas, different

materials, such as semiconductors, organic materials or insulators, are etched highly anisotropic and even a whole Si wafer can be etched through completely. This dry etching process is mainly used when substrates are patterned after a lithography process. Care has to be taken when introducing metals in a RIE machine. Metals that are etched remain in the inner wall of the chamber and are sputtered in the next processes from the wall. Thus, once metals were introduced in a RIE machine, the probability is high that the following sample will also have these metals on the surface. In the case of gold and optical devices, traps can be created in the optical devices and destroy the energy levels.

Our purpose of a RIE was not only the structuring of surfaces, but mainly the growth of insulators. This relatively new fabrication method was done at the Max-Planck-Institute of solid state in Stuttgart. After the deposition of Al in an evaporator, a native oxide is formed spontaneously on the surface when flooding the evaporation chamber. By treating the surface with a oxygen plasma in a RIE process, the thickness of the Al layer is increased from 2 nm to 3.6 nm. In addition, the formed AlO_x is pure and compact insulator. Together with a self-assembled monolayer (SAM), this material system represents are excellent gate dielectric in transistor technology [43].

We were able for the first time to form a thin layer of TiO_x on Ti. By treating the Ti surface with an oxygen plasma, a insulating layer having a thickness of 2.0 nm could be formed. The TiO_x features not only a excellent electrical characteristics for fabricating tunneling diodes, but also the physical resistance is outstanding.

3.6 Atomic Layer Deposition

The fabrication of aluminum oxide using a RIE machine has a lot of advantages, however, the dielectric thickness is limited to 3.6 nm [7]. In order to get thicker insulating layer wherein the thickness of the layer can be tailored precisely, the atomic layer deposition (ALD) process is the process of choice. Together with the physics department (E10), we fabricated several structures using an ALD machine.

ALD is a self terminating process. A sample is placed in chamber and after evacuation, a first process gas is introduced in the chamber. It uses two chemicals which react with a surface. After the process gas has formed a single layer of a product on the surface, not more material can be deposited since the surface is saturated. After evacuating the chamber again, a second process gas is introduced with reacts with the first deposited product until its surface is saturated. In this way, the first layer of a given material is deposited. The process is repeated until

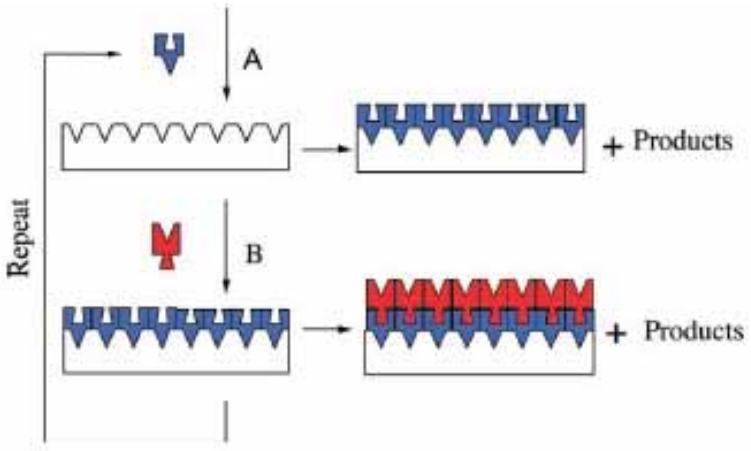

Figure 3.5: Growth of aluminum oxide by Atomic Layer Deposition. A: Trimethyl-Aluminum (TMA) is reacting with OH-groups on the substrate. B: Water is hydrolyzing the surface bound TMA. A new OH-group is created at the surface which can be used in a further cycle [67]

the desired layer thickness is reached. A schematic principle of the two reactions involved is depicted in Fig. 3.5

For the growth of aluminum oxide, the sample surface is first exposed to Trimethyl-Aluminum (TMA). The TMA is reacting with OH-groups on the substrate surface. For a uniform layer it is thus required to have many surface OH-groups. The first reaction is self-terminated with non-polar C-H groups. During the second process step, water is used to hydrolyze the surface bound TMA. By this, a new OH-group is created at the surface which can be used in a further cycle. In this way a layer-by-layer growth of aluminum oxide is achieved [8].

One drawback of this technique lies in the fabrication of thin films. In the case of aluminum oxide, the initial surface does not feature 100% hydroxil goups. That means that the first layers of the deposited aluminum oxide takes not place over the whole area, but seperated islands are formed. From our investigations, we observed that from thicknesses of 6 nm, a closed film can be garanteed. In order reach precise film thicknesses below 6 nm, the oxide growth with a RIE machine or the combination of that machine and an ALD process leads to reproducible results.

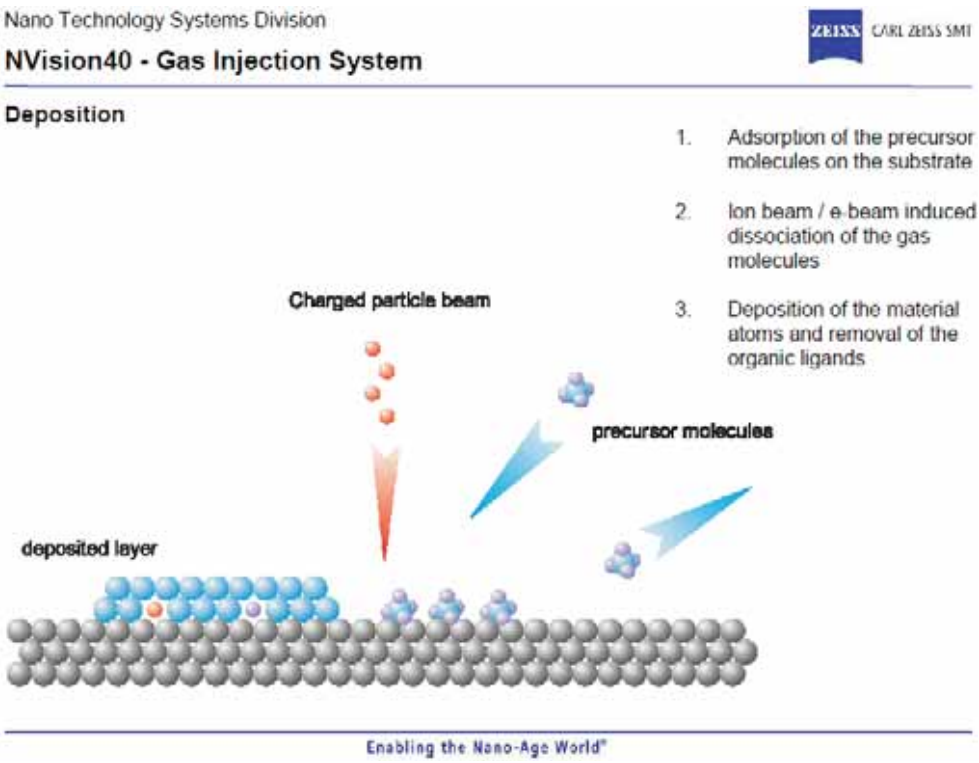

Figure 3.6: Schematic of the material deposition system (gas injection system) of the NVision© 40 Dual Beam from Zeiss. Reprinted with permission from Zeiss. Copyrigth 2012 Zeiss.

3.7 CVD in NVision© 40 Dual Beam

The NVision© 40 Dual Beam from Zeiss that is located at the Technische Universität München features a gas injection system for an charged particle-enhanced chemical vapor deposition. For the present work, a similar system at the University fo Notre Dame has been used. The basic principle of this system is explained briefly. A gas nozzle is brought close to the surface and a precursor gas is flowing onto a particular area of the surface. Some molecules of the precursor gas were absorbed on the surface. When a charged particle beam is exposed to the surface material from the gas is deposited (see Figure 3.6). The present system has the possibility to deposit several metals. Table 3.1 gives an overview of some materials that can be deposited.

In order to deposit materials precisely on a predetermined area, it is very important to focus the electron beam carefully before exposing the processes area. Another aspect has to be taken into account, when a particular area of a substrate is exposed to the precursor gas, of course, the gas is not localized to that area but is diffusing into chamber. After the material deposition, a break

possible materials	available in NVision© 40 Dual Beam
tungsten	yes
platinum	yes
carbon	yes
silicon oxide	yes
gold	no

Table 3.1: Deposition materials for gas injection system.

of at least 10 min has be taken before the success of the material deposition is evaluated. Otherwise, further material is deposited from the remaining precursor gas on the whole area that is exposed to the electron beam for inspection leading to undesired further materials. Drawbacks of this precise fabrication method is the speed and throughput, and the resistivity deposited metals like Pt or Au is high. That low conductivity can be further improved by annealing in an oxygen oven in order to remove carbon that is present in these metals after deposition.

Using this technique complex 3-dimensional structures can be deposited on pre-structured surface comprising even electronic devices. An example that will be presented later in this work, is the fabrication of a Pt bridge from a MIM diode through the air into a contact pad.

3.8 Focused ion beam

A focused ion beam system (FIB) is also implemented in the NVision© 40 Dual Beam. Ga atoms from a liquid metal source are accelerated and focused on a substrate. With this tool, the surface can also be inspected and imaged on a monitor. However, the energy of the ions is higher than the energy of the electrons and therefore, the etching rate of the substrate is also higher. In other words, even 3-dimensional structures can be etched into the substrate´s surface. The electron beam source and the ion beam source are arranged 54° tilted with respect to each other. When structuring a surface, the substrate is tilted by 54° and the two beams are aligned. The ion beam is than perpendicular arranged with respect to the surface and vertical etching can be done. With the electron beam, the surface can be inspected after every etching step. The ion beam is not used for the inspection since an ion exposure when investigating the sample leads directly to an etching of the surface. In this way, complex 3-dimensional structures can be fabricated including bridges and freestanding structures. A schematic of the FIB system is shown in Figure 3.7.

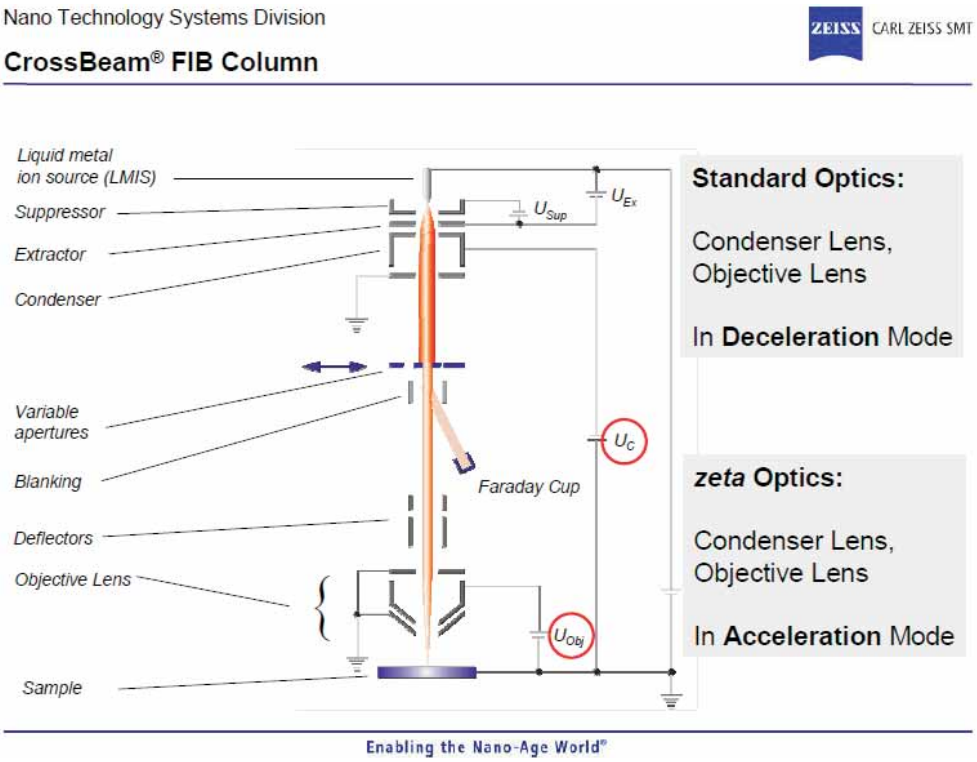

Figure 3.7: Schematic of the FIB system of the NVision© 40 Dual Beam from Zeiss. Reprinted with permission from Zeiss. Copyrigth 2012 Zeiss.

3.9 Plasma Asher

A plasma asher is usually used to remove organic materials. An oxygen plasma or an argon plasma can be produced in a chamber wherein a sample is placed. In contrast to a RIE machine, microwave radiation (2.6 GHz) forms oxygen or argon ions which does not lead to a homogeneous vertical anisotropic etching of a polymer. The ions are moving randomly in every direction leading to remove of a polymer from every side. With respect to cleaning, plasma asher is preferable to a RIE machine. With respect to etching, a RIE is faster and precise that is why for this purpose, the latter machine should be used.

Another interesting aspect with respect to an plasma asher is ability to form hydroxyl groups on several surfaces which is necessary in the nano transfer printing process. Since the nano transfer process is essential in the present work, Chapter 5 discusses this topic intensively.

3.10 Desiccator

A desiccator was used for covering surfaces with hydrophobic organic-self assembled monolayers (SAM), namely perflouroctyltrichlorsilane. A sample and 0.5 ml of a SAM are placed into petri-glasses in a desiccator. After evacuation to around 10 mbar, the sample and the SAM are left in the desiccator for about half an hour. As a consequence, the SAM saturates the hydroxyl groups on the surface, and after annealing, one monolayer is formed on the surface of the sample. This hydrophobic monolayer decreases the surface energy drastically such that the adhesion between said surface and material that comes into contact which this surface can be easily removed.

Chapter 4

Characterization methods

The characterization of the structures and devices fabricated in the frame of this work focused mainly on the morphological, electrical and electro-optical properties. Several setups were in our laboratory and laboratories at other universities used for this purpose. In this chapter, the most important characterization setups are described in detail.

4.1 Optical Microscope

The microscope that we mostly used to get a first impression of the success of a process was a Leica DM 2500 M. The microscope allowed the inspection of samples via reflected or transmitted light from a 100 W Halogen (Hg/Xe) light source. Several magnifications were possible with this microscope (5x, 10x, 20x, 50x, and 100x) and with an attached camera, the images could be recorded and saved on a computer for further image processing.

The microscope was clearly very useful for fast optical inspections, however, since dimensions of the fabricated structures were in the nanometer range, other investigation methods like a scanning electron microscope or an atomic force microscope are unavoidable for a precise analysis. The smallest feature size that could be detected in this microscope was 200 nm.

4.2 Atomic force microscope

In order get information about the topology of nanoscale devices, an atomic force microscope (AFM) is the investigation setup of choice. The lateral resolution of an AFM is worse than of a scanning electron microscope (SEM), however, the vertical resolution is on the atomic scale. We used in the present work a *JSPM-5200* from the Company *Jeol*. The configuration of an AFM is schematically shown Figure 4.1.

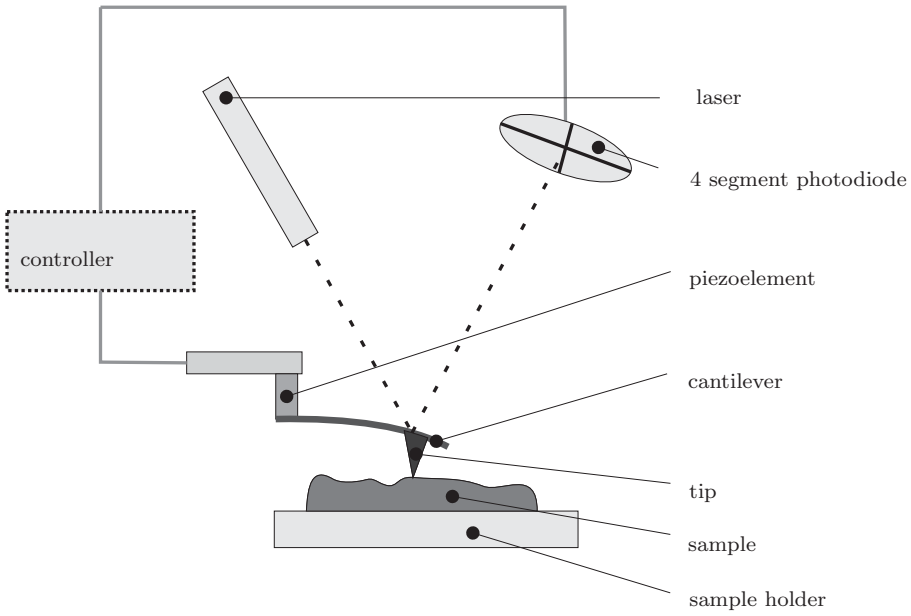

Figure 4.1: Schematic view of an AFM [68].

The tip is brought into contact with the sample surface and such that the cantilever which represents a spring, is bent. The spring constant of a cantilever is usually in the range of a N/m and forces down to 10^{-12} N which corresponds to a theoretical spatial resolution 10^{-12} m can be detected. However, because of the thermal noise, the resolution is in general higher than 20 pm [69]. In the distance between 1 nm to 10 nm, the attractive Van-der-Waals interaction is dominant. When the tip comes closer to the surface, the repulsive interaction is dominant. The interaction between the tip and the substrate can be described in general by the $Lenard - Jones - Potential$:

$$V(r) = \frac{a}{r^{12}} - \frac{b}{r^6} \tag{4.1}$$

The cantilever is excited by the piezoelement to oscillations in the few 100 Hz range. The resulting moving of the laser beam that is reflected on the backside of the cantilever is determined in the 4 segment photodiode. Via the piezoelement, a feedback loop is keeping the distance between the tip and substrate constant during measurement. When the topology of the surface is changing, the interaction between the tip an the substrate is changing as well. This results in a change of he amplitude of the oscillating cantilever. In this way, the actual heights on the surface can be measured.

4.3 Probe station

4.3.1 Microscale tips

A *Rucker & Kolls 680A* probe station comprising a *Keithley SCS 2400* parameter analyzer was used in order to characterize electrically devices or structures. We determine the I-V-characteristics of devices by applying an external voltage. In the case of structures, e.g. metal lines, this setup was used to investigate the conductivity, which is dependent on the geometry of the structures. This probe station is a three terminal port station. The chuck, on which the sample is placed is conductive and connected to the first port. Usually this port is used in the transistor research for applying a gate voltage, e.g. to the substrate. The other two ports are connected to micro manipulators, namely PH 100 from Suess Microtech. Using these manipulators, two conductive needles can be placed carefully on any target substrate. Since the tip radius of the needles were only 7 µm, small structures in the micrometer rang can be easily contacted.

Usually, on one needle the voltage was sweeped in the range of several volts and the second needle was set to ground potential. While sweeping the voltage on the first needle, the current flowing through both needles was measured. A alternating voltage with frequencies up to 100 MHz could also be applied to the to a needle and this way, capacitive measurements were accomplished.

In this work, mostly metal-insulator-metal (MIM) diodes were investigated. Therefore, only two ports of the probe station were used. Since, very low currants down to 10^{-15} A were measured, a insulating glass plate was placed between the sample and the conductive chuck, in order to avoid parasitic currents.

4.3.2 Nanoscale tips

Since the electrical characterization of nanoscale devices is not possible with *Rucker & Kolls 680A* probe station setup, a conductive atomic force microscopy (C-AFM) at the University of Notre Dame was used for this purpose. We used an *MFP-3D AFM* (Asylum Research, California) with an ORCA holder that features two transimpedance amplifiers with a gain of either $1x10^6$ V/A or $1x10^9$ V/A. The sample was clamped via the conductive substrate to a gold electrode, which was also connected to the cantilever holder, thus creating a complete circuit between the sample and the cantilever tip. We used Ti/Pt (5/20) coated silicon tips (OMCL-AC240TM, Olympus, Japan) for the measurement [7]. A photograph and a schematic image of the setup is shown in Figure 4.2.

Nanoscale vertical MIM diodes were investigated using this measurement setup (see chapter 6). First, the topography of the sample was measured in AC

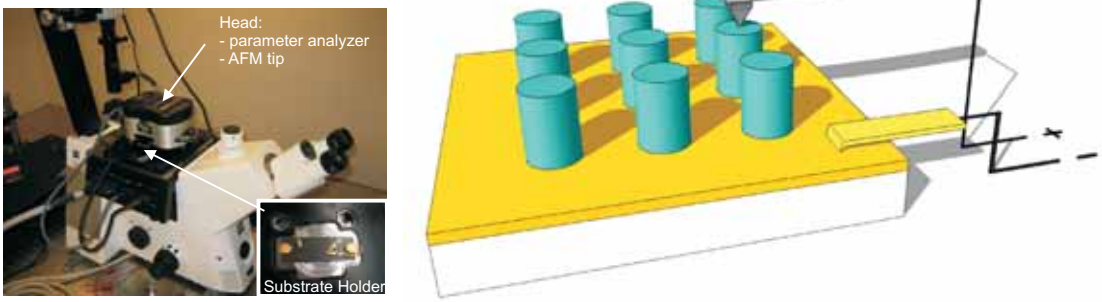

Figure 4.2: a) A photograph of the conductive atomic force microscope (AFM) setup: The parameter analyzer and the AFM tip are implemented in the head, and the substrate holder comprises ceramic plate and gold clamps for connecting the sample substrate. b) A schematic view of the AFM setup: The MIM pillars (turquoise) that are transfer-printed on a Si wafer (white) comprising a conductive AuPd layer (orange) are contacted from the top via a conductive AFM tip (here: positive voltage). The AuPd-layer on the substrate is connected via a gold clamp (here: negative voltage). Reprinted with permission from [7]. Copyright 2012 American Chemical Society.

tapping mode. Then, after a target structure was identified, the AFM cantilever tip was brought into direct contact with the surface. To ensure a good electrical connection, the tip was dithered in an outwardly expanding 5 nm spiral pattern in a span of 5 seconds. Then, the tip was held motionless as an electrical bias was applied through a cyclic, triangle wave pattern, to the sample through the gold electrodes on the sample mount while the current was simultaneously measured at the tip. This was repeated numerous times at different MIM device [7]. After that, the data that we obtained from these measurements were averaged.

4.4 Scanning Electron Microscope

The scanning electron microscope (SEM) that we used in order investigate structures in the nanometer regime was part of the NVision© 40 Dual Beam from Zeiss. With this setup, the lateral dimensions of features on the surface of sample can be determined precisely. Though the height differences of structures on the surface can detected, for a precise determination the AFM is preferable.

The electron beam is generated by heating up a tungsten filament and directed onto the substrate through condenser and magnetic lenses. By changing the acceleration voltage, the electrons reach the surface having a higher energy. Typical values are here between 1 kV and 20 kV acceleration voltage. Obviously, when sensitive substrates are used, e.g. that are covered with polymer, the acceleration voltage should be set to a low value since high-energy electrons can burn the substrate´s surface. On the other hand, by increasing the acceleration voltage, smaller structures can be detected and investigated. With scanning coils, the narrow beam is traced over the surface in order to investigate a whole are. A challenge when investigating surfaces is when the material of the substrate consists of an insulating surface. The electrons of the beam are penetrating into the substrate and when the substrate is insulating, a charging of the substrate takes place, since the electrons cannot reach a ground potential. When the substrate is charged, the electrons coming from the beam have an inhomogeneous Coulomb-force resulting from the substrate which leads to a beam shift. Therefore, when precise images of an insulating surface are necessary, the surface should be covered by a thin conductive film like gold. The detection system detects secondary electrons created by inelastic scattering, direct backscattered electrons from the beam and X-rays that is emitted beneath the specimen´s surface using two detectors, namely an inlens detector and a chamber detector. Detecting the number of electrons generated, the detector sends this information to a processing unit which creates an image that shows the height differences in gray scale on a monitor. SEMs have tremendous depth of field compared to traditional microscopes, providing an almost 3-D image for researchers to analyze, as compared to the flatter image an optical microscope produces. Magnification powers up to 300.000

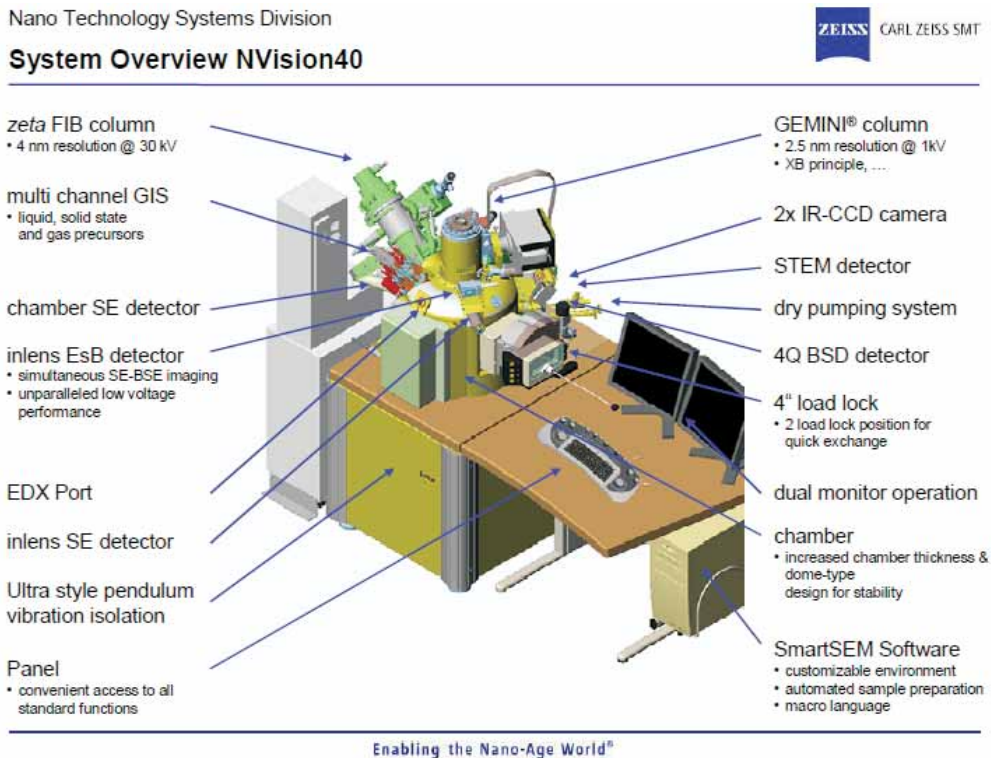

Figure 4.3: Schematic of a NVision© 40 Dual Beam from Zeiss. Reprinted with permission from Zeiss. Copyright 2012 Zeiss.

are possible [8].

4.5 Ellipsometry

Ellipsometry is method wherein the change in polarization of light is measured when the light is reflected (or transmitted) at a sample. In general, the electromagnetic field of light is orthogonal to its propagation direction. Common light sources, such as filament lamps or the sun, provide unpolarized light, that is, light featuring a completely random orientation and phase. Polarizer, such as a wire-grid polarizer, allow to polarize the light which originates from light sources. Three different polarizations can be obtained in this way (Fig 4.4):

- linear polarized light
- circular polarized light
- elliptical polarized light

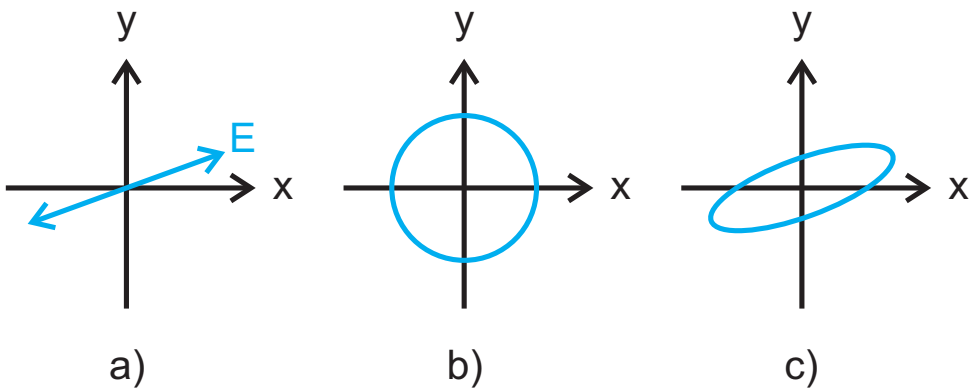

Figure 4.4: Three different types of polarization of light are shown: a) linear polarized light, b) circular polarized light and c) elliptical polarized light.

When two orthogonal light polarizations are in-phase, linear polarized light is obtained. Depending on the relative difference in the amplitude between the two orthogonal light phases, the angle between the light phase having the larger amplitude and the polarization direction of the resulting amplitude of the electric field is smaller than 45° (in Fig. 4.4a, the angle between the electrical field E and the x-axis). In the case that the two orthogonal waves are exactly 90°out-of-phase and feature the same amplitude, the superposition of both waves results in circular polarized light. If orthogonal waves having arbitrary amplitudes and phases, elliptical polarized light is obtained (Fig. 4.4b).

Usually, an incoherent broad light source, such as white light, is used in ellipsometry setups. After passing a polarizer, the light is linear polarized. The angle between the polarization of the light and the surface of the sample is between 0° and 90°, and therefore, the electric field vector can be described as a superposition of a s-plane wave (parallel to the surface) and a p-plane wave (orthogonal to the s-plane wave) (see Fig. 4.5). After the reflection of the linear polarized light on the surface and the sublayer beyond the surface, the relative phase and amplitude of the s-plane wave and p-plane wave change independently and elliptical polarized light of the reflected light is analyzed e.g. in a rotating analyzer. After obtaining the data, a model which includes the optical parameters and the thickness of the surface layer and sublayers is used for fitting the experimental data to the model until a good agreement is achieved. In this way, the optical parameters and the thicknesses can be achieved.

4.6 Setup for optoelectronic characterization

For determine an antenna response of our rectenna arrays, a coherent and linear polarized light source is needed. The optoelectronic characterization of the chip

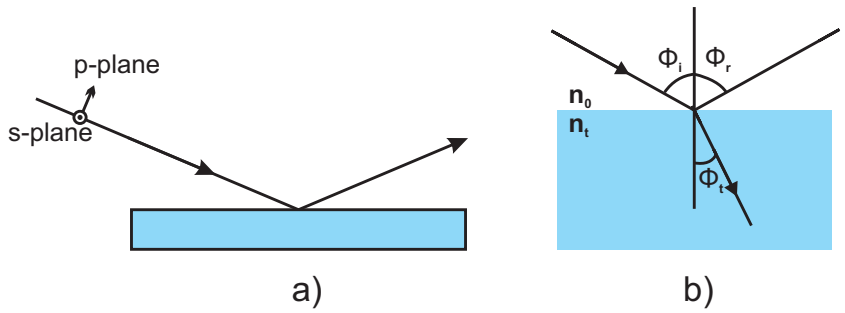

Figure 4.5: a) An incident light beam is linear polarized and the electric field vector can be described as a superposition of a p-plane wave and s-plane wave. After being reflected on the surface of the sample, the relative phase and amplitude of the s-plane wave and the p-plane wave is changed resulting in elliptical polarized light. b) Light reflects and refracts according to Snell´s law.

was carried out using the experimental setup shown in Figure 4.6. The device under test is mounted on a translation stage and it is illuminated by a CO_2 laser operating on its main emission line at 10.6 µm. A polarizer is used to ensure the linear polarization state of the incident radiation, which is rotated by a half-wave plate. A mechanical chopper is used to square-wave modulate the laser beam. The response of the device is measured with a lock-in amplifier that is synchronized to the modulation frequency of the mechanical chopper.

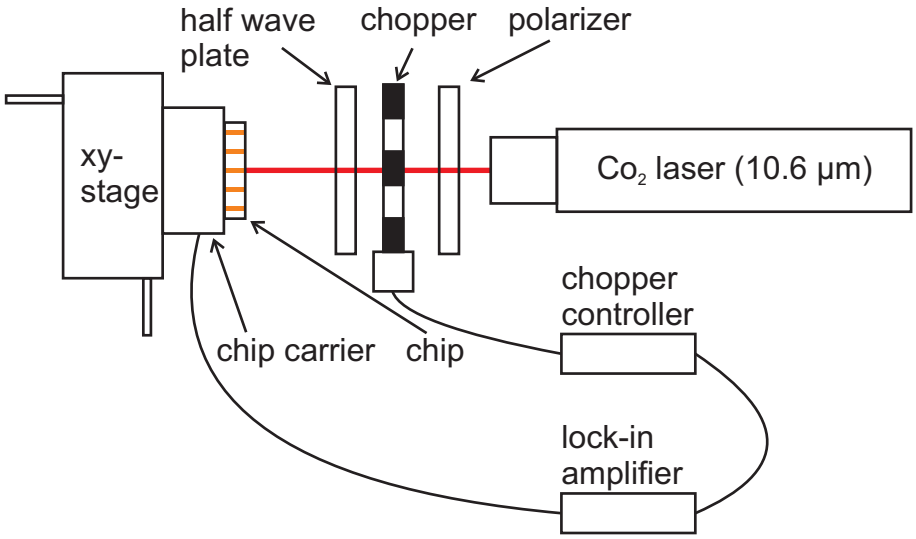

Figure 4.6: Experimental infrared testing arrangement. The CO_2 laser provides the 10.6 µm radiation used to test the fabricated rectenna array. The linear polarized light is rotated by a half-wave plate and square-wave modulated by a mechanical chopper. With permission from [62]. Copyright 2012 [62].

Chapter 5

Nanotransfer printing technology

The main fabrication technology that was used in this work is the nanotransfer printing (nTP). In this chapter, this novel fabrication technique is explained in detail. First, the basic concept of nTP is presented, focusing on the two main parameters of the transfer process, namely the hydrophilicity and the transfer temperature. Parts of these sections have been previously published in [7, 44]. Further, two approaches are described that were used for the manufacture of nanostructures, these are, molecular-beam-epitaxy (MBE) stamp approach and Si wafer stamps for structure and device fabrication. Parts of these sections have been published previsouly in [8].

5.1 Basic concept

Electron beam lithography (EBL) is the state-of-the-art fabrication method in a research enviroment for the production of structures and devices in the few nanometers range [70, 71]. Unfortunately, EBL is a slow and costly fabrication method, thus, not applicable to the realization of large scale systems, e.g., integrated circuits. Nanoimprint lithography (NIL) is a very promising technique for fast and high throughput production of nano structured devices [33, 72–75]. One drawback of NIL, similar to the EBL process, is that it is also a non-dry and complex process. Nanotransfer printing is a novel method for forming, e.g., metal patterns, by pressing a stamp, covered with metals, on a substrate [76, 77]. In order to provide weak adhesion between the stamp and the deposited metals, a self-assembled monolayer (SAM) is applied on the stamp, which saturates the surface dangling bonds [78, 79]. Several devices have been fabricated using this technique, for example, polymer light-emitting diodes [80, 81], electrical contacts, and capacitors [46, 47, 82]. NTP is a fast and low cost process which does not require lithographic processes. The dimensions of the transferred structures are entirely determined by the stamp. Thus, such a technique can be very useful for the realization of nanostructures over large areas, such as in the

realization of sub-wavelength gratings [83] for optical devices [44].

The basic principle of nanotransfer printing (nTP) is shown on Figure 5.1. Since we want to point out here that not only metal structures but whole devices can be fabricated using this approach, this example presents the fabrication of metal-insulator-metal (MIM) diodes using nTP. The stamp may consist of a flexible material such as PDMS or a rigid one, e.g. Si or GaAs. Both types of stamps have advantages. PDMS is a relatively low-cost material that can be easily formed by placing that material in a form when it is liquid and when taking it out when becoming solid, the surface features the desired structures. The main limitation when using flexible stamps is the lowest achievable feature size that is usually in the range of a few 100 nanometers. Conventional hard stamps however are fabricated e.g. by precise e-beam lithography processes and feature structure size down below 50 nm. Once the stamps are fabricated, the main challenge that has to be overcome is the adjustment of the surface energy of the stamp. Since material that is deposited on a stamp has get off easily in a transfer-printing process, the adhesion between the stamp and the substrate has to be kept low. While flexible PDMS stamps have already a very low surface energy, for Si wafers the polar bindings on the surface that provide a good adhesion can be saturated by a self-assembled monolayer (SAM). After that, it is better to deposit a noble material directly as the first layer on the stamp that is covered with the SAM. Such materials are Au, Pd, Pt or alloys of these materials. Since the reactivity of noble metals is low, the adhesion to surfaces is in general weak. Thus, the combination of a saturated (hydrophobic) stamp surface and a noble material as a first layer increases the probability of a successful delamination of the metal from the stamp. After this initial layer, further materials can be deposited as subsequent layers. The final metal layer should be an adhesion promoter which can be e.g. Ti or Cr. The surface of this layer can be activated (hydrophilic) and the amount of polar groups is increased. The target substrate, namely Si or SiO_2 wafers or glass, is also activated. When the stamp gets into contact with the substrate, the hydrophilic Ti layer binds to the hydrophilic substrate and the metal stacks are transferred onto the substrate. The stamp is cleaned afterwards and re-used several times. Therefore, a fast and low cost nanoscale fabrication method is possible. Since the hydrophilicity is a fundamental parameter, the next section discusses briefly how to tailor the surface energy.

5.2 Hydrophilicty

The formation of hydrophilic surfaces is due to the presents of polar groups. In the present work, mainly hydroxyl (-OH) groups are considered. If a hydrophobic surface, for instance on a stamp, is required, a removal or saturation

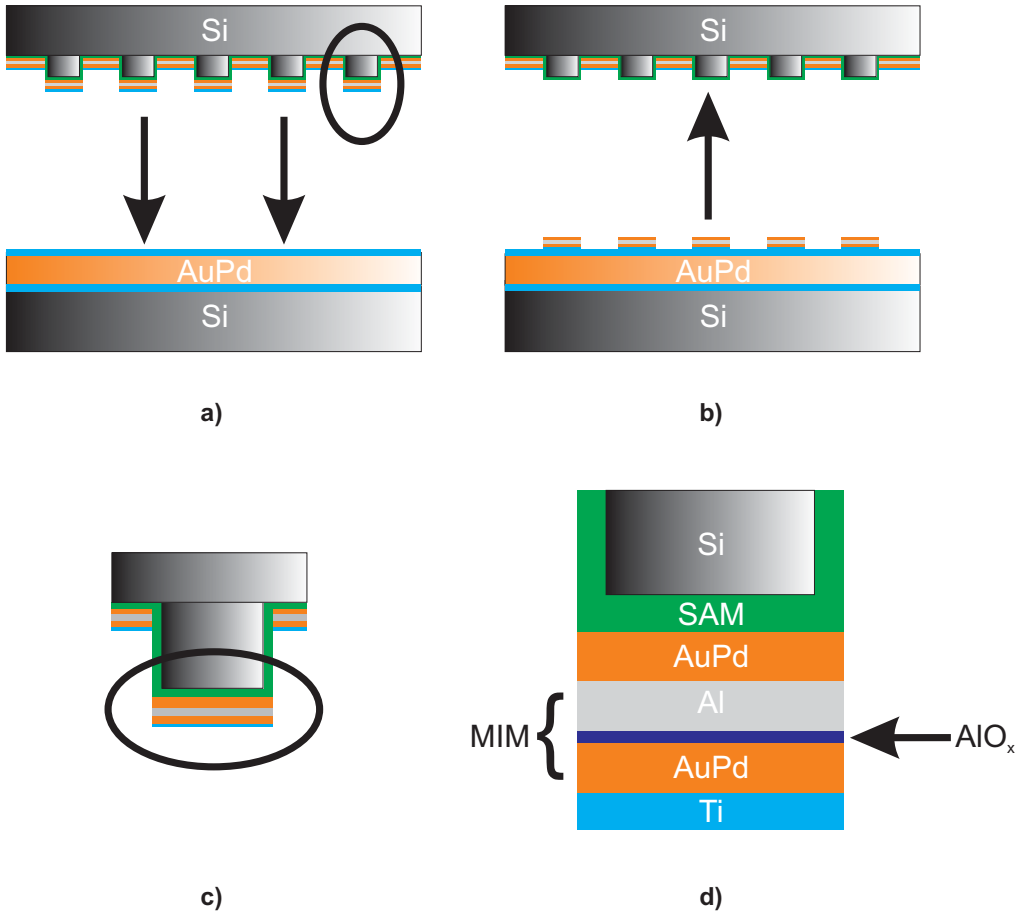

Figure 5.1: The nanotransfer printing process is shown in detail. a) Before the transfer process, the Si wafer stamp is covered with an organic self-assembled monolayer (green). The AuPd layer (orange) attached to the SAM layer provides weak adhesion between the MIM diode and the stamp. The Al layer (gray) serves as the first metal electrode. Then, the stamp is treated with a brief oxygen plasma exposure to form an AlO_x dielectric (violet). The second electrode is AuPd. The last layer is Ti (blue) that is an adhesion promoter between the MIM diode and the target substrate. When the stamp comprising the metals and the dielectric is brought into physical contact with the substrate which is covered with a AuPd layer (orange) and two Ti layers (blue) for providing a good adhesion, b) the material stack on the elevated structures is transferred to the substrate. The SAM remains on the stamp and can be used again. In c), a zoom of the structures on the stamp (black circle in Figure S3a)) is shown. In d), the material stacks on the stamp are shown in detail (black circle in Figure c)) Reprinted with permission from [7]. Copyright 2012 American Chemical Society

Figure 5.2: Surface energy is adjustable by a) a plasma treatment in order to from hydrophilic silanol groups on the Si wafer, or b) by saturating open bonds on the surface with a hydrophobic organic self-assembled monolayer. Reprinted with permission from [7]. Copyright 2012 American Chemical Society.

of these groups is essential. SAMs are molecules comprising chains of CH_2 atoms featuring a functional head group. Depending on the presents of certain functional groups, the SAM adhere well to surfaces. For example on Si, silane based molecules binds excellently to hydroxyl groups that are present on the surface. The other end of that molecule has mostly a CH_3 molecule that is not polar and thus provides weak adhesion to material which gets into contact. In this way, the surfaces becomes hydrophobic (see Fig. 5.2b). In the case of GaAs, thiol based SAM may be used, however it has been shown that, the formation of a native oxide on GaAs stamps is sufficient for providing a hydrophobic surface. Therefore in the case of GaAs stamps, a SAM coverage of the stamp is not necessary.

In order to achieve a hydrophilic surface, several processing methods are available. For Si surfaces, an RCA 2, an piranha clean, an UV treatment or a microwave induced plasma treatment are reported [7] (see Fig. 5.2a). The latter one has the advantage that a wet chemical process steps can be completely avoided in the nTP. For thermally grown SiO_2 layers on Si, these activation processes do not create such a high surface energy than in the case of of pure Si. The high temperature fabrication of SiO_2 removes most hydroxyl groups which cannot recover easily. Here, a RCA 1 clean for 1 min is the activation method of choice. Table A.1 in the appendix gives an overview over the activation methods for several materials.

5.3 Temperature

During the investigation and optimization of the nTP process, we observed a strong temperature dependence of the transfer yield. The transfer yield is defined as follows:

$$\text{transfer yield} = \frac{\text{number of transferred metal structures}}{\text{number of structures on the stamp before transfer process}} \cdot 100\% \tag{5.1}$$

In order to understand this unexpected behaviour, we designed an experiment in which several stamps were used in order to find a theoretical model for this effect. At the end, we observed that the removal of water that is formed during the printing process is necessary in order to obtain a good adhesion between the structures to be transferred and the substrate.

Experiment In this experiment we show three possibilities for fabricating and duplicating stamps, and different methods to cover the stamps with materials. All methods lead to successful transfer printed structures. The first stamp which is a 2-inch Si stamp (stamp A), consisting of structures in the range of several hundred nanometers, was fabricated by duplicating a nickel stamp (master stamp) made by electron beam lithography. The precise fabrication process of master stamps with electron beam lithography is explained in section 5.5. The reproduction was done using a two-step nanoimprint lithography process (NIL). The master stamp was pressed in an Intermediate Polymer Stamp (IPS) fabricated by Obducat (Obducat AB, Malmö, Sweden) [84]. Then, the IPS with the negative copy of the master stamp was used as a stamp and a usual NIL process was done on a 2-inch Si wafer [85]. The imprinted structures were etched in the Si wafer by reactive ion etching (RIE). A second 2-inch Si stamp (stamp B) was fabricated by optical lithography and further dry etching. It consisted of a grid structure with 500-mm line thickness and the lines were spaced from each other by 100 to 500 mm. A plane 2-inch Si wafer (stamp C) was used as a third stamp on which metal dots with diameters between 70 and 400 mm were deposited through a shadow mask.

The SAM, 1H, 1H, 2H, 2H-Perfluorooctyltrichlorosilane, 97%, fabricated by Alfa Aesar (Alfar Aesar, Ward Hill, MA, USA) was applied for saturating the dangling bonds on the surface of the stamps. By placing the stamps and 1mL of the SAM in vacuum for 15 min, a layer of the SAM is formed on the surface. After that, the stamps were placed on a hotplate at 150°C for 30 min to consolidate the SAM monolayers. In this way, the wafer becomes very hydrophobic and adhesive forces between the stamp and the metals were

strongly reduced [86]. The SAM-molecules adhere to SiO_2 or Si surfaces as Si turns normally into SiO_2 due to oxidation in air [87].

A 30-nm thick metal layer was deposited on the stamp by thermal evaporation. A 4-nm thick titanium layer was thermally evaporated on top of the previously deposited gold layer in order to increase the adhesion between the metal and the substrate [34]. An activation of titanium was performed by UV light with a power density of 70 mW/cm^2 for 1 hour and a brief oxygen-plasma treatment. This breaks the bonds of the native formed TiO_2 and titanols are formed in humidity [88]. In the case of nanotransfer printing of aluminum and Permalloy, a titanium layer was not necessary as the surface of these materials already consist of –OH groups due to oxidation in humidity at room temperature [89–91]. The 2-inch Si and 2-inch SiO_2 substrate surfaces were activated by soaking the wafers in a 6:1:1 volumetric mixture of distilled water, H_2O_2, and HCl for 10 min at 75°C. This procedure generates surface hydroxyl (-OH) groups on the (native) SiO_2 layer [46].

The nTP was performed in the NanoimprinterTM NIL 2.5 from Obducat. The substrate was placed on a plane surface and the stamp, covered with the metal,was placed upside down on the substrate. A pressure of 50 bar was applied for 5 min. The transfer process was performed at different temperatures wherein heat was applied before and after applying pressure. In addition to that, transfer processes around room-temperature were done under vacuum conditions. In order to determine the effectiveness of the transfer process, we define the transfer yield (or transfer gain) as the percentage of the metal actually transferred on the substrate according to equation 5.1.

The transfer gain has been measured as a function of temperature for the flat stamp C by taking images of the stamp and the substrate after transfer printing and performing an image processing using a Matlab code.

Explanation for temperature dependence We observed a strong temperature dependence of the transfer gain. For the determination of the optimal transfer temperature, we used stamp C with a 30-nm thick gold layer, assisted by a 4-nm thick titanium layer. Under non-vacuum conditions, the gain is zero percent up to a temperature of 50°C, that is, transfer printing of the metal on a Si/SiO2 substrate could not be performed without heating the substrate. By increasing the process temperature, the gain increased correspondingly and full transfer was reached at 200°C. Above this temperature, the transfer gain remains around 100%. An example of the transfer printing of stamp C at 200°C is shown in Fig. 5.3, along with the dependence of transfer gain versus process temperature. At temperatures below 200°C, the transfer gain

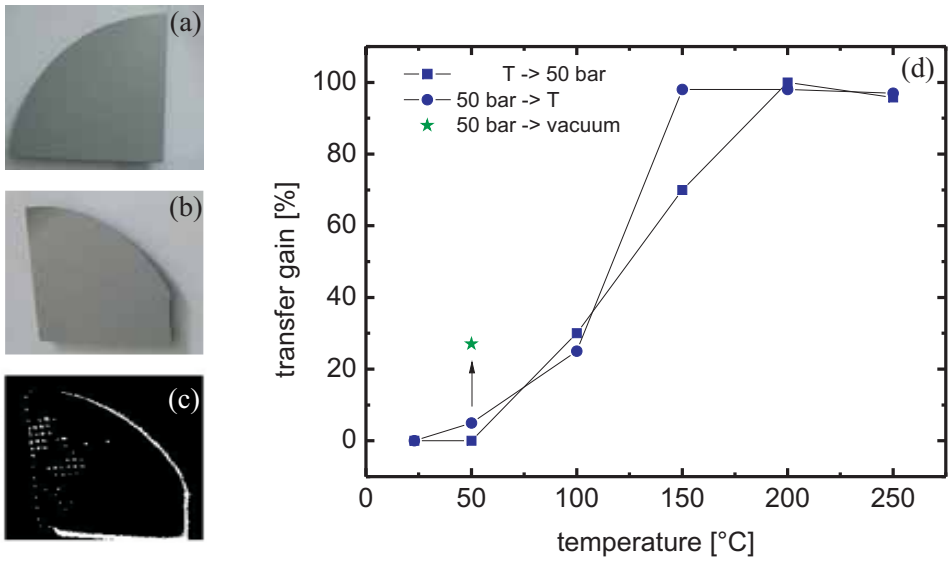

Figure 5.3: (a) Stamp C, (b) substrate, and (c) image processed substrate after transfer printing. Process parameters were 50 bar for 3 min at 200°C (390 F). The gain versus the process temperature is shown in (d). Reprinted with permission from [44]. Copyright 2011 Taylor and Francis.

is increased when pressure is first applied and then temperature is increased from room temperature to target value. We also observed that at 50°C, transfer of metals is achieved under vacuum conditions. After the optimization of the process temperature, we succeeded in transfer printing the grid of stamp B with 45-nm thick gold structures (assisted by 4nm titanium) over the whole 2-inch wafer. Figure 5.4(a) shows the transferred gold grid. The defects that can be observed are due to a few dust particles on the substrate where the stamp could not get in touch with the substrate. Furthermore, we were able to completely transfer dot-like structures of gold, assisted by 4nm of titanium at 200°C using stamp A. At these temperatures, we were also able to transfer other metals, such as aluminum and Permalloy. Figure 5.4(b) presents a section of a large area transfer of dot-like structures of aluminum transferred with stamp A.

As the performed experiments showed, the transfer gain is strongly dependent on temperature, around 200°C being the optimal temperature. We want to discuss here the reason for this behavior and to explain why the chemical bonds are made durable by applying heat. It is known that the application of heat can improve the nTP when using a flexible PDMS stamp [92]. There, it was speculated that the heating step in the transfer print process facilitates diffusion of low-weight components of the PDMS to the stamp surface and/or

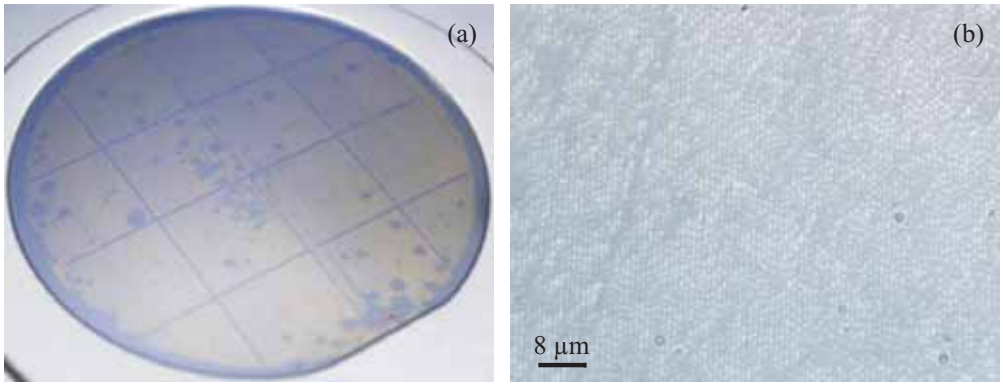

Figure 5.4: (a) Transfer printed 2-inch (2.54 cm) gold grid and (b) transfer printed dot-like structures of aluminum. Reprinted with permission from [44]. Copyright 2011 Taylor and Francis.

reorientation and segmental motion of polymer chains in this region. Both effects would accelerate surface hydrophobic recovery in the PDMS, which would lead to an easier transfer of the metal deposited on the PDMS stamp. Such an argument is applicable to PDMS stamps but not for the presented transfer process we have performed with stamp A-C.

Figure 5.5 gives a schematic overview of the interfaces during the nTP of gold films on a silicon substrate. There, titanium is deposited above the gold layer and silicon is the substrate to be transferred on. As previously discussed, by activating the surfaces with UV light, oxygen plasma, and a HCl cleaning, silanol and titanols are formed, respectively, on the silicon and titanium surfaces. By combining the metal and the substrate surface, the Ti-OH molecules and the Si-OH molecules form a Ti-O-Si bonding and H_2O is released [93]. Furthermore, by adding H_2O to a Ti-O-Si bonding, the connection is not stable and silanols and titanols are formed again [94]. Therefore, nTP is strongly improved by removing the water originating in the process. By applying a temperature of 200°C, the physisorbed water is completely removed from the interface [95]. This postulate is confirmed as under vacuum conditions, transfer of metals is possible even at low temperatures. The transfer gain in the vacuum promoted process is not one 100% as our nanoimprinting machine does not provide high vacuum conditions (around 0.8 bars). Furthermore, we observed that the transfer process is improved when the pressure is first applied and then the temperature is increased. For better understanding this behavior, we investigated the hydrophilicity of Ti and Si after UV and plasma treatment under vacuum and high-temperature conditions before the transfer process. We observed a strong decrease of the hydrophilic character for both materials when exposing them to vacuum conditions (10 mbar) as well as when applying temperatures

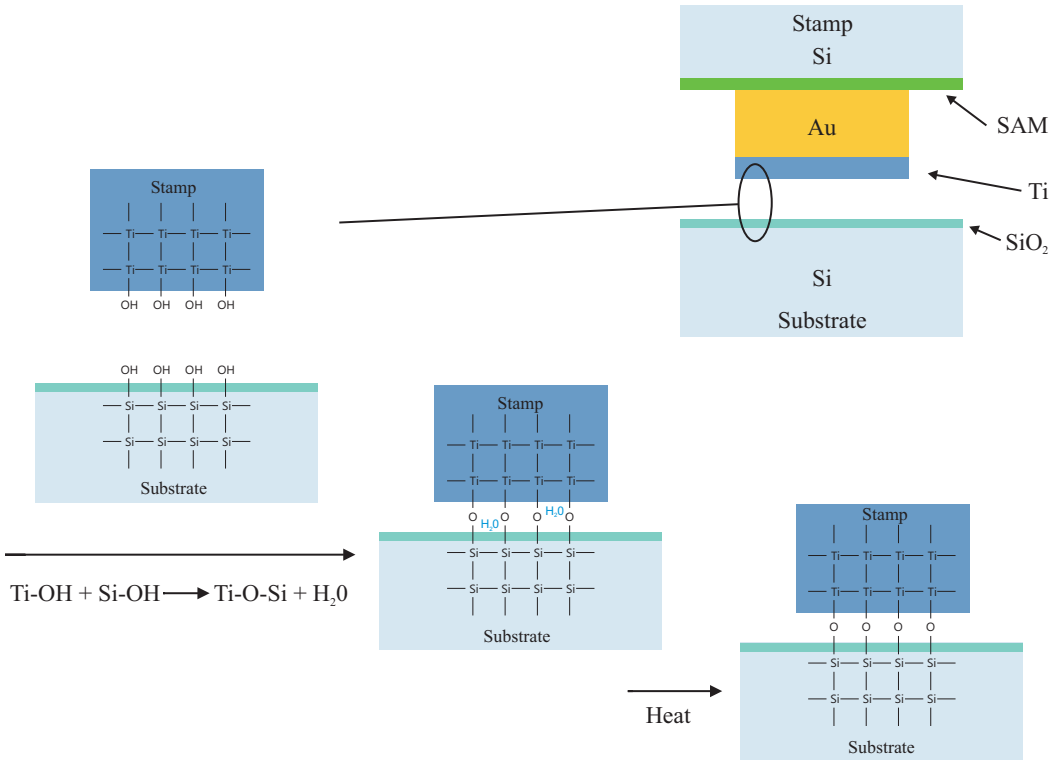

Figure 5.5: Interface chemistry during transfer process. Reprinted with permission from [44]. Copyright 2011 Taylor and Francis.

above 100°C which can be seen in Fig. 5.6. Therefore, temperature should be applied after pressure is applied in the transfer process to avoid destruction of the hydrophobic character of the Ti and the Si surface. With respect to this investigation, nanotransfer prints worked out not only for gold with a thin layer of titanium on top, but also for aluminum and Permalloy as these metals already contain –OH groups on the surface, as referenced above.

5.4 Structures fabricated with MBE stamps

In this section, a transfer-printing process using a stamp fabricated by molecular beam epitaxy (MBE) is introduced. The stamp fabrication involves the growth of a superlattice of GaAs and $Al_{0.8}Ga_{0.2}As$ lattice matched on a GaAs wafer. Since MBE growth has a resolution of one atomic layer, very thin and precise structure thicknesses can be achieved. After growth, a piece of the wafer with dimensions around 6 mm x 8 mm are cut out and than the breaking edge is selectively etched by citric acid or HF to selectively etch GaAs or AlGaAs, respectively.

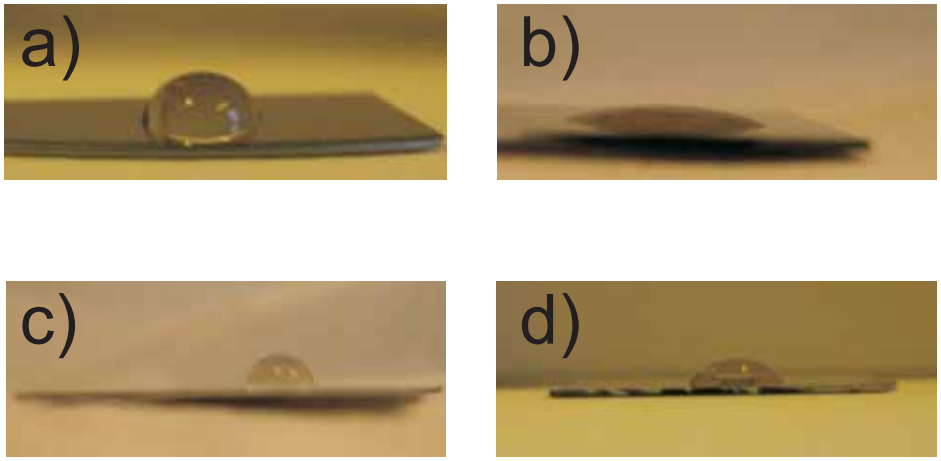

Figure 5.6: Hydrophobic and hydrophilic character of Si-wafer covered with Ti (a) before any treatment and (b) after UV and plasma treatment, respectively. After activating the Ti-surface, the hydrophilic character is lost under (c) vacuum conditions (10mbar) and (d) heat treatment (150°C). Reprinted with permission from [44]. Copyright 2011 Taylor and Francis.

In order to achieve a highly hydrophobic surface, since the structure will be used as a stamp, the surface can be either covered by a thiol based SAM or just oxidized naturally for one day. After that, metals can be deposited on top of the etched structures, wherein the first layer should be a noble metal and the last layer an adhesion promoter. The main process steps are shown in Figure 5.7.

Using a custom build nTP machine [23], the stamp is than pressed on a target substrate and the metals that are located on the stamp are transferred on the substrate. In Figure 5.8(a), an SEM image of the structures on a MBE stamp etched with citric acid are shown. The lines feature a width of 200 nm are spaced one from another by 200 nm. In Figure 5.8(b), lines that were transfer printed of that stamp on a Si wafer are shown. The transfer process has been carried out at room temperature and 300 MPa for 30 s. The length of the transferred structures is almost 2 mm and the lines are continuous [2].

By growing a thinner AlGaAs layer during the stamp fabrication process step, smaller structures can be transferred. In Figure 5.9a), we fabricated a single line having a width of 43 nm.

For the fabrication of nanoscale lines comprising a very small feature size, MBE stamps are excellent candidates. However for the fabrication of more complex structures, namely nano antenna arrays, this method lacks in printing efficiency and adjustment possibilities. We tried to fabricate a cross bar structure

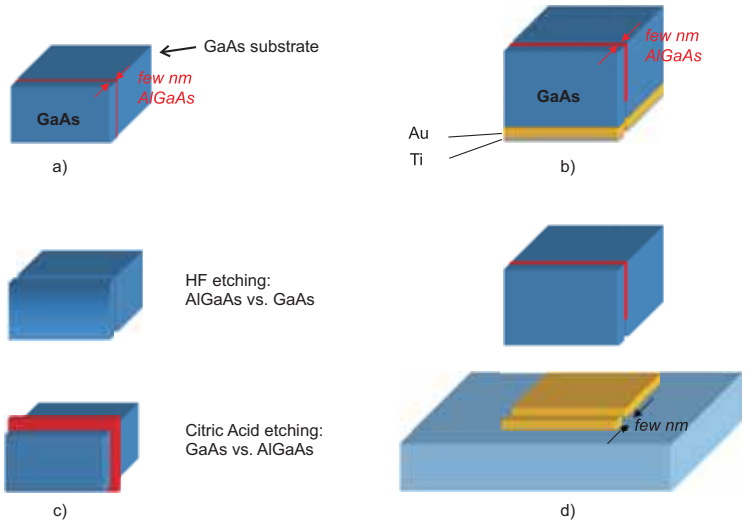

Figure 5.7: Fabrication of an MBE stamp for nanotransfer Printing. The stamp shown in this example could print one line (gap) of few nm width. (I): A small layer of AlGaAs is deposited on a GaAs substrate and covered with a GaAs Cap layer. (III): Selective etching can remove either the AlGaAs or the GaAs layers. (IV): Metal layers are evaporated on the stamp. (V): When brought into contact with a substrate, a small line (gap) is fabricated [23].

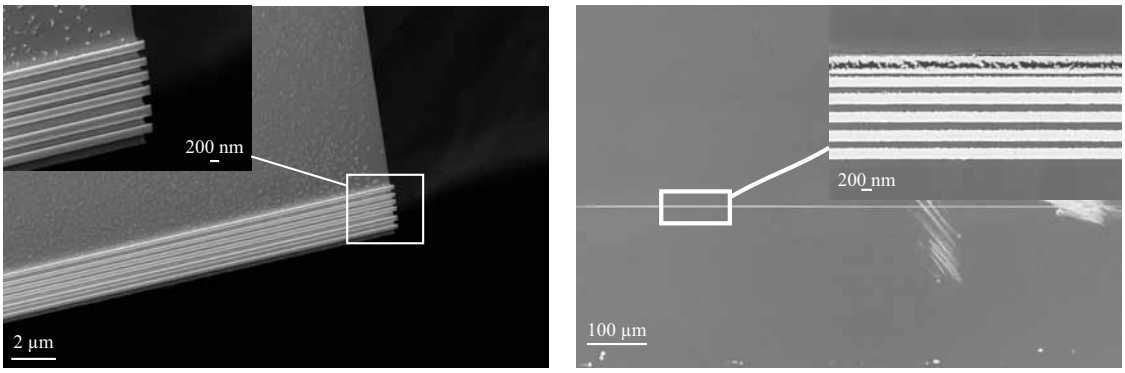

a) b)

Figure 5.8: (a) SEM image from MBE mold on the edge of a chip and (b) transfer printed gold lines. The MBE mold in this structure consists of six layers of 200-nm-thick AlGaAs separated by 200-nm-thick layers of GaAs grown on a GaAs wafer. After etching GaAs selectively, the structure results in six free-standing AlGaAs-bars (clearly visible in the inset) on the edge of the chip [2]. Copyright 2011 IEEE.

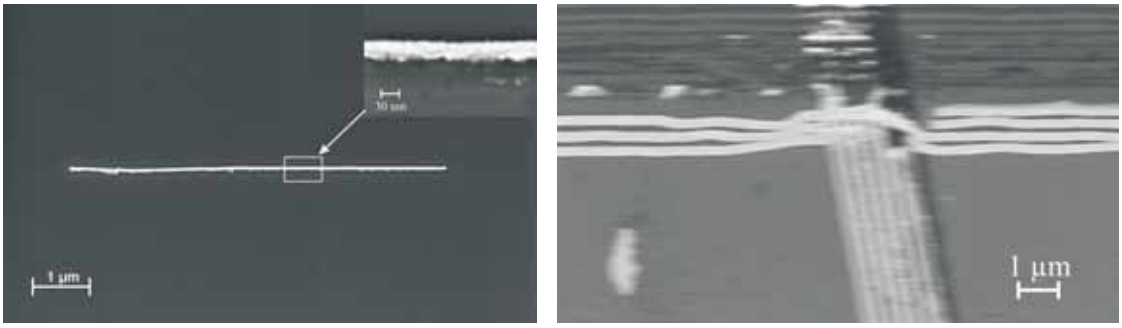

a) b)

Figure 5.9: a) SEM image of a transferred 30 nm wide and 34 nm high Au/Ti antenna. The width of the AlGaAs structure on the stamp was 30 nm. b) SEM image of a Cross Transfer of 200 nm wide gold lines. The height of the Au/Ti was 34 nm [8].

by printing a first bunch of lines and than rotating the substrate by 90° to print a second bunch of lines on top. Figure 5.9b) shows a typical image of such a two-step nTP with a MBE stamp. We use in the present work hard stamps, but a flat Si wafer features a small flexibility in the nanometer range that is sufficient to allow a stacking of two lines one over the other (see section 5.5). As the structures on the MBE stamp are not on the flat area located but on a breaking edge, flexibility is not given at all from that type of stamp. Therefore, for the fabrication of more complex structures like nano antenna arrays, flat Si wafer stamps are used.

5.5 Structures fabricated by Si wafer stamps

The previously presented approach using MBE stamps is an ideal method to fabricate small and dense lines. However, in order to cover large areas with structures or devices, Si wafer stamps are more suitable.

5.5.1 Fabrication of Si wafer stamps

Si wafer stamps featuring microscale structures were fabricated via optical lithography and reactive ion etching (RIE). A 2" Si wafer was covered with a positive photoresist, exposed to UV light through a mask in a maskaligner and developed resulting in areas in that the polymer was removed wherein on the remaining polymer the initial layer thickness remained unchanged. In a sub-sequential process step, the wafer was introduced into a RIE machine and the structures in the polymer was transferred into the Si. By that, a hard stamp featuring a 3-dimensional surface was created.

Our nanoscale Si wafer stamps were fabricated by the company IMS Chips (www.ims-chips.de). The fabrication method differed here by the fact that the polymer structuring was done via an electron beam. As a consequence, a different polymer that is sensitive to the electron beam was used by IMS Chips than the UV sensitive polymer that we used for the fabrication of our microscale stamps. The wafer that were used for the production of nanoscale stamps consist of a 4" Si wafers. Two typical nanoscale Si wafer stamps comprising pillars and lines are shown in Figure 5.10. Si wafer stamps with pillars, lines, cross bars or more complex structures like antenna arrays were fabricated. Since the structures were present on the flat Si wafer surface, a certain mechanical flexibility of the stamps is given that is necessary when after the transfer of a first layer, an additional second layer is transferred thereon.

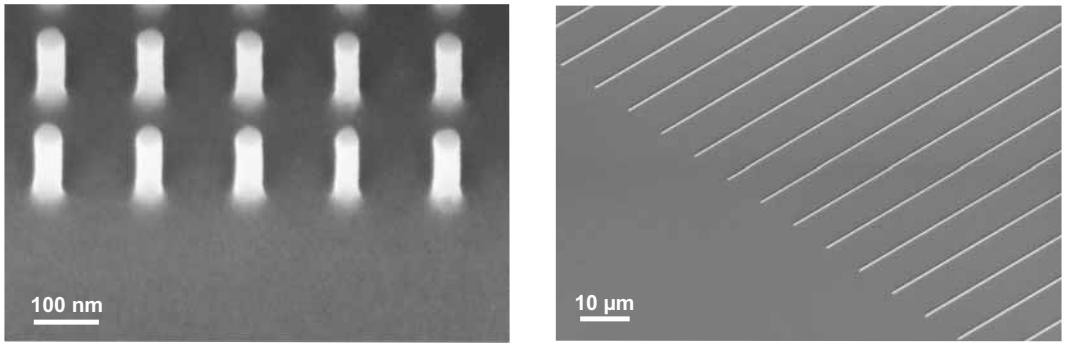

Figure 5.10: SEM image of two Si wafer stamps featuring (a) pillars and (b) lines.

5.5.2 Nanotransfer printing

Several structures were transfer printed over large areas (between 300 µm x 300 µm to 6 mm x 6 mm). Several material stacks were transferred always while the initial layer on the stamp being a noble metal and the last layer is an adhesion promoter. The transfer yield that is defined as the successfully transferred structures divided by the overall structures on the stamp is usually excellent with almost 100%. Lines, pillars and grid like structures were successfully transfer-printed. It turned out that the best materials for transfering are the material combinations of Au/Ti or AuPd/Ti. Some examples for succesfully transferred nanostructures are presented in Figure 5.11.

So far, transferring of single metal layers on flat substrates were demonstrated. However, for fabricating electronic devices more layers are necessary. We were able to transfer an additional layer of metal lines from a second stamp on the initial transfer-printed metal lines from a first stamp on a target substrate, namely a Si wafer. First of all, before transferring the second layer of metal lines, the target substrate comprising the metal lines from the first transfer needs to be activated. The activation of the Si substrate comprising a first layer of metal lines was done by a dry plasma treatment. After the activation, a second stamp comprising lines with the same material composition is also activated by a dry plasma treatment. After that, the target substrate with the first layer of metal lines is placed in the nanoimprinter. The second stamp is placed thereon. Care was taken that the line orientation of the transferred lines on the substrate and the lines on the stamp are 90° rotated with respect to each other. The orientation of the lines was checked before transferring in an AFM or SEM and marked on the stamp and on the substrate by a marker. The morphological investigation with a SEM proves the successful two step transfer over a large

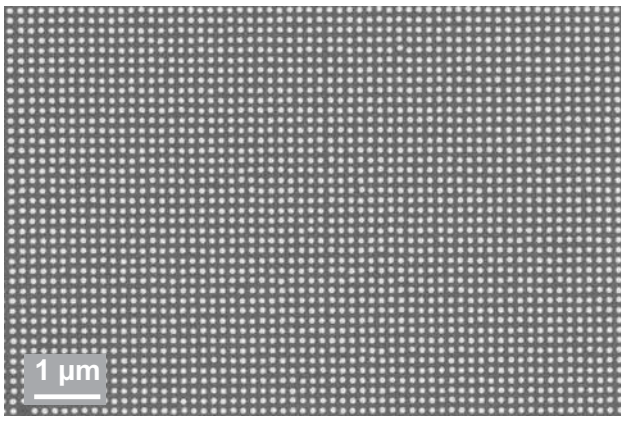

a)

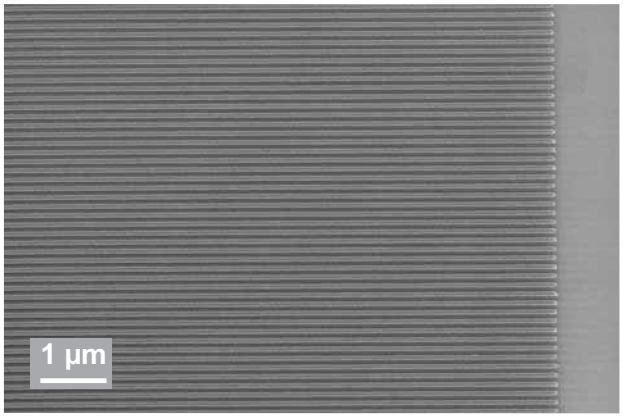

b)

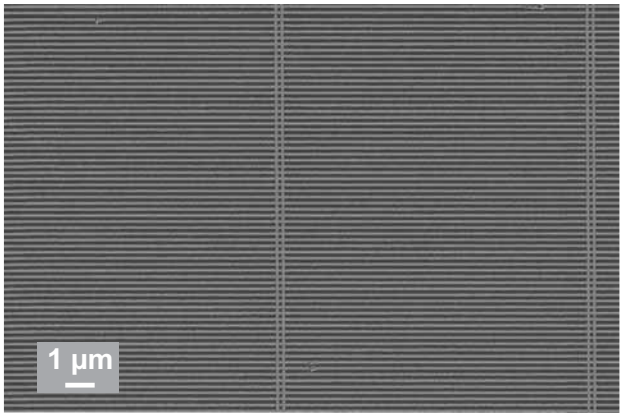

c)

Figure 5.11: SEM and AFM images of transfer-printed structures: (a) Pillars (b) lines and (c) grid like structures comprising 25 nm of Au and 4 nm of Ti were transferred on a Si wafer.

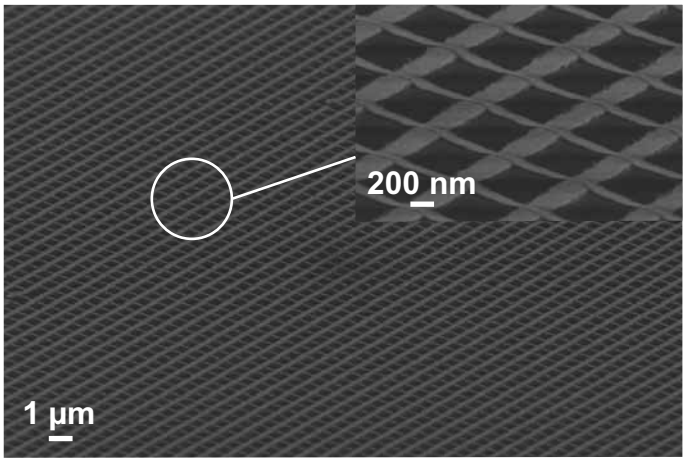

Figure 5.12: SEM image of two step transfer printed cross bars wherein a first set of lines of Au (25 nm) and Ti (4 nm) was transferred on Si wafer and a second set of lines was transferred 90° rotated with respect to the initially fabricated lines comprising the same material composition.

area (Figure 5.12). AFM investigations proves that the second layer is laying over the first one wherein in the gaps of the first layer, the metal structures are hanging over the substrate without touching when the distance of the lines between each other of the first stack is below 100 nm. When the distance of the first layer of lines is above 100 nm, the second layer of lines is actually touching the surface of the Si wafer.

A challenge occurs in the two step transfer process when using Si wafers comprising a thermally grown SiO_2 layer beyond the first set of transfer-printed metal lines. For SiO_2, a RCA 1 clean is necessary for activating the substrate. In a two step transfer process, this would mean that the first layer of metals is etched away. Therefore, when an insulating substrate is required, glass is the material of choice, since it can also be activated by a brief plasma treatment.

We further show that the target substrate must not be a plane substrate for transferring materials thereon. We demonstrated that a pre-structured surface can be further processed by a nTP process. A 15 nm thick thermally grown SiO_2 on a highly doped Si wafer was structured via optical lithography and dry etching. In this way, a "window" is created in the SiO_2 layer. A set of Au (25 nm) - Ti (4 nm) - lines was printed over that "window" connecting both sides of the SiO_2 layer(see Figure 5.15). This design can be used in the fabrication of transistor featuring ultra-thin gate dielectrics.

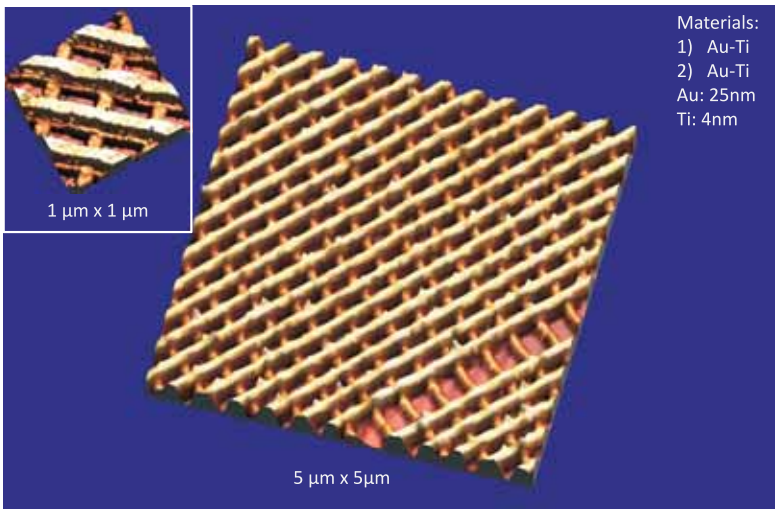

Figure 5.13: AFM image of two step transfer printed cross bars wherein a first set of lines of Au (25 nm) and Ti (4 nm) was transferred on Si wafer and a second set of lines was transferred 90° rotated with respect to the initially fabricated lines comprising the same material composition.

5.6 Conclusions

In this chapter, we discussed the importance of two main process parameters, namely the hydrophilictiy and the temperature. With respect to the temperature dependency we found that the formation of metal-oxygen-silicon bonds produces a strong bonding between the metal to be transferred and the substrate. We pointed out that the release from the interface of water formed in this process is important in order to achieve a durable bond, as the connecting process is reversible. This can be done by applying temperatures of around 200°C or by establishing vacuum conditions during the transfer process. Treating temperature as a further process parameter in the nTP method improved the process strongly and allowed us to effectively transfer several metal nanostructures over large areas. It should be emphasized that the metals and the substrate must have –OH groups on their surfaces which can be obtained by chemical or optical treatments. In particular, the transfer of small dots of Permalloy can lead to promising applications [96]. Permalloy is a magnetic material and by arranging small magnetic dots, these nano magnets can provide logic circuits [97, 98]. For constructing a computing device, a large amount of nano magnets are necessary, which is a slow and costly fabrication process using electron beam lithography. Nanotransfer printing of a large area of Permalloy dots is a technical solution to

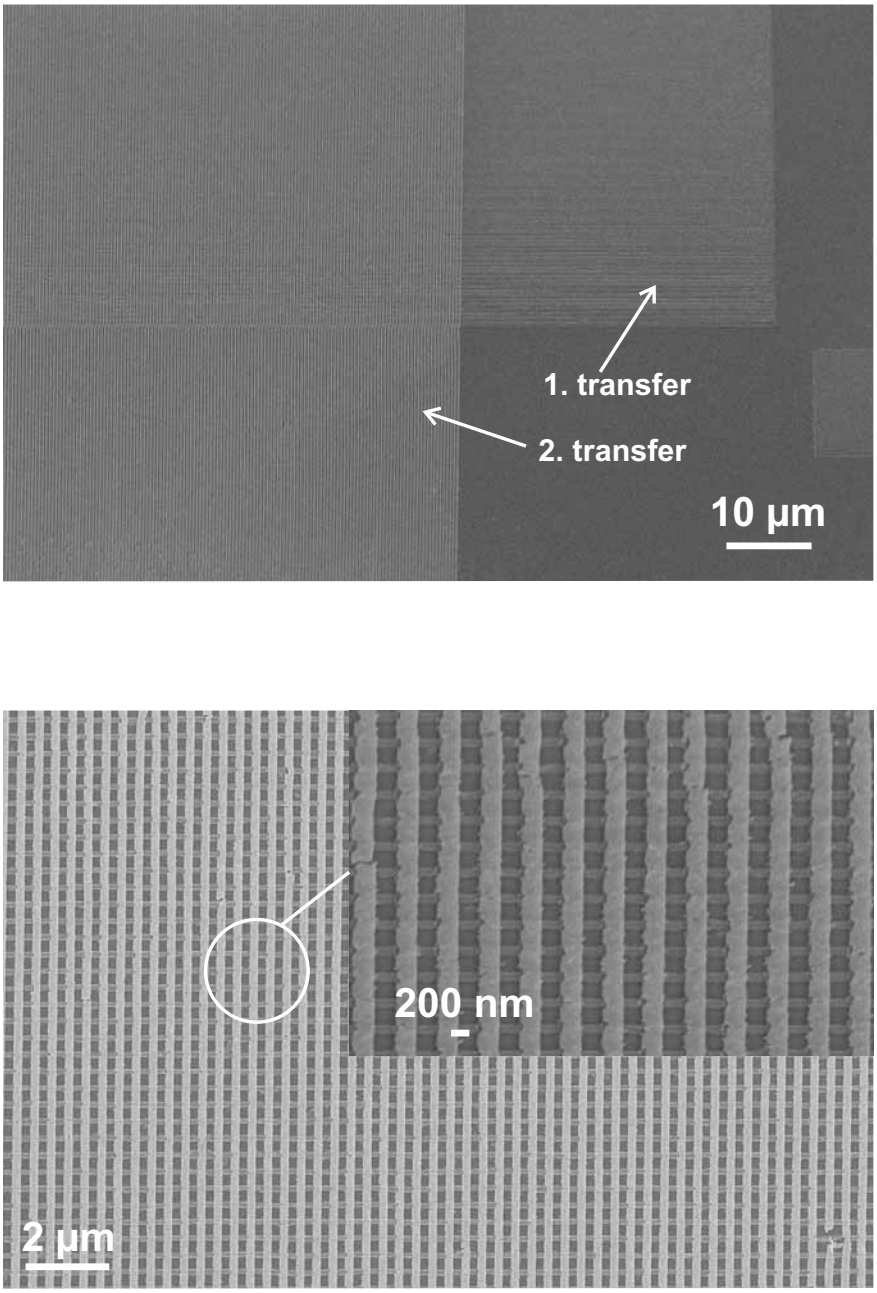

Figure 5.14: SEM image of two step transfer printed cross bars: (1) A first set of lines of Al (25 nm) and Ti (4 nm) was transferred on Si wafer and a second set of lines was transferred 90° rotated with respect to the initially fabricated lines comprising the of Au (25 nm) and Ti (4 nm). (2) The first set of lines was fabricated via NIL and lift-off and consisted of Al (25 nm) and Ti (4 nm).

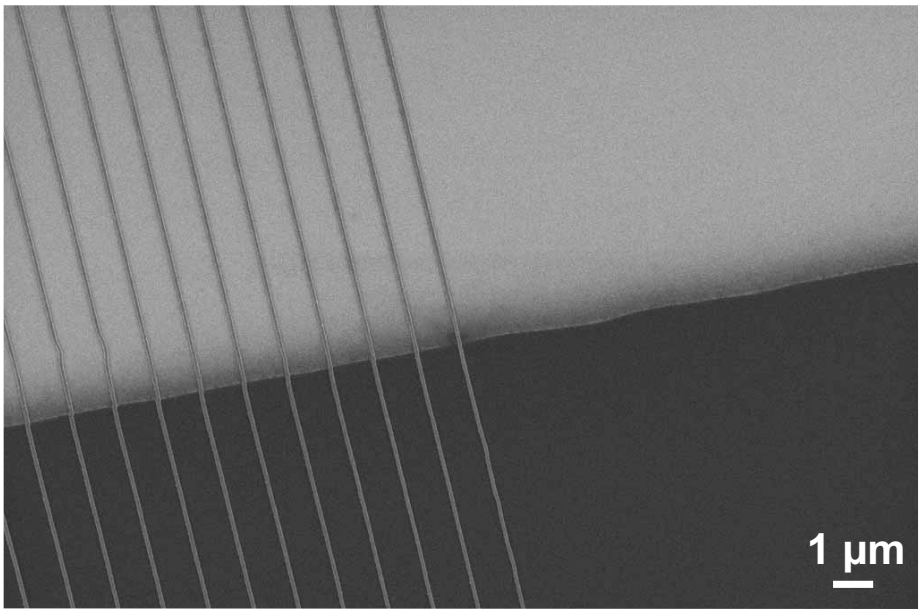

Figure 5.15: SEM image of transferred Au lines over an etched SiO_2 window.

this issue.

Further, we showed two approaches of nTP using MBE stamps and Si wafer stamps. Individual and ultra-small lines were fabricated using MBE stamps. Large areas were covered with metal lines and pillars using Si stamps. We also showed that more complex structures like grids can be fabricated in a two-step nTP process. Even transfers over edges is possible and in this way two different material layers that are vertically spaced can be connected.

Chapter 6

Metal-insulator-metal (MIM) tunneling diode

In this chapter, the metal-insulator-metal (MIM) tunneling diode is discussed in detail since this device represents the most important and challenging part in the nano antenna array. A short introduction to the theoretical background of MIM diodes is given which has been previously presented in parts in [7, 8]. After that, the different types of dielectrics in MIM diodes are briefly discussed. Then, the fabrication of microscale and nanoscale MIM diodes featuring a AlO_x and a TiO_x dielectric are presented. Parts of these results have been published in [2, 3, 7, 11, 65].

6.1 Theory of MIM diodes

Metal-insulator-metal (MIM) tunneling diodes represent important devices in the fields of electronic circuits, detectors, communication, and energy, as their cut-off frequencies may extend into the THz "gap" between the electronic microwave range and the optical long-wave infrared regime 6.1. [7]. Besides the high cut-off frequencies, MIM diodes feature a non-linear I-V-characteristics. When metals with dissimilar work functions are used, an asymmetric current with respect to the polarity of an applied bias across the junction occurs. This leads to a rectifying behaviour of the MIM junction. Summarizing, since MIM diodes may be designed to follow high electrical currents (e.g. in the THz range) and feature an asymmetric behaviour at 0 V, these devices represent an unbiased and high frequency diode. In the present work, antenna arrays have been realized that are sensitive to infrared radiation via absorption of electromagnetic radiation. MIM diodes are excellent devices for converting the high alternating current (AC) generized in the antennas into DC. They are therefore coupled to these antennas. Conventional diodes, like Schottky diodes or p-n junctions are usually not fast enough to follow this high frequencies. Tunneling provides a

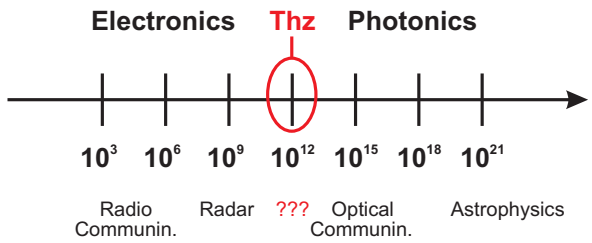

Figure 6.1: The working range of devices with respect to the frequency is shown. A gap between electronics (lower frequencies) and photonics (higher frequencies) is in the THz regime where very few devices are able to work.

conduction mechanism that allows diodes to be sufficiently fast. An overview over the theoretical background, the fabrication, and characterization is given in this chapter.

The physical and energetic structure of a MIM diode is shown in Figure 6.2. The basic structure of a MIM junction consists of an oxide layer of thickness d, surrounded by two metals. The bandgap of the insulating oxide represents a barrier for electrons in the metals. The metal bands are filled with electrons up to the Fermi energy E_F. The work functions φ_1, φ_2 of the electrons and the work function of the insulator (oxide) determine the barrier heights φ_{b1} and φ_{b2}. Since the barrier heights for the electrons are much smaller than the one for the holes, the contribution from the holes to the overall tunnel current can be neglected.

In general, electronic tunneling is a quantum mechanical process in which an electron described as a probability wave functions that penetrates into a tunnel barrier which is forbidden to classical particles. When the tunnel barrier is thin enough, a non-negligible probability exists that the electronic wave does not only penetrate into the barrier but has also a sufficient large value on the other side of the barrier. In this case, electrons can tunnel through that barrier. In a one-dimensional problem, the probability $D(E_x)$ for an electron to travel through a barrier is given by equation 6.1 wherein a general barrier $V(x)$ is assumed.

$$D(E) = exp\left\{-\frac{4\pi}{h}\int_{x_1}^{x_2}[2m(V(x)-E_x)^{\frac{1}{2}}]dx\right\} \tag{6.1}$$

where x_1 and x_2 define the edges of the barrier of thickness d, E_x is the energy component of the electron in the x direction and m is the electron mass.

Finally *Simmons* [100] showed that:

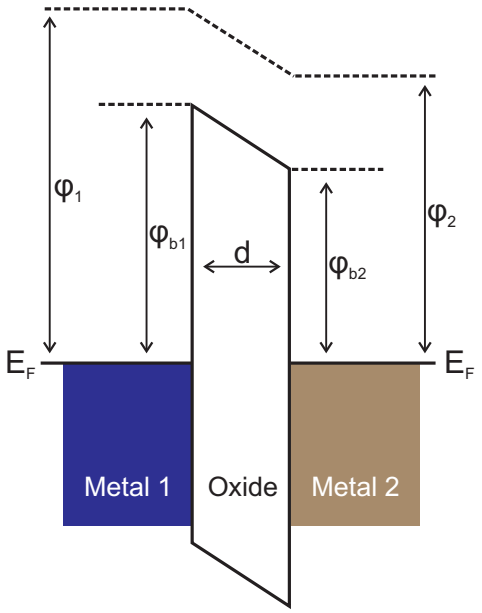

Figure 6.2: Banddiagram of a MIM diode in equilibrium with two metals of different electronic work functions φ_1 and φ_2. d is the thickness of the insulator and E_F is the Fermi energy of the electrons in the conduction bands. [8, 99]

$$N = \int_0^{E_m} D(E_x)dE_x \cdot \left\{ \frac{4\pi m^2}{h^3} \int_0^{\infty} [f(E) - f(E + eV)]dE_r \right\} \tag{6.2}$$

where E_r is the energy in the y and z direction: $E_r = m(v_y^2 + v_z^2)/2$ and $f(E)$ is the Fermi distribution in electrode 1. If a voltage is applied on electrode 2 (electrode 1 being grounded) the Fermi distribution of electrons on this side gets dependent on the voltage: $f(E + eV)$. Quantum mechanical tunneling through a high barrier is depending very weekly on the temperature. The only contribution is the temperature-dependent Fermi function.

Different regimes of tunnel currents are defined commonly and will briefly discussed here:

Direct Tunneling For low-voltage regime below the corresponding φ_{b1} and φ_{b2}, electrons can tunnel from one electrode to the other (see fig. 6.3(b)) through the whole barrier width, which is called direct tunneling. For small applied voltages, the current density is directly proportional to the applied voltage V. This is an Ohmic behavior with high resistivity. For intermediate voltages, $V < \varphi_{b1,b2}/e$, the current starts to increase exponentially with voltage [8, 100].

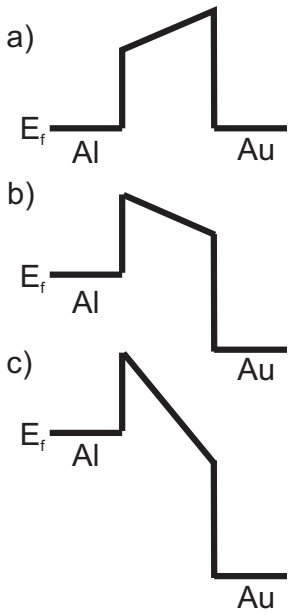

Figure 6.3: Banddiagram of a MIM diode under applied voltage [8].

Fowler-Nordheim Tunneling The high voltage range is called 'Fowler-Nordheim regime', first described by Fowler and Nordheim in 1928 [101]. Electrons first tunnel from electrode 1 to the conduction band of the insulator before reaching electrode 2 (see fig. 6.3(c)). This means that the effective thickness of the tunnel barrier is decreased

By considered that the barrier thickness Δd becomes dependent on the voltage when the voltage for $V > \varphi_{b1,b2}/e$ the effective barrier thickness is in first approximation: $\Delta d = d\varphi_{b1,b2}/eV$. That means that the potential barrier has in the 'Fowler-Nordheim' regime a triangular shape.

For very hight voltages (e.g. negative voltages applied on electrode 1), the electrical current from electrode 1 to electrode 2 is dominant is given by [100]:

$$J = \frac{2.2e^3F^2}{8\pi h\varphi_0} exp\left[-\frac{8\pi}{3heF}(2m)^{\frac{1}{2}}\varphi_0^{\frac{1}{2}}\right] \tag{6.3}$$

wherein $F = \frac{V}{\Delta s}$ is the electric field across the barrier. The current density is proportional to $F^2 exp(-\frac{1}{F})$. The current-voltage-characteristics in the 'Fowler-Nordheim regime' feature a much higher slope with respect to direct tunneling which is obvious since the barrier thickness is decreasing with increasing applied voltage. This effect facilitate the determination of such regimes in practical applications since the change in the slope is drastic and takes place at voltages that corresponds to the tunneling barrier heights.

Some further effects can modify the I-V-characteristics of a tunneling current. A few of these effects are discussed in the following sections.

Image potential The energetic shape of the potential of the thin isolator between two metals in a MIM junction can be described as a trapezoidal form when no voltage is applied (see Fig. 6.3(a)). However, image forces in metals are known to reduce the potential barrier height [102]. The potential is better described like a hyperbolic function [100] which is lowering the tunnel resistivity. However, this effect is rather small in our case since the reduction of the barrier height is low and it is therefore neglected in the investigations done in this work.

Other tunneling mechanisms In the previous discussion about the tunneling mechanism, the electronic current occurred because of a modulation of the Fermi levels of the electrodes by an external voltage [103]. However, other effects can interfere with that conductive mechanism or even dominate:

- Trap Assisted Tunneling [104, 105]: The electron tunnel current does not take place from electrode 1 to electrode 2 directly, but due to trap states that are located in the dielectric. Thus, the overall current is a multiple step process, since the electron travels from electrode 1 through several trap states to electrode 2. Since trap states are almost always present due to defects, this mechanism can in general not be avoided completely. However, in the present work, this conduction mechanism is not the dominant one.

- Photon assisted tunneling [106]: An electron gains an effectively higher energy due to the absorption of a photon. Thus such electron has to overcome a lower barrier height of the dielectric or even has a thinner oxide to tunnel through ('Fowler-Nordheim regime'). When the photon energy is higher than the tunnel barrier, the electron can even be lifted over the barrier (thermionic emission): In the case of an Al/Al_2O_3 interface the barrier height is ≈ 2 eV, which corresponds to a wavelength of 620 nm. Visible radiation around that value can contribute to the current through a MIM diode. In order to avoid photon assisted tunneling, measurements should be carried out without the influence of light.

All these mechanisms can occur simultaneously in a MIM diode. However, in general, one mechanism is dominating. For radiation in the far infrared this is tunneling due to Fermi level modulation [66].

Other conduction mechanisms besides tunneling Further conduction mechanisms through thin dielectrics are Poole–Frenkel conduction, Schottky conduction and hopping conduction [107]. Schottky conduction in MIM structures

occurs when an electric field lowers the barrier to thermal emission of electrons at the metal–insulator interface. Poole-Frenkel conduction depends on the lowering of the depth of traps in an insulator by an electric field, while hopping is a conduction mechanism at low temperatures from one localized state to the other [108]. In the conditions of interest for the present work these mechanisms do not dominate over tunneling [8].

Rectifying mechanism of MIM diode As the tunneling current I_t is dependent exponentially [101] of the voltage V, the amount of tunneling electrons with respect to the polarity of the electron flux is different when an alternating field is applied on the MIM structure under an external bias [61]. For example, when a constant voltage of 2 V is applied to one metal with respect to the other one and in addition to that, an AC field of 100 mV is applied, more electrons are tunneling from the electrode that is positive biased (DC) to the electrode that is negative biased (DC) than the other way and thus, a direct current is formed. The conversion from AC to DC is more efficient when a larger voltage is applied because of the exponential I_t-V-characteristics. Therefore, MIM diodes used as detectors should be able to substain large voltages. When fabricating MIM diodes containing work functions with dissimilar metal electrodes like gold as the first electrode and aluminum as a second electrode, an asymmetric slope of the I_t-V-characteristics is achieved even when no biased is applied to the junction [2]. In such a structure, the electrons have a higher effective energy barrier when tunneling from the high work function material to the low one than in the other way. Thus, an effective direct current flows from the low work function material to the high work function material [7]. Figure 6.4 shows the conduction band structure of MIM junctions with metals featuring equal and dissimilar work functions with and without applied biases.

The cut-off frequency f_{Cutoff} of a MIM diode is defined as:

$$f_{Cutoff} = \frac{1}{2\pi R C_D} \tag{6.4}$$

wherein R is the resistance of the electrical contacts. C_D is the capacitance of the diode [66]. Assuming a parallel plate capacitor for the MIM structure, the capacitance can be calculated as

$$C = \frac{\varepsilon\varepsilon_0 \cdot A}{d} \tag{6.5}$$

where ε is the permittivity of the dielectric, ε_0 is the dielectric constant and A is the area of the MIM diode. Since infrared radiation induces high frequency currents in the terahertz range, the RC time constant has to be tailored to match a f_{Cutoff} in the terahertz range. For f_{Cutoff} = 30 THz,

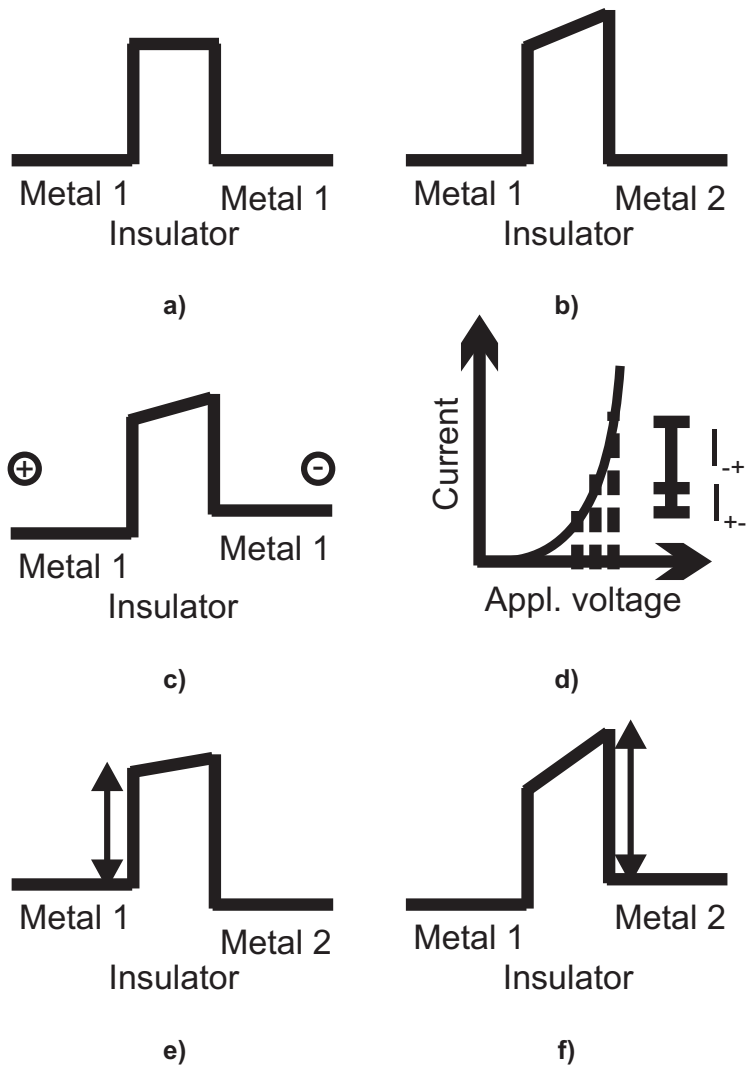

Figure 6.4: The conduction band structure of a MIM diode a) with equal metals and b) metals with dissimilar work functions is shown in steady state. When a voltage is applied on an electrode of the similar or dissimilar MIM diode, c) the Fermi-levels of the metals are not aligned anymore and an electrical current occurs. d) An AC signal that is applied in addition to the external bias (DC), displaces electrons from the cathode to the anode (I_{-+}) and the other way (I_{+-}) with the frequency of the AC signal. However, as the I-V-characteristics are exponential, the resulting direct current which is the difference between I_{-+} and I_{+-} is directed from the cathode to the anode. This asymmetric current is also achievable without an external bias when two metals with dissimilar work functions are used. When a surplus of electrons is formed in e) metal 1, the tunnel barrier for the electrons is lower than when a surplus of electrons is formed in f) metal 2 which results in an asymmetric current around zero volts. Reprinted with permission [7]. Copyright 2012 American Chemical Society.

an oxide layer thickness of 3.6 nm [43], the permittivity of aluminum oxide ($\varepsilon \approx 9$, [109]), and a resistance of R = 100 Ω [66], the capacitance has to be in the attoFarad range which in turn implies a diode dimension of approximately 50 nm x 50 nm. However, latest results show that a value for $\varepsilon < 6$ is here more reasonable and a resistivity for MIM structure less than R = 100 Ω has been reported [7], which relaxes the constriction on the diode area.

6.2 Dielectric fabrication methods

6.2.1 Aluminum oxide

The requirements for the dielectric materials in order to reach high-quality and reproducible tunnel current are fairly high. A pure and compact, thin insulator has to be fabricated. Different methods have been investigated and an overview is given here.

Naturally grown AlO_x The main insulating material used in the application of antenna-coupled MIM diodes has been so far native oxidized aluminum [66]. So far, single Al-AlO_x-Au diodes featuring a naturally grown insulator have been fabricated and showed an asymmetry around 0 V and a very large current density. This large current density can be explained by the relative thin dielectric which is known to be in the range to 2-3 nm. However, in our investigations, we found that about 90% of the diodes with the naturally grown AlO_x tunnel barrier showed short-circuit behavior, apparently due to direct contact between the top and bottom metal electrodes through the naturally grown AlO_x tunnel barrier. The current-voltage characteristics of the remaining 10% of the diodes showed extremely large device-to-device variations, suggesting that the thickness of the naturally grown tunnel barrier was different in each device (Figure 6.5). By fitting kinetic Monte Carlo simulations to the experimental data [110, 111] we have shown that the thickness of the naturally grown AlO_x is very inhomogeneous across the diode array and that the AlO_x thickness varied from less than 2.5 nm to about 3.6 nm. We did not find any diodes with an insulator thickness greater than 3.6 nm, which happens to be the thickness of the oxygen-plasma-grown AlO_x tunnel barriers (see section 6.3). We therefore conclude that this thickness of 3.6 nm is the maximum AlO_x thickness that is produced either by natural oxidation of aluminum in ambient air (although not homogeneously across a large area) or by plasma oxidation of aluminum with a plasma power of 200 W (with excellent uniformity across large areas). Unlike the MIM diodes with the naturally grown AlO_x tunnel barrier, which are neither reliable nor reproducible, the MIM diodes with the oxygen-plasma grown AlO_x tunnel barrier show excellent reproducibility (see section 6.3) [7].

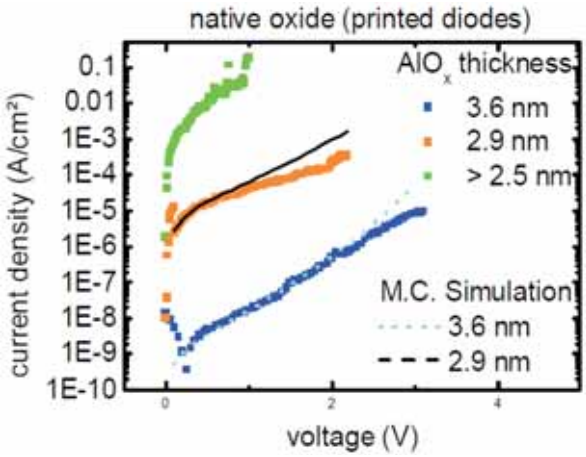

Figure 6.5: I-V- characteristics of printed MIM tunneling diodes featuring a naturally grown aluminum oxide as insulating material. The positive bias on Au is different for all three diodes, and the Monte Carlo simulation confirms that the thickness of the insulator is different in the three diodes, despite the same exposure time to air. Reprinted with permission [7]. Copyright 2012 American Chemical Society.

ALD fabricated Al_2O_3 Atomic layer deposition provides the possibility to fabricate thin layers of Al_2O_3 wherein in one cycle, exactly one layer of this material is grown. This is true after an initial layer thickness of around 6 nm is present. Before, islands are formed on the substrate which do form a closed film. Since a reliable and reproducible fabrication method of an insulator with an ultra-thin thickness of only a few nanometers is required, this fabrication method is here not suitable. However, for the fabrication of thicker oxides, this technology is excellent (see Fig. 6.6).

Plasma enhanced fabrication of AlO_x **with RIE** Reactive ion etching (RIE) is usually a method for etching anisotropic semiconductors and organic materials. There are few groups who also use that technology for the fabrication of high-quality oxides [43, 112]. In the present work, aluminum has been deposited by thermal evaporation on a substrate and than exposed to an oxygen plasma in a RIE machine for 30 s to 40 s at 200 W and 0.16 torr. In this way, oxygen atoms penetrates into the already native oxidized aluminum oxide and the pure aluminum located beyond. Therefore, a compact aluminum oxide layer is formed. The growth time is not a crucial parameter, since we determined a saturation thickness of 3.6 nm independent of the time (see also section 6.2.1). This fabrication method provides the thinnest dielectric with the highest quality and is therefore the fabrication technology of choice.

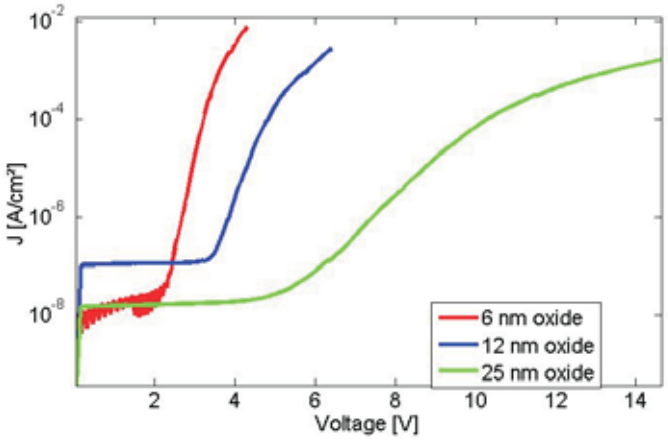

Figure 6.6: I-V-characteristics of Au-AlO_x-Au diode wherein the oxide was fabricated in an ALD process. The thickness of the manufactured oxides is between 6 nm to 25 nm [8].

6.2.2 Titanium oxide

Plasma enhanced fabrication of TiO_x with RIE Reactive ion etching (RIE) is also used in order to fabricate ultra-thin TiO_x on surfaces that are covered with Ti. The fabrication process is analogous to the fabrication of AlO_x. The resulting thickness is in the range of 2 nm.

6.2.3 Organic MIM diodes

So far, MIM diodes featuring a solid state dielectric have been discussed. The plasma induced fabrication of a dielectric with a RIE provides the possibility to manufacture a pure and compact dielectric. However, said fabrication method has one drawback. The thickness of the dielectric cannot be tailored by varying the plasma parameters as discussed in section 6.2.1. That is, a MIM diode comprising a reliable dielectric having a thickness of only 1 nm or 2 nm cannot be fabricated. Therefore, organic insulators, namely self-assembled monolayers (SAMs), have been investigated in order to fulfill the requirements of a MIM diode. SAMs are commercial available molecules featuring a chain of CH_2-groups, wherein either one end or both ends of the molecule have a functional group [113]. The functional group may consist of a silane, a phosphonic acid or a thiol group depending on which material, the SAM should adhere. Since the amount of C-atoms can be varied in the molecule synthesis the length of the molecule and therefore the thickness of the dielectric can be tailored. In order to investigate this material system, test structures featuring a plasma induced fabricated AlO_x layer together with SAMs of different lengths were manufactured and characterized. In Figure 6.7 and Figure 6.8, the I-V-characteristics and

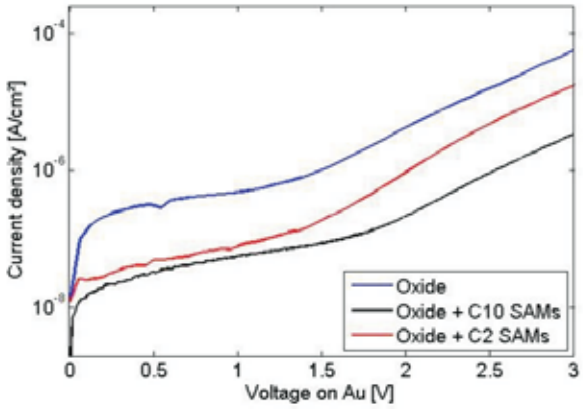

Figure 6.7: I-V-characteristics of an Al–AlO_x–Au diode with an additional layer of SAMs with different amount of C-atoms. The solid state dielectric was fabricated in a RIE enhanced plasma process. The diode area is here 60 µm^2 [8].

determined permittivity are shown, respectively. By increasing the amount of C-atoms in the SAM, the current is decreasing since the electrons have to tunnel through a thicker dielectric. The permittivity is also decreasing as expected.

However, we found that SAMs provide a dielectric suitable for tunneling only when they form a hybrid dielectric together with a solid insulator. Thus, the SAM layer is ideal for modifying the thickness of a dielectric, but having always a solid dielectric of a thickness of a few nanometers underneath. This hybrid insulataor is used in transistor technology [114]. Solely SAMs do not fulfil the requirements of being a compact insulator. We measured in a Au-SAM (bi-thiol with 8 C-Atoms)-Au structure only shortcuts which means that the SAM itself does not represent a compact dielectric like a solid state dielectric. Consequently, we choose solid insulators as the dielectrics of choice.

Up to now, we discussed the theoretical background of MIM tunneling diodes including different conduction mechanisms, several thin dielectrics and their fabrication methods. In the next sections, we will focus on the MIM device. Different microscale and nanoscale MIM tunneling diodes have been manufactured. We used plasma grown AlO_x and TiO_x, since these dielectrics feature the best properties with respect to the tunneling current and their permittivity which will be discussed in the following section in detail.

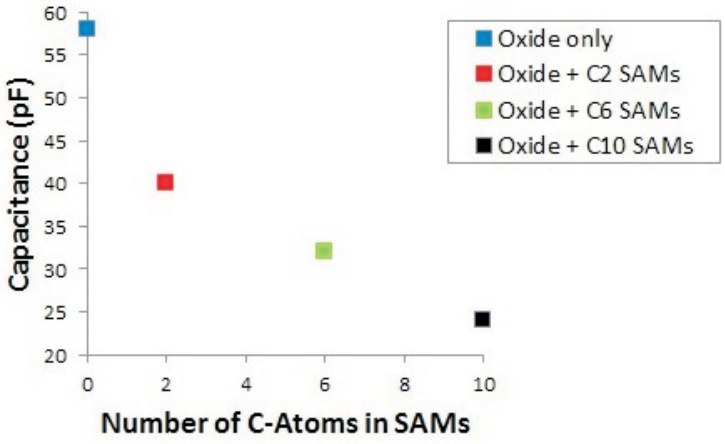

Figure 6.8: Capacitance measurements of diodes featuring a RIE grown AlO_x and SAMs as additional insulating layer. The diode area is here 60 µm^2 [8].

6.3 Microscale MIM tunneling diodes featuring a AlO_x dielectric

A silicon wafer covered with a hydrophobic organic self-assembled monolayer (SAM) of perflouroctyltrichlorsilane as an antisticking layer is used as a stamp. To create the hydrophobic SAM, the wafer is briefly exposed to an oxygen plasma (to create a density of hydroxyl groups sufficient for molecular self-assembly) [43, 115], placed for 30 min into a vacuum chamber along with 0.5 ml of perflouroctyltrichlorsilane at a pressure of 10 mbar, and then annealed at ∼140°C on a hotplate. The SAM coverage reduces the surface energy to 20 mJ/m^2 [116], making the wafer suitable as a stamp. Due to the excellent stability of silane SAMs on silicon [117, 118], the stamp can be utilized repeatedly without damaging the anti-sticking SAM.

The entire MIM tunneling diode is then created on the SAM-covered silicon stamp. First, a stack of 10 nm thick gold followed by 20 nm thick aluminum is deposited by vacuum evaporation through a shadow mask. This Au/Al stack later serves as the top electrode of the printed diode. The reason for depositing a stack of two different metals is that this makes it possible to choose a first metal (gold) that provides minimum adhesion to the fluoroalkyl SAM (to facilitate delamination from the stamp) and a second metal (aluminum) that can be plasma-oxidized to create a thin, compact tunneling dielectric (AlO_x). This oxidation is performed by a brief oxygen-plasma treatment that increases the thickness of the native AlO_x layer on the aluminum surface from ∼1.6 nm to ∼3.6 nm [114, 119, 120]. In the next step, a stack of 30 nm thick gold (as the bottom electrode of the printed diode) followed by 4 nm thick titanium (to

promote adhesion of the printed diode to the target substrate [77]) is deposited by vacuum evaporation through a second shadow mask. The titanium is allowed to oxidize and titanol surface groups are created by a UV and plasma treatment [88, 121].

Depositing the top and bottom electrodes through two different shadow masks makes it possible to also create a metal probe pad for each electrode to facilitate electrical characterization of the printed diodes. The active area of the diodes is the area by which the top and bottom electrodes overlap, as defined by the overlap of the designed shadow-mask features. The completed diodes ($Au/Al/AlO_x/Au/TiO_x$), including the probe pads are then transfer-printed onto the target substrate, namely a silicon wafer covered with a 200 nm thick layer of thermally grown silicon dioxide (Fig. 6.9). Prior to printing, the surface of the target substrate is exposed to an oxygen plasma, treated with HCl to form silanol surface groups [47] and then dried with compressed nitrogen. Transfer printing is performed using an Obducat NIL 2.5 Nanoimprinter at a temperature of 200°C and a pressure of 50 bar for 5 min. During the transfer process, the titanol and silanol surface groups on the stamp and on the substrate react to titansiloxanes under water release [93]. This reaction is strongly promoted by drying the surfaces prior to transfer and removing physisorbed water from the interface at 200°C during the printing process [95].

Several hundred MIM diodes were transferred from the stamp to the target substrate in a single printing step in normal laboratory environment (i.e. wihtout cleanroom). In order to quantify the mechanical yield of the transfer process, we have imaged the printed devices by scanning electron microscopy (SEM) and counted the number of diodes that appear to have been transferred properly (like the diode shown in Fig. 6.9) and those that appear to have been damaged or transferred incompletely. By defining the transfer yield as the number of diodes that appear in the SEM images as properly transferred divided by the number of diodes that were originally created on the stamp, the transfer yield is 83%. In Fig. 6.10, the transfer yield is plotted as a function of the active area of the tunneling diodes, which ranges over three orders of magnitude. As can be seen, the mechanical transfer yield is above 70% over the entire range of diode areas. The transfer yield appears to be limited by particles on the surfaces that prevent substrate and stamp from making physical contact, leading to damage or incomplete transfer. This may explain why the transfer yield appears to decrease for larger areas where the probability for features to overlap with particles on the surface is expected to be higher. Clearly, under cleanroom conditions this problem would be substantially less severe. Atomic force microscope (AFM) measurements performed on the diode structures prior to printing and after printing confirm the structural integrity of the transferred diodes, as the total thickness of the devices does not change upon transfer. These results show that

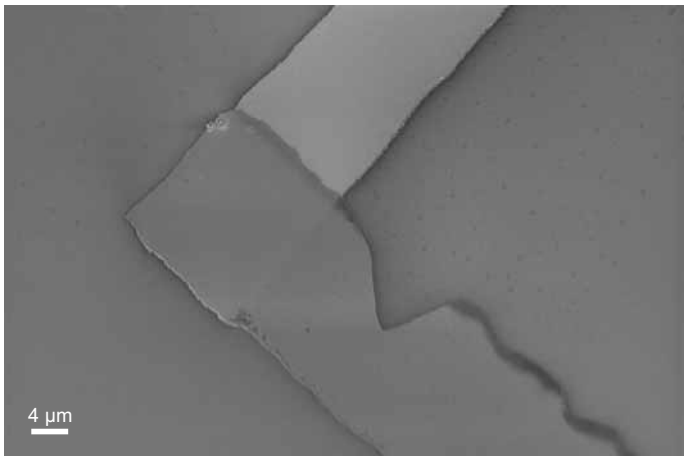

Figure 6.9: SEM image of a printed MIM tunneling diode. The substrate is a thermally oxidized silicon wafer. The MIM diode is defined by the overlap of the gold electrode located at the bottom and the aluminum electrode located at the top. The tunneling dielectric is 3.6 nm thick AlO_x produced by plasma oxidation of the aluminum electrode prior to Au evaporation and printing. The entire MIM diode was transferred from a stamp onto the target substrate in a single printing step. Reprinted with permission from [65]. Copyright 2012 American Institute of Physics.

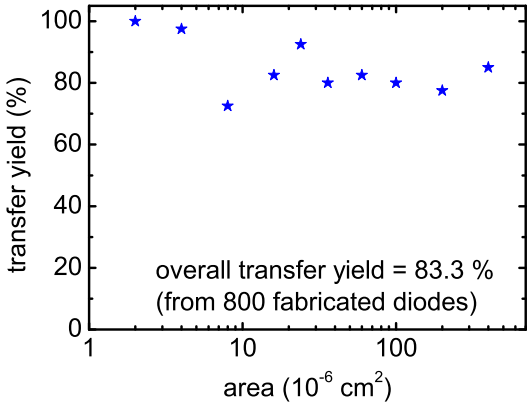

Figure 6.10: Mechanical yield of the transfer-printing process plotted as a function of the active area of the MIM tunneling diodes. As can be seen, a high yield of about 83% is obtained over a wide range of diode area. Reprinted with permission from [65]. Copyright 2012 American Institute of Physics.

by careful selection of materials and by adjusting the adhesive forces between the stamp surface and the top electrode as well as those between the bottom electrode and the surface of the target substrate, complete MIM diodes can be transfer-printed with large yield and excellent integrity.

The current-voltage characteristics of the transfer-printed MIM tunneling diodes are measured in ambient air at room temperature by contacting the printed top and bottom electrodes outside of the active diode area using probe needles and a parameter analyzer. In our measurements, the aluminum top electrode is set to ground potential, a positive or negative potential is applied to the gold bottom electrode and increased in small increments beginning from zero volts, and the current through the 3.6 nm thin plasma-grown AlO_x dielectric is measured as a function of the applied bias. In Fig. 6.11, the result of a current-voltage (I-V) measurement performed on a transfer-printed MIM diode is shown. In the graph, the absolute value of the measured current is plotted as a function of absolute value of the applied voltage, so that the asymmetry of the I-V curves can be easily evaluated. Symbols and lines represent experimental data and theoretical values, respectively. Comparing the slope of the I-V curve of a transfer-printed tunneling diode with that of a reference $Al/AlO_x/Au$ diode (not transfer-printed), it can be seen that the electron-transport mechanism in both structures is identical. Furthermore, the current densities in the transfer-printed diode and in the diode that was not printed are of the same order of magnitude, again confirming that the diodes are not damaged by the printing process.

An asymmetric slope of the two polarities was observed for larger voltages. For example, at a voltage of ± 3.5 V the current density due to electron injection from the gold electrode is around two orders of magnitude larger than for injection from the aluminum electrode. In order to identify the transport mechanism in the MIM diodes, the measured current was modeled using a kinetic Monte Carlo simulation [105, 122]. Electron tunneling was found to be the dominant mechanism, due to the very small thickness of the dielectric (3.6 nm). The resulting current density j can be described by the Tsu-Esaki formula [123]

$$j = \frac{e m_{ox} k_B T}{2\pi^2 \hbar^3} \int_0^\infty P\left(E_t\right) ln \left[\frac{1 + exp\left(\frac{-E_t}{k_B T}\right)}{1 + exp\left(\frac{-eU - E_t}{k_B T}\right)} \right] dE_t \tag{6.6}$$

where m_{ox} is the conductivity mass for the injected electrons, $P(E_t)$ is the transmission coefficient for electrons with transversal energy E_t, calculated in the Wentzel-Kramers-Brillouin approximation. A close agreement with the experimental data, as shown in Fig. 6.11, is achieved by assuming an effective tunneling mass of $m_{ox} = 0.38 \cdot m_0$ for the aluminum oxide, a tunneling barrier of 4.2 eV for the gold electrode, and 2.8 eV for the aluminum one.

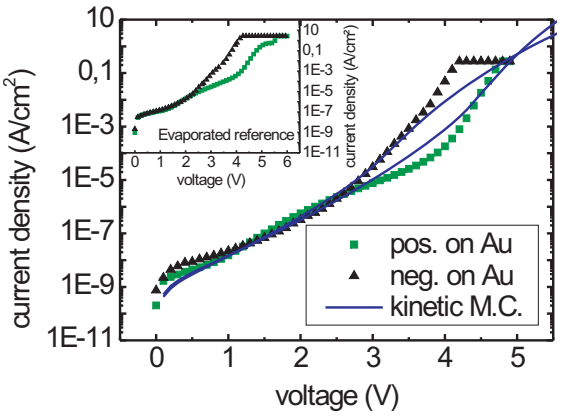

Figure 6.11: Current density through a transfer-printed MIM tunneling diode measured as a function of applied voltage for both polarities. The aluminum top electrode is set to ground potential, and the current is measured for positive (green data points) or negative (black data points) potentials applied to the gold bottom electrode. The lines represent the kinetic Monte Carlo simulation results using equation (6.6). In the inset the current-voltage curve of a transfer-printed MIM tunneling diode is compared to that of a diode based on the same material stack that was not transfer-printed. Reprinted with permission from [65]. Copyright 2012 American Institute of Physics.

As the work function of gold is $\Phi_{Au} = 5.2$ eV, the extracted barrier height of 4.2 eV corresponds to a gold/aluminum oxide interface at the Schottky limit, i.e. without any barrier reduction due to charge transfer across the interface. Correspondingly, a barrier height of 3.2 eV would be expected for the aluminum barrier (taking $\Phi_{Al} = 4.2$ eV), which is slightly larger than the extracted value of 2.8 eV. This discrepancy may be due to the formation of a dipole layer produced by charge transfer between the aluminum electrode and interfacial gap states in the aluminum oxide, which is known to reduce the barrier height [124, 125]. In general, the aluminum/aluminum oxide barrier height is known to strongly depend on, e.g., the growth method of the aluminum oxide [126]. For smaller voltages (0 to -2.8 V and 0 to +4.2 V) direct tunneling is the dominant transport mechanism. Minor deviations of the experimental data from the simulated curve for $|U| < 1$ V arise due to the relatively large applied voltage ramp which causes transient relaxation currents and charging of defect states. These dominate over the steady-state leakage current [127]. For voltages more negative than -2.8 V or more positive than +4.2 V the slope of the I-V curves increases. This well-known feature arises due to the transition from direct tunneling to Fowler-Nordheim tunneling, that is, a transition from a trapezoidal to a triangular tunneling barrier. Consequently, the barrier thickness decreases as the applied voltage is increased. For current densities $|j| > 10^{-2}$ A/cm^2, irreversible degradation of the tunneling diode during the measurement and finally short-circuiting was observed.

These results show that the electrical properties of the MIM diodes, including the thin aluminum oxide layer, were not noticeably altered or degraded by the transfer-printing process.

By measuring the surface roughness of the Au/Al/AlO_x layer after transfer printing with an AFM (see Fig. 6.12a), a RMS average value of 0.5 nm in intervals of 20 nm could be determined. The electrical field at local height peaks on the surface is higher than on a plane metal layer. Taking the roughness of the electrodes into account and thus the inhomogeneous field distribution including electrical field peaks, a better fit between the simulation (straight line in Fig. 6.12b) and the experimental data could be found. Static device parameters, namely the electron tunneling mass and the tunneling barriers of the Al-AlO_x and the Au-AlO_x interface, were carried out using said Monte Carlo simulation wherein the surface roughness of the interface was taken into account. An effective electron tunneling mass of 0.35 m_0, which is reasonable, and barrier heights of 3.3 eV and 4.3 eV for the Al-AlO_x and the Au-AlO_x barrier, respectively, were found. As aluminum oxide is known to have a work function of around 1 eV, the measured values of the barrier heights matches good to the theoretical values [3] and thus, these values substitute the values previously determined which do not include a roughness analysis.

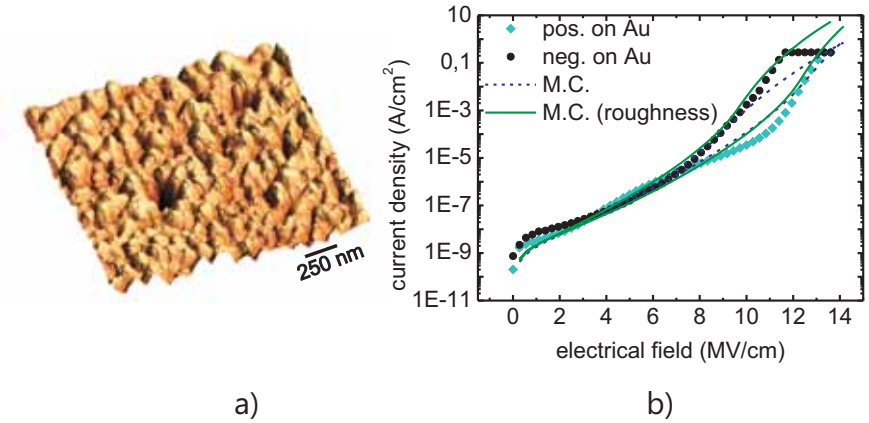

Figure 6.12: a) Roughness of the Al/AlO_x- layer determined via AFM and b) electrical characterization and simulations of a printed MIM tunneling diode (with and without roughness of electrodes)[3]. Copyright 2011 IEEE.

Building upon the parameters determined so far, the identification of the permittivity of the printed aluminum oxide is of great interest with respect to, e.g., the discussion of aluminum oxide as *high-k* dielectric [128]. The permittivity of the aluminum oxide layer of the printed tunneling diode was determined by capacitance measurements in which the aluminum electrode was set to ground potential and a dc voltage modulated with a small ac bias was applied to the gold electrode. A capacitance density of $1.19 \cdot 10^{-6}$ F/cm^2 was measured for the 3.6 nm thick oxygen-plasma-grown aluminum oxide layer of the transfer-printed MIM tunneling diodes. Modeling the MIM diode as a conventional parallel-plate capacitor with aluminum oxide as the dielectric [107], the permittivity can be calculated as

$$\epsilon = \frac{C \cdot d}{\epsilon_0 \cdot A}. \tag{6.7}$$

Here C/A is the capacitance per unit area, ϵ is the permittivity of the insulator, and d is the thickness of the insulator. For a dielectric thickness of 3.6 nm, a permittivity of 4.8 is calculated, which is much smaller than the values around 9 that are typically presented in literature for bulk aluminum oxide [109]. However, it is also well-known that reducing the thickness of aluminum oxide is often accompanied by a reduction of the permittivity [129]. This can also be seen in Fig. 6.13, where the permittivity of the printed tunneling diodes was compared to diodes in which the metals were evaporated and the aluminum oxide was deposited by atomic layer deposition (ALD). Unlike plasma oxygen, ALD allows us to set the thickness of the AlO_x-layer to any value. As has been pointed out

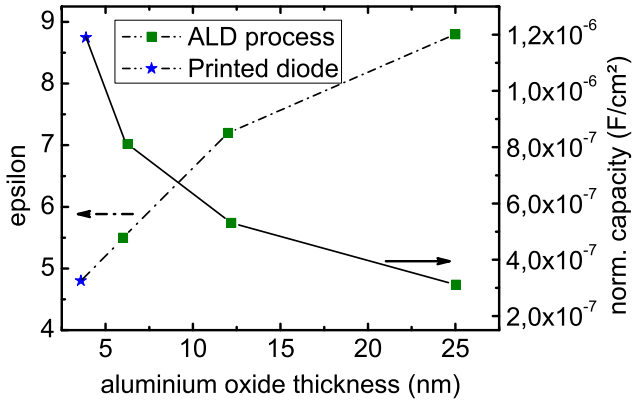

Figure 6.13: Measured capacitance of Al/AlO_x/Au diodes as a function of AlO_x thickness. The AlO_x film with a thickness of 3.6 nm was fabricated by plasma oxidation (as described in the text), while the thicker AlO_x films (6 nm , 12 nm, 25 nm) were deposited by atomic layer deposition (ALD). The permittivity calculated from the measurement data is also shown. Reprinted with permission from [65]. Copyright 2012 American Institute of Physics.

by Hickmott [130], extracting the permittivity of the dielectric by using equation (6.7), especially for thin-film capacitors, leads to erroneous results, i.e. to an apparent reduction of ϵ. In fact, the observed decrease of ϵ for ultra-thin films is due to interfacial capacitances at the metal-insulator interfaces. Thus, equation (6.7) should be replaced by

$$\epsilon = \frac{1}{\epsilon_0} \cdot \frac{1}{\frac{A}{C} - \frac{A}{C_I}} \cdot d \tag{6.8}$$

Here, C_I is an interface capacitance that depends on the metal contacts and is connected in series with the capacitance of the dielectric film. More precisely, C_I is not a property of the chosen metal-dielectric combination, but was found to depend on the deposition method of the metal electrode. It was concluded that the interface capacitance is not caused by the field penetration into the metal electrodes, as suggested by Mead [131]. Instead, it is due to the occurrence of interface states at the metal-dielectric interface which depend on the deposition conditions of the metal electrodes.

In this section we presented the fabrication and characterization of transfer-printed MIM tunneling diodes with gold and aluminum electrodes and a 3.6 nm thick, oxygen-plasma-grown aluminum oxide dielectric. We have shown that the dielectric retains its high quality during the transfer-printing process. Tunnel currents have been measured over eight orders of magnitude, including the transition

from direct tunneling to Fowler-Nordheim-tunneling. The asymmetric behavior of the printed MIM diodes makes it possible to use them as rectifying devices. By comparison to a theoretical tunneling model, the static electronic properties of the diodes, i.e. the tunneling barrier heights and the tunneling effective mass, have been determined. Capacitance measurements performed on the printed devices indicate a permittivity of about 5 for the 3.6 nm thick aluminum oxide films, which is in line with previous investigations. As the mechanical yield of the transfer-printing process is above 80% (and even higher for smaller structures), we believe that transfer-printing is an efficient and economical process to cover large areas with rectifying MIM tunneling diodes without affecting the electrical performance of the diodes. The process can be further scaled down to arrays of nanometer-size MIM diodes to be transferred. This is presented in the next section.

6.4 Nanoscale MIM tunneling diodes featuring a AlO_x dielectric

In this section, we show, based on the previously fabricated microscale MIM diodes, the production of several millions of nanoscale MIM tunneling diodes featuring a AlO_x dielectric.

As already discussed in chapter 5, electron-beam lithography (EBL) [9, 30] is a commonly used method for patterning materials and fabricating devices with dimensions between 30 and 100 nm in research. However, EBL lacks the fabrication speed and cost efficiency required for the processing of large areas. In contrast, nanotransfer printing (nTP) offers the possibility to print large, dense arrays of nanoscale devices on arbitrary flat surfaces, provided that the adhesive and cohesive forces, the surface energies and the material properties are properly tailored [47]. Using temperature-enhanced nTP, we have fabricated an array of approximately 4 million MIM pillar diodes, each with a diameter of less than 100 nm, suitable for electronic and optoelectronic applications.

First, a stamp was designed and fabricated from a silicon wafer by EBL and highly anisotropy reactive ion etching (RIE). The stamp contains an array of cylindrical mesas covering a square area of 300 x 300 µm (see Figure 6.14a for a schematic and Figure 6.15a for an electron microscopy image). Successful transfers with stamps up to 1 cm^2 have also been performed. The mesas have a height of 80 nm to provide good physical stability during the printing process. The diameter of the mesas and the spacing between adjacent mesas was designed between 50 and 100 nm.

The preparation of the stamp prior to printing is outlined in Figure 6.14b-e. First, the stamp was covered with an alkylsilane self-assembled monolayer (SAM) to reduce its surface energy. Next, a 15 nm thick layer of AuPd was deposited by thermal evaporation onto the SAM-covered stamp to provide a delamination layer from which the MIM pillars can later be easily transferred to the target substrate. In the next step, a 25 nm thick layer of aluminum with a surface roughness of less than 1 nm was deposited as the first electrode. The stamp was then briefly exposed to oxygen plasma to form a high-quality aluminum oxide tunnel barrier with a thickness of 3.6 nm [112]. As far the larger diodes, the oxygen-plasma-grown oxide has been found to provide substantially better reliability and reproducibility compared with aluminum oxide obtained by native oxidation in air. To complete the MIM structure, a 15 nm thick AuPd layer was then deposited as the second electrode. Finally, a 4 nm thick layer of titanium was deposited by evaporation to provide an adhesion promoter for the nanotransfer printing process. In order to facilitate good physical contact between the stamp and the target substrate, the layer stack deposited onto the stamp must be as smooth as possible. Therefore, metals with a small grain size, such as Al, AuPd, and Ti, are more desirable than, e.g., Au. During the metal evaporations the stamp was held perpendicular to the metal source in order to minimize the deposition of metals on the sidewalls of the mesas (see Figure 6.15b) and Figure 6.15c)).

As target substrate we have used a p-type silicon wafer covered with an AuPd layer (to electrically connect the bottom electrodes of all diodes) and a thin titanium layer (to provide good adhesion of the printed layer stack). Immediately prior to printing, the titanium-coated surfaces of the stamp and the target substrate were physically activated (the parameters can be found in the appendix). When the titanium-covered MIM pillars on top of the mesas of the stamp are brought into physical contact with the titanium-covered target substrate, individual and isolated MIM nanodiodes are transferred from the stamp to the substrate, resulting in a high density of devices. The transfer process is facilitated by applying a temperature of 200°C during printing. We found that such a high temperature promotes the formation of covalent bonds between the titanium layers on the top of the stamp and on the substrate due to the removal of water molecules [44].

In order to investigate the quality of the nTP process, three nominally identical samples were fabricated and investigated by scanning electron microscopy (SEM). The transfer yield was found to be 98%, which means approximately 4 million diodes were successfully transferred. During the metal and insulator deposition process, some material is deposited not only on the top of the pillar structures of the stamp, but also around the periphery of the previously

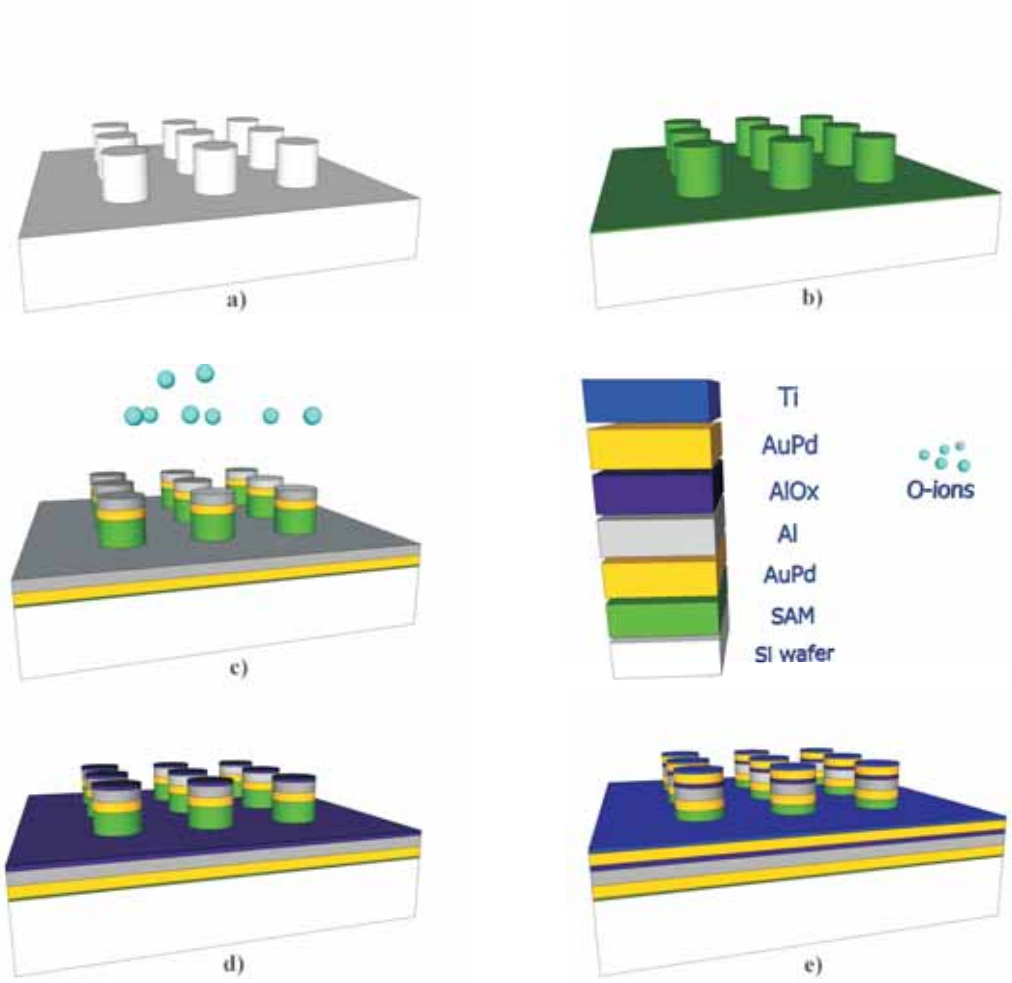

Figure 6.14: a) An array of mesas with a height of 80 nm and a diameter of 50 to 100 nm is fabricated on the surface of the silicon stamp by electron-beam lithography and highly anisotropic silicon etching. b) The silicon stamp is covered with an alkylsilane self-assembled monolayer (SAM). c) 15 nm of AuPd and 25 nm of Al (first electrode of the MIM diodes) are deposited by thermal evaporation. d) The Al surface is exposed to oxygen plasma to form a 3.6 nm thick AlO_x tunnel barrier. e) Finally, 15 nm of AuPd (second electrode of the MIM diodes) and 4 nm of Ti (to promote adhesion to the target substrate) are deposited by thermal evaporation. Reprinted with permission from [7]. Copyright 2012 American Chemical Society.

deposited metal stack (although not on the sidewalls of the pillars). Therefore, the area of the MIM structure increases with increasing metal layer thickness. Indeed, the diameter of the transferred quantum devices was found to be larger by about 45 nm than the original feature size on all three stamps. Taking these effects into consideration, the diode area and the distance from each other can be tailored very precisely, and nanoscale structures with a very high density can be fabricated. In order to compete with high resolution EBL fabrication techniques, the morphology and height of the printed devices have to be homogeneous and to remain unchanged after the printing process. The fidelity of the printing process is proven by the perfect match between the height of the transfer-printed MIM diodes, measured with an atomic force microscope (AFM) and the evaporated material thicknesses on the stamp. The printed quantum pillars have a height of 60 nm and feature a stack shape expected from the original layer depositions on the stamp.

So far, we have therefore demonstrated that several millions of MIM nanodiodes can be fabricated by a few evaporation steps and a fast printing process, without need of resists or other patterning steps (other than those used to make the stamp), followed only by some plasma treatments. Thus, temperature-enhanced nTP provides a solution to the challenge of fabricating large-scale and high-density homogeneous arrays of nanoscale devices in a fast and economic way. The stamp can be used several times before degradation occurs. However, the electrical characterization of individual diodes is challenging since the contact area is fairly small. Indeed, the top surfaces of the transferred tunneling diodes are very smooth, thus providing an excellent contact area for electrical characterization with a conductive AFM tip which allows the contacting of nanometer-scale electrodes.

The electrical properties of the transfer-printed MIM nanodiodes have been quantified using a conductive atomic force microscope (C-AFM). With this high spatial resolution characterization method, several nanodiodes have been tested individually and the static device parameters of single nano devices have been extracted, allowing us to investigate the underlying electron transport mechanism. The conductive AFM tips consisted of silicon covered by a Pt-Ti alloy and featured a tip radius of 15 nm. The electrical set-up allowed to locally apply voltages up to 10 V and to measure the current at the same time. The sample with the printed rectifiers was placed on a ceramic holder wherein the AuPd layer on the substrate was connected through a magnetic gold clamp from the top (see 6.16b). As the AuPd electrode of the printed MIM structure was attached to the conductive metal layer on the substrate, the bottom of the transfer-printed diode was directly connected to the gold clamp. The top of the diode, consisting of the Al and the AuPd delimitation layers, was electrically connected via the C-AFM tip. The conductive tip and the gold clamp on the

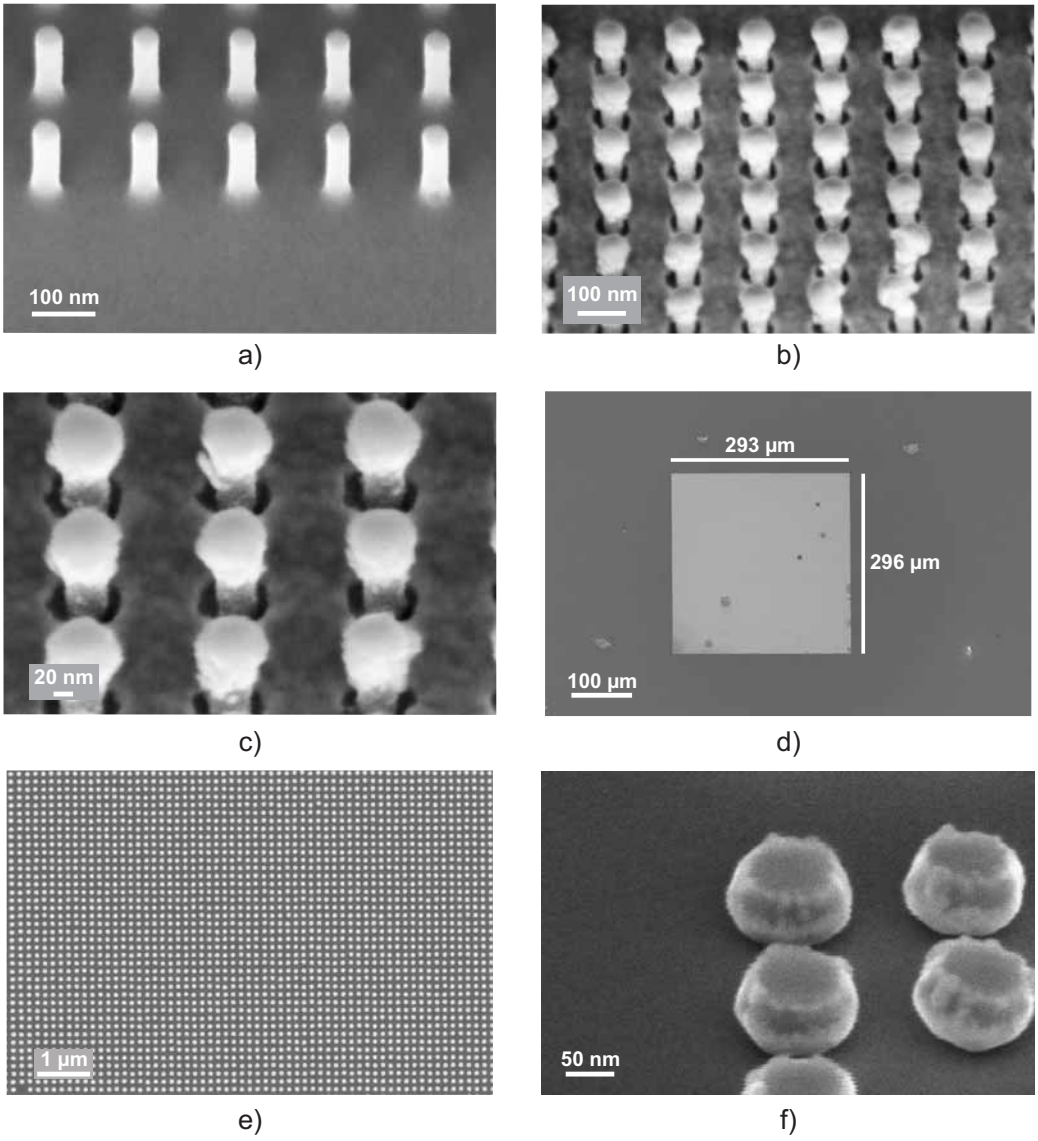

Figure 6.15: a) A scanning electron microscope (SEM) image of an edge of the Si stamp is shown at a tilt angel of 45°. The pillars feature a height of 80 nm and a diameter of 50 nm. b) Metal layers and an insulator are fabricated on the stamp that is covered with a hydrophobic self-assembled monolayer. c) No material was deposited on the sidewalls of the pillars as we used collimator plates during the evaporation. d) After covering the stamp with metals and the insulator, almost the whole array of MIM nanodiodes was transfer-printed on a target substrate. e) A zoom of the printed area covered with nanodiodes is presented here. f) 3 dimensional individual diodes can be seen by tilting the electron beam by 54°. The surface of the printed nanodiodes is very smooth allowing contacting the top with a conductive atomic force microscope. Reprinted with permission from [7]. Copyright 2012 American Chemical Society.

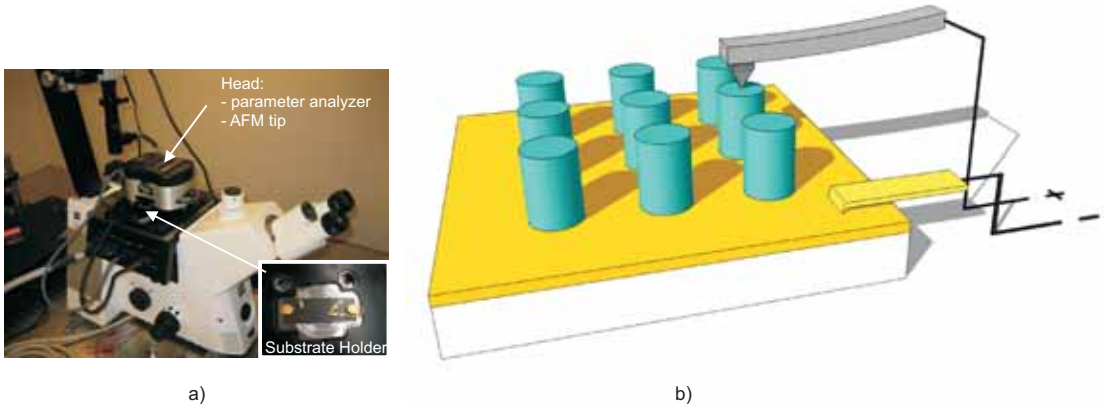

Figure 6.16: a) A photograph of the conductive atomic force microscope (AFM) setup: The parameter analyzer and the AFM tip are implemented in the head, and the substrate holder comprises ceramic plate and gold clamps for connecting the sample substrate. b) A schematic view of the AFM setup: The MIM pillars (turquoise) that are transfer-printed on a Si wafer (white) comprising a conductive AuPd layer (orange) are contacted from the top via a conductive AFM tip (here: positive voltage). The AuPd-layer on the substrate is connected via a gold clamp (here: negative voltage). Reprinted with permission from [7]. Copyright 2012 American Chemical Society.

substrate were connected to a parameter analyzer which was located in the head of the C-AFM setup (see 6.16a). This circuit was used for the electrical characterization of single MIM nanodiodes. The voltage was applied on the C-AFM tip and the current was measured at the same time.

As the area of the MIM diode is in the nanometer range, currents from 10^{-19} A up to 10^{-6} A are expected. Although the C-AFM setup was in a temperature, humidity and vibration controlled environment, electrical noise still occurred and the lowest measurable currents were in the 100 pA-range which is similar to C-AFM measurements reported in literature [132, 133]. We investigated several nanodiodes and only one of them showed a short circuit behavior. In all other diodes, an exponential I-V characteristic was measured (see Figure 6.17a). An asymmetric tunneling current behavior with respect to the applied bias was observed as expected due to the asymmetric diode structure with different metal electrodes. When comparing the measured current density of the nanoscale tunneling diodes with previously transfer-printed diodes featuring an area in the micrometer range discussed in section 6.3 [65], the current densities are in excellent agreement to each other, which in turn proves the

quality of the materials and fabrication process. The electrical stability under an applied voltage was improved by a factor of at least two by reducing the area of the tunneling diodes. The previously presented tunneling diodes showed a breakdown behavior around 5 V to 6 V. In contrast, the nanoscale diodes worked at least up to 10 V. We believe that the improved break down behavior is related to the reduced number of defects found in the insulating layers as the diode area is scaled down. This is another indication of the high quality of the ultra-thin AlO_x layer fabricated by the plasma treatment.

In order to extract static device parameters and to determine whether or not tunneling is the dominant transport mechanism, numerical simulations were carried out [134]. Hole currents can be neglected since the tunnel barrier for holes is much higher than for electrons. By assuming that direct/ Fowler-Nordheim tunneling is the dominant tunneling process, the current density can be modeled by the Tsu-Esaki formula [123].

An excellent fit of the simulation for voltages up to 6 V was accomplished when considering an energy dependent effective tunneling mass and using tunnel barrier heights of 4.2 eV for the AuPd electrode and 2.8 eV for the Al electrode. The value of 4.2 eV at the AuPd-AlO_x interface corresponds to the barrier height of Au in the Schottky limit. As the barrier height at the Al-AlO_x interface is known to be dependent on the growth mechanism, a smaller barrier height of 2.8 eV than the expected value of 3.1 eV can be explained by the formation of a dipole layer produced by charge transfer between the Al electrode and interfacial gap states in the AlO_x which is known to reduce the oxide barrier height [124, 125]. For higher voltages, the simulation predicts higher values for the current density. However scattering processes like electron-phonon interactions are not included in the simulation which are expected to reduce the tunneling current[135].

The cut-off frequency (f_{cut}) is the maximum frequency at which an electrical device still works properly [136] and has been introduced in section 6.3. The increase of the thickness of the dielectric leads to an increase of the cut-off frequency. However, the tunneling current is exponentially dependent on the tunnel barrier thickness. Thus, a dramatic current decrease can be expected when increasing the thickness of the dielectric. In general, a direct measurement of the permittivity of MIM nanodiodes is not possible with a C-AFM setup. However, we have previously determined the permittivity of the MIM diodes comprising a microscale area in a low noise probe station and the diodes showed a capacitance density of $\frac{C}{A} = 1.19 \cdot 10^{-6} \frac{F}{cm^2}$ [65]. We showed there that the dielectric constant is strongly dependent on the insulator thickness; although it is independent of the area A. The resistance R of the AuPd substrate that took

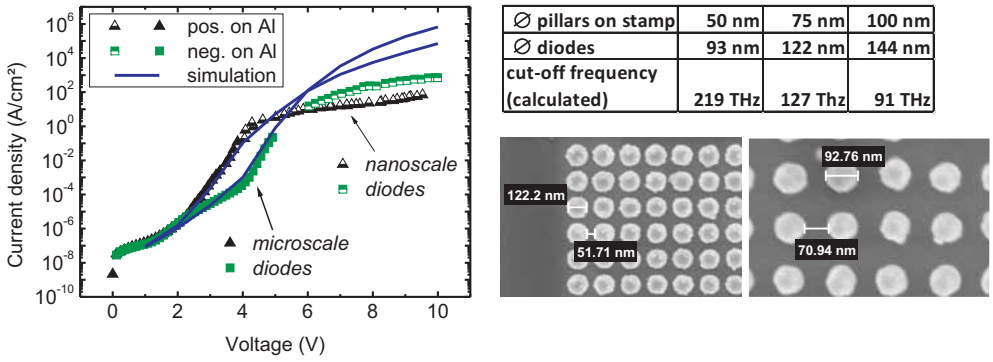

∅ pillars on stamp	50 nm	75 nm	100 nm
∅ diodes	93 nm	122 nm	144 nm
cut-off frequency (calculated)	219 THz	127 Thz	91 THz

Figure 6.17: a) The I-V-characteristic of a transfer-printed nanoscale MIM pillar (half-open symbols), measured using a conductive AFM setup, is presented in comparison with previously fabricated microscale MIM diodes (full symbols), characterized with a probe station, and numerical simulations (line). For a better comparison the positive and the negative polarity (on aluminum) are both shown on the positive V-axis and absolute logarithmic scale is used for the current density for the same reason. The nanoscale and microscale MIM structures show an excellent agreement and the simulation could extract static device parameters. b) The calculated cut-off frequencies of three different transfer-printed MIM diodes comprising areas between 93 nm and 144 nm are shown in the table and two SEM images show the spatial dimensions of MIM diode arrays. Reprinted with permission from [7]. Copyright 2012 American Chemical Society.

over the lead lines was determined to be 8.93 Ω. The area of the MIM tunneling diodes was measured via SEM and the diameter of the smallest printed pillars was determined to be 93 nm. A cut-frequency of 219 THz for the smallest MIM diodes can therefore be estimated. A further increase of the cut-off frequency is possible by reducing the diode area, however, because of the vertical thickness of the MIM nanodiodes, scaling down below 50 nm appears to be challenging so far. A better way to improve the performance of the device is the use of a low-k material, e.g. with a permittivity below the value of 4.8 that we determined for the 3.6 nm thin AlO_x.

We showed in this section a sophisticated large-area nanoscale device fabrication method for the transfer-printing of metal-oxide-metal tunneling nanodiodes which feature asymmetric I-V characteristics. We showed that the efficient fabrication of several million tunneling nanodiodes within one process step is possible. An implementation to CMOS technology can realistically be considered as the transfer-printing process is applicable for almost every substrate and the temperature required is rather low. We can tailor the cut-off frequency by varying the diode area, as the general conducting mechanism and the static device parameters are independent of the diode area. The AlO_x insulator has a thickness of 3.6 nm and retains its high quality during the printing process, so that even voltages up to 10 volts can be applied without destroying the quantum device. The electrical performance of the nanoscale devices is in good agreement with previously fabricated microdiodes. Numerical simulation shows that direct Fowler-Nordheim tunneling is the main conducting mechanism for the electrons, and static device parameters were extracted. Since the cut-off frequency of the smallest diodes is estimated as 219 THz, MIM nanodiodes are promising for extremely high-speed electronic and optoelectronic applications. Moreover, the fabrication of these nanoscale devices in dense arrays over large areas provides the possibility to fabricate THz rectifiers or also other devices in an economic and fast way.

In the next section, we focuse on the investiagtion of microscale and nanoscale MIM tunneling diodes featuring a TiO_x dielectric. As we will see, this oxide feature advantages with respect to its electronic and capacitive properties.

6.5 MIM microscale and nanoscale diodes featuring a TiO_x dielectric

In our previous section, aluminum oxide (AlO_x) was employed as the tunneling dielectric. However, AlO_x has a large bandgap. In order to generate a larger

electrical signal from the diode (i.e., larger tunneling currents through the insulator), a smaller bandgap dielectric is required. In this way, the tunnel barrier height is reduced and the probability for electrons to tunnel through the barrier is higher. A promising candidate is TiO_x. One drawback of TiO_x for this application is that the permittivity of TiO_x is reported to be relatively large [137], which would in turn lead to a large capacitance and hence to a small cut-off frequency of the MIM diodes [7]. We have shown before that the permittivity of thin AlO_x dielectrics decreases with decreasing dielectric thickness. Assuming this effect occurs in TiO_x as well, very thin TiO_x films are potentially useful for MIM tunneling diodes with large current signal (due to the small bandgap) and high cut-off frequency (due to the small permittivity).

TiO_x layers with thicknesses of less than 10 nm can be fabricated by a variety of techniques, such as (plasma-enhanced) chemical vapor deposition [138], sputtering [139], and atomic layer deposition [140]. It is however challenging to produce large areas films of pure titanium oxide with good homogeneity when the film thickness is in the range of a few nanometers. We present here a novel fabrication method for titanium oxide resulting in an ultra-thin dielectric with a thickness of about 2 nm over large areas. The thickness of the oxide was determined by ellipsometry. For electrical measurements, two metal electrodes with dissimilar work functions (Ti and Au) were prepared. Electrical measurements on microscale diodes and of ensembles of nanoscale diodes were carried out. Direct tunneling was observed, and static parameters were determined by fitting a numerical model to the experimental data. The permittivity of these ultra-thin oxide films determined from capacitance measurements indicates that the permittivity indeed strongly depends on the thickness of the insulator.

Three different types of samples have been fabricated in order to investigate the TiO_x. An array of micrometer MIM diodes have been fabrication by thermal evaporation through a shadow mask. An array of nanoscale crossbar structures were fabricated in a two-step nanotransfer printing (nTP) process. And a layer of TiO_x have been fabricated on a plane Si wafer for ellipsometry.

In order to fabricate microscale MIM diodes, a first metal electrode (Ti) was deposited through a shadow mask featuring line-like openings onto a silicon wafer covered by a 100-nm-thick layer of thermally grown silicon dioxide. To produce the ultra-thin TiO_x dielectric, the surface of the Ti layer was oxidized in an Oxford Plasma Technology Reactive Ion Etch (RIE) system operated at an oxygen partial pressure of 10 mTorr and a plasma power of 200 W for 30 s. These parameters are similar to those previously used for the fabrication of thin aluminum oxide layers [112, 141]. The second metal electrode (Au) was deposited perpendicular to the first electrode by thermal evaporation through a second shadow mask featuring line-like openings as well. In this way, an array of

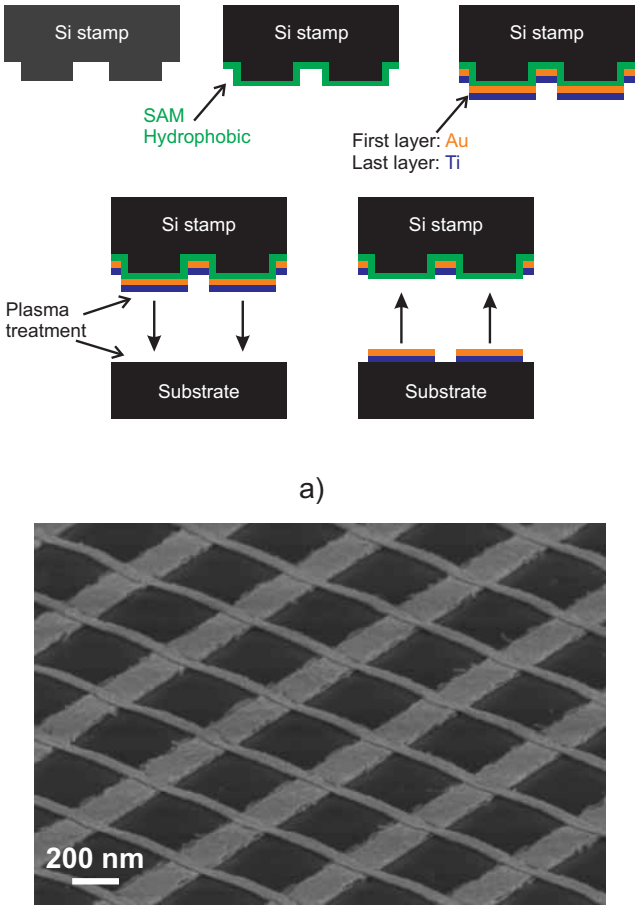

Figure 6.18: a) Dense arrays of nanoscale Au-TiO_x-Ti tunneling diodes fabricated by nanotransfer printing (nTP). A silicon wafer with raised, narrow lines is used as a stamp. In order to reduce the surface energy, the stamp is covered with a hydrophobic alkylsilane SAM. A stack of two metals, Au and Ti, is then deposited onto the stamp by thermal evaporation. The Au layer later serves as the bottom electrode of the MIM diodes, while the Ti layer is intended to promote adhesion of the metal stack on the target substrate during stamping. The surfaces of the stamp and of the target substrate (glass) are activated by oxygen-plasma treatments and then brought into physical contact, causing the Au-Ti metal stack to be transferred from the raised regions of the stamp onto the target substrate. b) Scanning electron microscopy (SEM) image of a crossbar array fabricated in a two-step nTP process. After transferring the Au bottom electrodes from the stamp onto the target substrate, the substrate is activated again and the Ti top electrodes covered with the oxygen-plasma-grown TiO_x dielectric are transferred from another stamp in a perpendicular orientation. The width of the Au bottom electrodes is 100 nm, that of the Ti top electrodes is 50 nm. Reprinted with permission [11]. Copyright 2012 American Institute of Physics.

Ti-TiO_x-Au crossbar structures was fabricated that allows each individual diode to be contacted with probe needles outside of the active area without damaging the dielectric.

The nanoscale MIM diodes were fabricated by nanotransfer printing (nTP) [9]. As for the Al/AlOx/Au diodes, first, a silicon stamp was prepared by etching trenches into the surface of a silicon wafer using a combination of electron-beam lithography and dry etching to produce raised, 100-nm-wide lines. The silicon was then covered with an alkylsilane self-assembled monolayer (SAM) in order to render the stamp surface hydrophobic (Fig. 6.18a). A 25-nm-thick Au followed by 4-nm-thick Ti was deposited onto the SAM-covered silicon stamp by thermal evaporation. Since Au is a noble metal and since the stamp surface is hydrophobic, the adhesion of the metal stack on the stamp surface is sufficiently weak to facilitate delamination of the metal stack during stamping. The 25-nm-thick Au layer later serves as the bottom electrode of the nanoscale MIM diodes. The 4-nm-thick Ti layer serves as an adhesion promoter to facilitate the transfer of the metal stack from the stamp onto the target substrate during stamping. To further improve the adhesion of the metal stack on the target surface, the Ti was activated by a brief oxygen-plasma treatment that increases the density of hydrophilic hydroxyl groups. The density of siloxane groups on the surface of the target substrate (glass) was increased in the same manner. After these two activation steps, the stamp was brought into physical contact with the target substrate, and a pressure of 50 bars and a temperature of 200°C were applied for 3 min. This causes the metals to be transferred from the raised regions of the stamp onto the glass substrate. Onto a second silicon stamp that was prepared similar to the first one (i.e., by covering the surface with raised, 50 nm-wide lines and rendering it hydrophobic with a SAM), 25-nm-thick Au followed by 25-nm-thick Ti were deposited by thermal evaporation. The 25-nm-thick Ti layer later serves as the top electrode of the nanoscale MIM diodes. The ultra-thin TiOx dielectric was then produced by oxidizing the Ti surface in the same way as described above for the microscale MIM diodes. Finally, the Au-Ti-TiO_x stack was transfer-printed onto the target substrate in an orientation perpendicular with respect to the previously patterned Ti-Au lines, resulting in a dense array of Ti-Au-TiO_x-Ti-Au crossbar structures (Fig. 6.18b). To allow electrical characterization of the nanoscale MIM diodes, contact pads were fabricated by photolithography, metal deposition and lift-off.

For ellipsometry measurements, a 30-nm-thick layer of Ti was deposited by thermal evaporation onto a silicon wafer covered with thermally grown silicon dioxide. The Ti surface was then oxidized by oxygen plasma as described above, and ellipsometry was performed to determine the oxide thickness.

The thickness of the plasma-grown TiO_x was determined by ellipsometry.

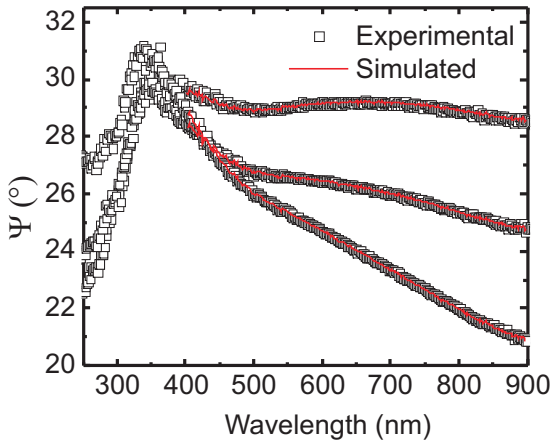

Figure 6.19: Measured (black squares) and simulated (red lines) ellipsometric spectra of ultra-thin (2.0 nm) plasma-grown titanium oxide films at three different angles of incidence (65°, 70°, 75°). By fitting the measurement data to the Cauchy model, the oxide thickness was calculated. Reprinted with permission [11]. Copyright 2012 American Institute of Physics.

The angle of incidence was varied between 65° and 75° with respect to the surface normal, and several measurements were performed. By fitting the experimental data to the Cauchy relationship [142], an oxide thickness of $2.0\text{nm} \pm 0.02\text{nm}$ was calculated (see Fig. 6.19). Since a loss feature around 300 nm occurs [143], we fit the experimental data between 400 nm and 900 nm in which the Caichy model is valid [144]. The mean square error in this fit is 1.087 and the refractive index determined from the fit is 2.04 at 550 nm.

The permittivity of these ultra-thin TiOx films was determined by measuring the capacitance of several microscale Ti-TiO_x-Au diodes. The Ti bottom electrode was set to ground potential and a DC potential modulated with a small AC bias was applied to the Au top electrode. An average capacitance per unit area of $2.25 \cdot 10^{-6}\text{F/cm}^2$ was calculated. This corresponds to a permittivity of 5.1 when assuming an oxide thickness of 2.0 nm (as determined by ellipsometry). This is to our knowledge the smallest permittivity that has been reported for titanium oxide (Tab. 6.1).

The current voltage characteristics of individual shadow-mask-patterned microscale Ti-TiO_x-Au diodes were measured in ambient air via a semiconductor parameter analyzer at room temperature by contacting the metal electrodes outside of the active area using probe needles. In these measurements, the Ti bottom electrode was set to ground potential, and a positive or negative potential was applied to the Au top electrode. The current through the diodes

method	thickness (nm)	permittivity
CVD [145]	7-91	7-55
PECVD [138]	20-200	60
Sputtered [139]	10	95
Sputtered [146]	300-500	50-70
ALD [73]	9-25	60-80
ALD [147]	35-140	60-100
Plasma (this work)	2.2	5.1

Table 6.1: Permittivity of titanium oxide reported in the literature and determined in this work. Reprinted with permission [11]. Copyright 2012 American Institute of Physics.

was measured as a function of the applied voltage. The results are shown in Figure 6.20. The circles represent the experimental data obtained from the Ti-TiO_x-Au diodes. In the graph, the absolute value of the current density is plotted as a function of the applied voltage, so that the asymmetry of the current voltage curves can be easily evaluated. For comparison, the measured current voltage characteristics of one of the Al-AlO_x-Au tunneling diode described in section 6.3 [65] are also shown (squares).

As can be seen in Figure 6.20a, the current-voltage characteristics of the MIM diodes are asymmetric around zero bias. For example, at an applied voltage of -0.5 V, the absolute value of the current density is two orders of magnitude larger than the current density at +0.5 V. More importantly, the observed degree of asymmetry is much larger in the Ti-TiO_x-Au diodes than in the Al-AlO_x-Au diodes. In order to identify the mechanism of charge transport through the ultra-thin titanium oxide films, numerical simulations [134] were carried out. The work functions of Ti and Au were assumed to be 3.95 eV and 5.2 eV [148], respectively, and the thickness of the TiO_x was assumed to be to 2.0 nm (as indicated by the ellipsometry measurements). The effective mass of the electrons tunneling through the dielectric and the height of the potential barrier at the Ti/ TiO_x interface were adjusted until a satisfactory fit to the experimental data was obtained. We determined an effective electron mass in TiO_x of $m_o x = 2.62 \cdot m_e$ and a barrier height at the Ti/ TiO_x interface of 0.71 eV, in good agreement with literature [149, 150]. In Figure 6.20a, this numerical fit is shown with blue lines. We believe that the observed discrepancy between the experimental data and the numerical fit for negative voltages is due to the presence of interfacial traps that reduce the effective potential barrier height until the traps are depleted [151]. For the most part, the numerical model provides a satisfactory fit of the experimental data, showing that direct tunneling is the main conduction mechanism.

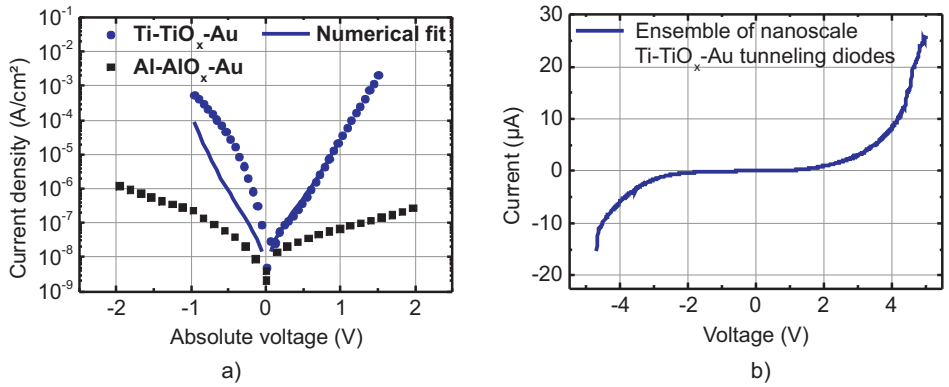

Figure 6.20: a) Measured (blue circles) and simulated (blue lines) current-voltage characteristics of a shadow-mask-patterned microscale Ti-TiO_x-Au tunneling diode. For comparison, the measured current-voltage characteristics of an Al-AlO_x-Au tunneling diode (black squares) are also shown. Compared with the AlO_x based diodes, the TiO_x based diodes are characterized by a smaller dielectric thickness (2.0 nm instead of 3.6 nm) and a smaller potential barrier height at the metal-insulator interface, which explains that the current density in the TiO_x based diodes is several orders of magnitude larger than in the AlO_x based diodes. With numerical simulations, static parameters of the oxide were extracted. b) Measured current-voltage-characteristics of an ensemble of transfer-printed nanoscale Au-TiO_x-Ti tunneling diodes, showed an exponential relationship between the current and the applied voltage. Reprinted with permission [11]. Copyright 2012 American Institute of Physics.

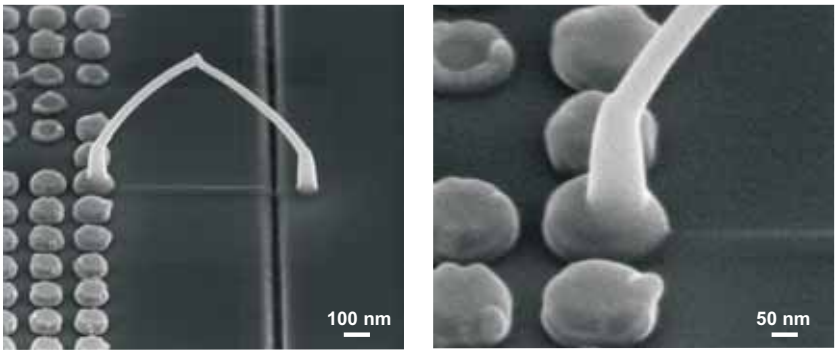

Figure 6.21: a) A nanoscale MIM diode is connected to a conductive microscale pad vie a Pt bridge grown in a FIB system. b) A zoom of the connection of the Pt bridge and the MIM nanodiode.

In addition to individual shadow-mask-patterned microscale Ti-TiO_x-Au tunneling diodes, we also measured the current-voltage characteristics of an ensemble of transfer-printed nanoscale Au-TiO_x-Ti tunneling diodes. All diodes within this ensemble are connected in parallel (see Figure 6.20b)). The exact number of functional diodes within the ensemble is unknown, since some fraction of the diodes are believed to be short-circuited (which also produces a finite shunt resistance). The measured current-voltage characteristics of the ensemble are shown in Figure 6.20b). As can be seen, the dependence of the measured current on the applied voltage is exponential as well as asymmetric with respect to the zero bias.

Here, we showed on a new fabrication method to produce ultra-thin titanium oxide films by an oxygen plasma. The materials characteristics, such as the thickness and the permittivity of the TiO_x films, were determined by ellipsometry and by capacitance measurements. Since electric fields up to 22 MV/cm can be applied without damaging the dielectric, this method is suitable for the fabrication of high-quality insulating films. The current density through these ultra-thin titanium oxide films is 4 orders of magnitude larger than the current density previously measured in thin films of plasma-grown AlO_x. The permittivity of the ultra-thin titanium oxide films was found to be much smaller than the permittivity of thicker titanium oxide films, which means that ultra-thin TiO_x is an excellent candidate for rectifying metal-insulator-metal tunneling diodes in terahertz applications, such as infrared detectors.

6.6 Pt bridges from MIM diodes to contact pads

We showed that nanoscale MIM diodes can be characterized electrical using a C-AFM setup. However, this setup is very fragile with respect to vibrations. Therefore, another technique was used in order to connect nanoscale Au-AlO_x-Al diodes to a contact pad using a CVD system in a FIB.

In a first step, an individual contact pad is cut with the FIB which represents an conductive island on the substrate which is not connected to the rest of the substrate. After that, Pt is deposited on top of the MIM diode and in the pad in such a way, that they connect at a certain height. In this way, the top electrode of a MIM junction is connected to the island (Figure 6.21).

We were not able to obtain electrical data on this structures, since the bridges are very fragile, and can be destroyed easily. However, when improving the process, this kind of connections might be used for investigations of small nanodevices.

6.7 Conclusions

In summary, we fabricated large-arrays of microscale and nanoscale MIM tunneling diodes in a transfer process. We found that the dielectric properties can be scaled down from microscale to nanoscale structures. Further, with respect to AlO_x and TiO_x, an important finding is the dependence of the permittivity on the thickness of the dielectric: In the nanoscale the permittivity decreases with decreasing thickness. This fact is important to be considered in *high-k*-applications. Further we could prove for both material systems, namely Au(Pd)-AlO_x-Al and Au-TiO_x-Ti, that direct tunneling and Fowler-Nordheim tunneling are the dominant conduction mechanisms. An asymmetric I-V-characteristics has been observed around zero volt for both junctions.

Since plasma grown TiO_x is thinner by almost a factor of 2 than AlO_x and feature in this thin-layer configuration a similar permittivity, the current flowing through the MIM junction is higher. This is an important fact which we will see in the next chapter. Furthermore, the asymmetry around zero volt is also larger for TiO_x based diodes. Consequently, we decided to implement Au-TiO_x-Ti diodes in rectenna arrays.

Chapter 7

Nano antenna and rectenna arrays

Nowadays, several possibilities exist for detecting long wave infrared (LWIR) radiation. The most common detectors are bolometers [152] and low-bandgap detectors, such as InGaAs detectors. Another promising candidate that which has been proposed in 1968 by the group of *Javan*, but which is still not commercially available, is the "rectenna" device. The word "rectenna" is a neologism word and originates from the two words rectifier and antenna. In this chapter, we present the fabrication of dipole antenna arrays coupled to MIM junctions and to thermocouples. The antenna arrays were fabricated in a transfer printing process. We observed that in rectennas, in which antennas are coupled to MIM junctions, a thermal effect, namely the Seebeck-effect, is responsible for the obtained voltage. Since our rectennas are based on dipole structures, a theoretical background of dipole antennas is given in the next section.

7.1 Theoretical background of dipole antennas

A dipole antenna feature a bar-like structure which is usually divided into two parts wherein each part is contacted individually (Fig. 7.1). The dipole antenna can either emit or receive electromagnetic radiation. In order to match the wavelength of the incident radiation, the length of the dipole has to be approximately half of the wavelength of the incident wave. In this case, a voltage node is formed at the center of the antenna and anti nodes at each end of the antenna. The opposite case occurs with respect to the current.

However, since our antenna structures are not free-standing dipole antennas in vacuum, the effective wavelength detected by the antenna is changing depending

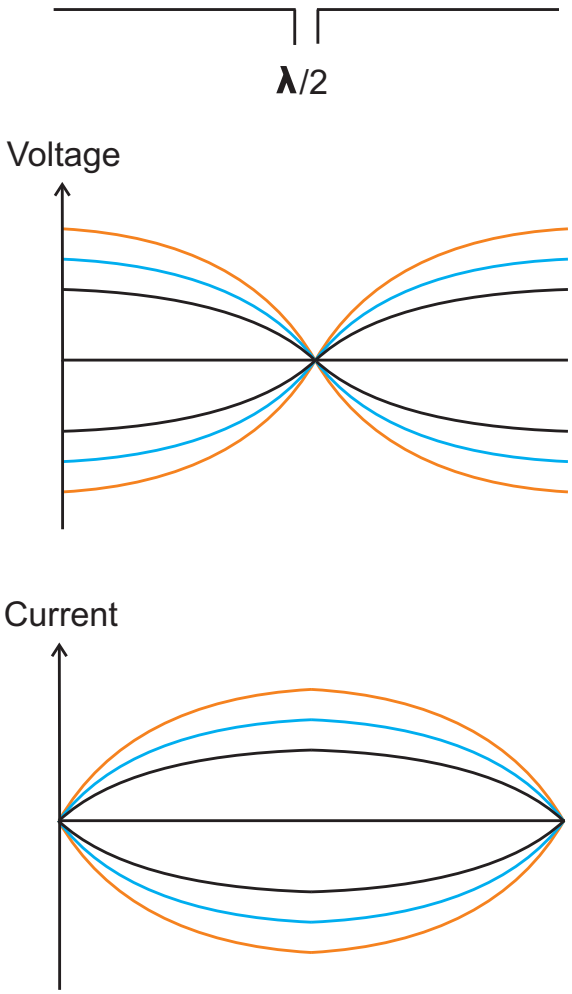

Figure 7.1: A dipole structure, the current distribution and the voltage distribution along the dipole are shown.

on the substrate on which the antenna is fabricated. Since the antenna is located at an interface between two materials (substrate and air), the effective dielectric constant can be calculated as follows [110]:

$$\epsilon_{eff} = \frac{\epsilon_{SiO_2} + \epsilon_{air}}{2} \tag{7.1}$$

and the effective wavelength is given by:

$$\lambda_{eff} = \frac{\lambda_{air}}{\sqrt{\epsilon_{eff}}} \tag{7.2}$$

Based on our setup, we designed the antennas sensitive to a CO_2 laser which features a wavelength of 10.6 µm. The dielectric constant in SiO_2 at these frequencies is 4.84 [153]. In order to match the wavelength of the laser, the dipole length has to be 3.1 µm.

Transverse currents perpendicular to the dipole orientation have also to be taken into account when the width is more than $\lambda/35$ [154]. Since the widths of our dipole antennas are in the range of 50 nm until 100 nm, these currents can be neglected.

7.2 IR sensitive antenna and rectenna arrays

Typical wavelengths in the LWIR regime are around 10 µm. The fabrication of an IR sensitive antenna, for example a dipole antenna or a bowtie antenna, can easily be done via optical lithography. However, once the electromagnetic waves are absorbed by the antenna, a high frequency current f_{AC} is induced in the antenna that corresponds to the wavelength of the incident light by the relation:

$$f_{AC} = \frac{c}{\lambda} = \frac{c}{10\ \mu m} = 30\ THz \tag{7.3}$$

wherein c is the velocity of light and λ the wavelength of the incident IR light. Since no conventional electronic devices are able to deal with such high frequencies, a rectifying device has to be coupled to the antennas in order to transform the high AC current into DC. An antenna featuring a rectifier is then called a "rectenna".

Conventional rectifiers, namely, pn-junctions or Schottky diodes, are not able to rectify terahertz (THz) frequencies, since their cut-off frequencies usually extend in the megahertz regime or at best in the gigahertz regime [155]. Recently, Schottky diodes with a cut-off frequency of a few terahertz have been reported [156], but only in the form of individual diodes that can hardly be integrated into antennas. Metal-insulator-metal (MIM) diodes that have been discussed

intensively in chapter 6, feature the ability for rectifying THz frequencies due to femtosecond tunneling time.

Currently, several groups are working on the theory and experiments to design the "ultimate" rectenna suitable for industrial applications with respect to energy harvesting and IR detection [64, 65, 157, 158]. A small overview of several groups working on the concept of rectennas is given in table 7.1.

group	year	reference
Javan	1968-1978	[58, 159]
Bailey	1972	[160]
Gustafson	1974	[161]
Smythe	1974	[162]
Brown	1976-1996	[163, 164]
Kneubühl	1977-1998	[165, 166]
Weiss	1983-1998	[59, 167]
Klingeberg	1983-1985	[167, 168]
Marks	1984	[169]
Kale	1985	[170]
Chang	1992-2005	[171, 172]
Korving	1996	[173]
Boreman	1999-2011	[66, 174]
Puzzer	2002	[175]
Berland	2001-2003	[176]
Tamm	2004	[177]
Libsch	2005-2007	[178, 179]
Buckle	2005-2008	[180, 181]
Pinhero	2008	[182]
Peckerar	2009-2010	[157, 183]
Osgood	2007-2010	[158, 184]
Moddel	2010-2011	[64, 185]
Porod	2005-2012	[7, 186]
Lugli	2011-2012	[7, 65]

Table 7.1: Publications of groups that worked and still works in the field of rectennas with MIM diodes.

In the following sections, we show concepts and the fabrication of rectenna arrays using our approach, namely nanotranfer printing (nTP).

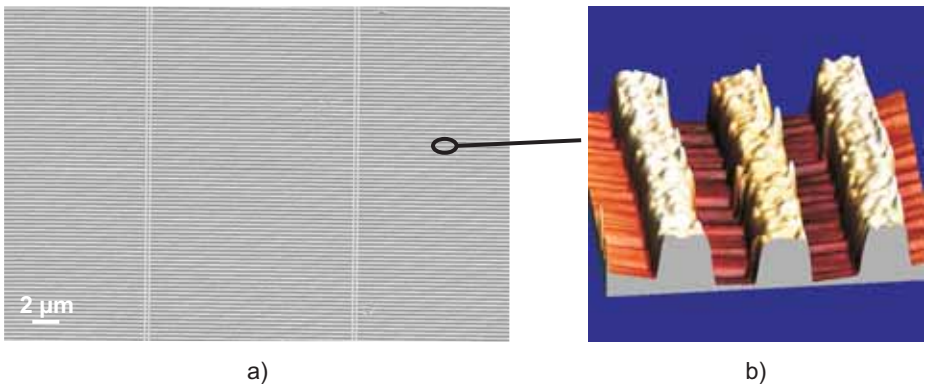

Figure 7.2: a) A scanning electron microscope image of transfer printed antenna structures featuring a line width of 100 nm. b) An atomic force microscope image prove the high quality of the transfer printed structures, since the side walls are straight and the height of all structures is equal. With permission from [13]. Copyright 2012 Springer.

7.3 Transfer printed antennas

So far, we showed that a large area fabrication of millions of the first key component in rectennas, namely the MIM tunneling diode, can be achieved with nTP. The second component is the IR antenna. We fabricated several antenna structures on Si wafers comprising a thermally grown SiO_2 oxide layer. The effective wavelength occurring at the antenna on this substrate is 3.1 µm [110].

We fabricated antenna structures having a width of 100 nm in a nTP process. The material composition of the fabricated antenna structures was 25 nm Au and 4 nm Ti (adhesion promoter). We were able to produce a dense array of several hundred thousand potential antennas (Fig 7.2). In order to characterize the transfer-printed antenna structures, we adjusted the length of the antenna structures to match the effective incident IR radiation using focused ion beam (FIB), and produced a thermocouple as a rectifying element thereon [187] featuring microscale contact pads for contacting to a probe station (Fig. 7.3a)).

For characterizing the antenna structures, we used a special setup comprising a CO_2 laser featuring a wavelength of 10.6 µm. The light of the laser beam was converted into linear polarized light and passed through a half-wave plate for changing its polarization, before reaching the sample. Via probe needles, the antenna array has been contacted for determining the antenna response with respect to the polarization of the incident laser beam. Fig. 7.3b) presents the antenna response wherein the upper symbols represent the polarization dependent measurement and the lower symbols are the noise when switching off the beam.

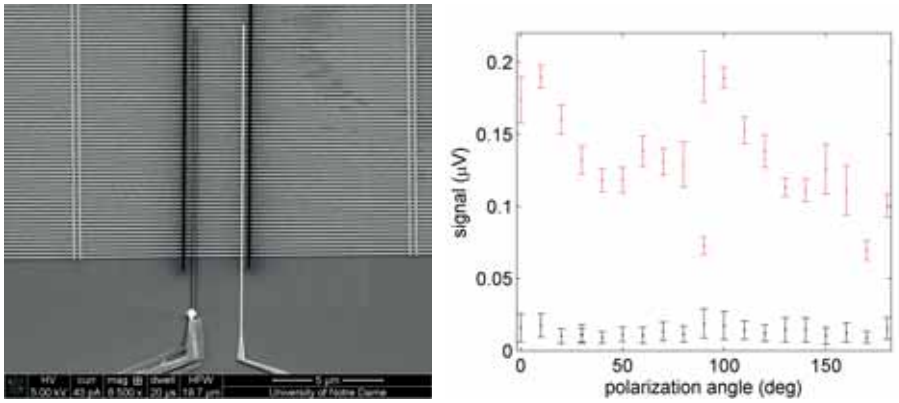

Figure 7.3: a) A scanning electron microscope image of transfer printed antenna structures featuring a thermocouple fabricated with electron beam lithography thereon. b) Antenna response of an array of transfer printed antenna structures featuring a thermocouple as a rectifier. The upper symbols represent the antenna response (signal) when illuminating with a laser beam, the lower symbols represent the noise level. With permission from [13]. Copyright 2012 Springer.

Indeed, an on-off ratio of a factor seven could be determined. However, a clear polarization dependence could not be obtained. Most likely, the antennas in the array are arranged in a too densely, so that the incident wave cannot resolve the individual antennas [188]. Therefore, we analyzed the interferences occurring within an antenna array and optimize the distances between the antennas which is presented in the next section.

7.4 Rectenna array

7.4.1 Simulation of spatial dimensions with the array

The high frequency structural simulator (HFSS) from the company Ansys Corporation was used to simulate the separation of the rectennas in the array. The incident radiation excites currents on the dipole antennas forming the array. These currents will re-radiate and interfere with the incident radiation at the neighboring antennas. The separation between the 3.1 µm long dipole antennas along the direction parallel and perpendicular to the axis of the dipole antennas was varied and the increase in response to an incident plane wave was simulated. The largest increase was found when separating the antennas by 5 µm in the direction parallel to the axis of the dipole antennas and by 5 µm along the direction perpendicular to the antenna axis (Fig. 7.4).

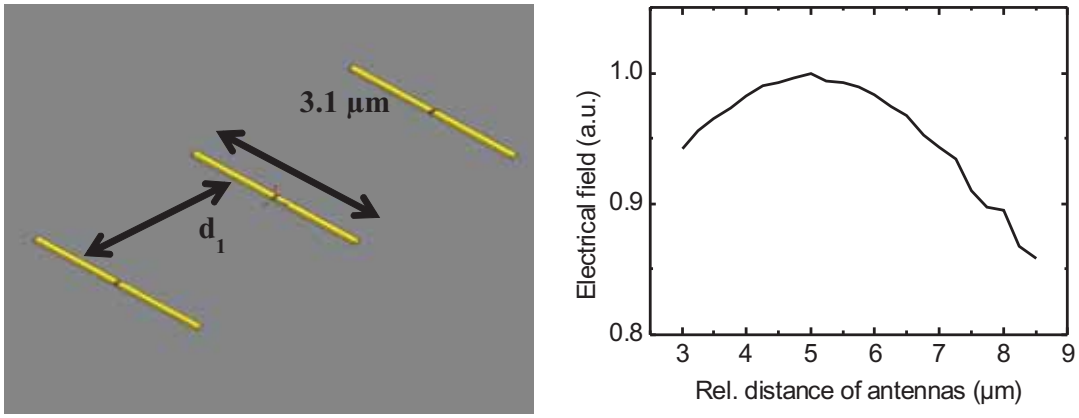

Figure 7.4: HFSS simulations in order to find optimum distance between the antennas along the direction perpendicular to the antenna axis. With permission from [62]. Copyright 2012 [62].

7.4.2 Concept of rectenna array fabrication and operation

In chapter 6, we determined the best materials of nanoscale MIM diodes and we could prove their outstanding performance. Further, a successful transfer of antennas arrays was accomplished, and we simulated the optimum spatial dimensions of the antennas including the best relative spacing with respect to each other. In this way, destructive interference within the array is avoided. Based in these results, we developed a concept for the large-area fabrication of rectennas.

We designed two stamps. The first stamp feature 100 nm-thick lines that are spaced by 11 µm from each other. We evaporated 25 nm of Au on the stamp and 4 nm of Ti (adhesion promoter). After activating the surface of the first stamp, the lines were transfer-printed onto a glass substrate. In Fig. 7.5a), the transfer of the lines of the first stamp is shown schematically. The contact pad to which all lines are connected is not integrated in the stamp and is fabricated afterwards by shadow evaporation. The second stamp consist of antenna structures that are connected to each other. The relative spacing between the antennas on the second stamp comply with the results from the HFSS simulations. We evaporated 25 nm of Au and 25 nm of Ti thereon. The Au layer on the second stamp represents both a delamination layer and low resistivity material in order to assist the current that flows in the Ti electrode. After that, the surface of the second stamp has been oxidized in a plasma in order to obtain the 2.0 nm-thin TiO_x tunnel dielectric. In a subsequential process, the glass substrates was

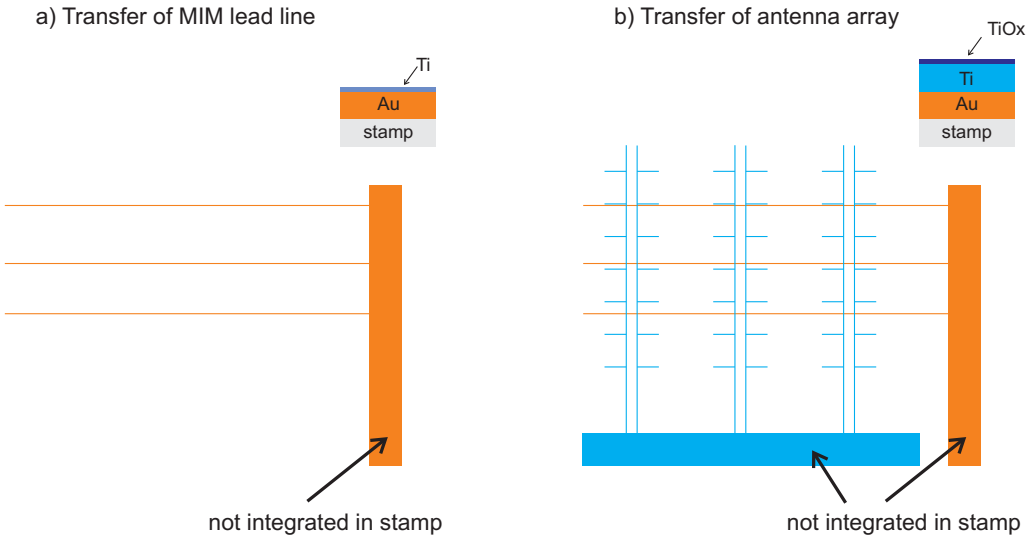

Figure 7.5: Concept of rectenna array fabricated via nanotransfer-printing. With permission from [62]. Copyright 2012 [62].

activated as well as the second stamp, and the second material stack was also transferred on the lines on the glass substrate which were transferred from the first stamp. This shown schematically in Fig. 7.5b). The second contact pad is also fabricated by shadow evaporation afterwards.

The resulting structure of that two-step transfer process can be seen in Fig. 7.6a). The overlap of the lines form the MIM diode through which the induced currents are rectified: Currents that are induced in the antennas that were fabricated in the second transfer process and reach the overlap of the lines that were fabricated in the first transfer process and the antenna structures. At the overlap, parts of the current are rectified since the MIM junction represents a diode (Fig. 7.6b)).

Scanning electron microscopic images show the first stamp with lines (Fig. 7.7a) and the second stamp with antenna structures (Fig. 7.7b). Fig. 7.7c show an array of successfully transferred rectennas. By zooming in the array, we investigated individual antennas and MIM diodes with respect to their morphology. A clear overlap of the lines fabricated in the two step nTP process is visible. After the fabrication of the array, we manufactured contact pads on top of the array by conventional optical lithography and lift-off techniques in order to address individual sectors featuring 25 thousand rectennas each (Fig. 7.7e)). Further, optoelectronic measurements were carried out.

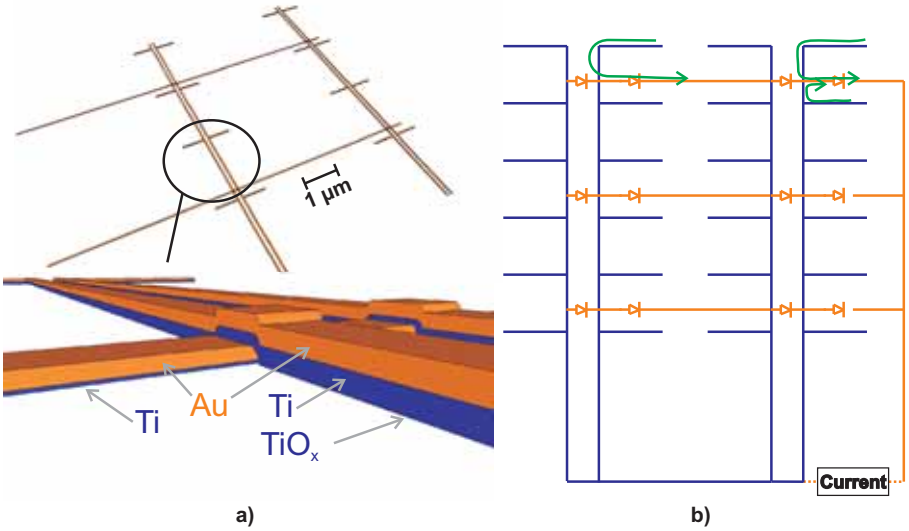

Figure 7.6: a) The design of the rectenna array is shown wherein the overlap of the initially transferred lines featuring Ti (adhesion promoter) and Au (first electrode) and the antenna structures featuring TiO_x (insulator), Ti (second electrode), and Au (second electrode and delamination layer) represent the MIM diode. b) The resulting circuit diagram shows the initially transferred lines (orange), the secondly transferred antenna structures (blue) and the rectified currents (green). With permission from [62]. Copyright 2012 [62].

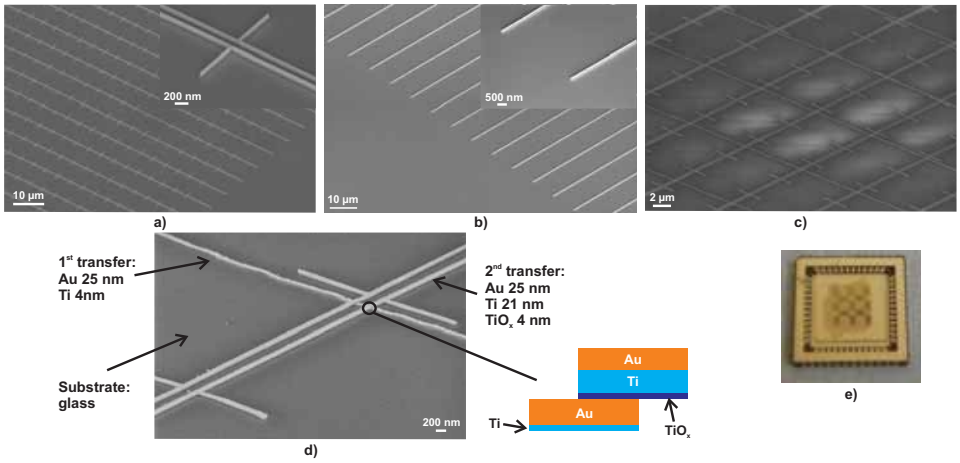

Figure 7.7: a) A scanning electron microscope (SEM) image of the first stamp b) and of the second stamp. c) A magnified view of the transferred rectenna array onto a glass substrate is shown here. d) In a further magnified view of the transferred array, the overlap of the initially transferred lines and the secondly transferred antenna structures which represents the MIM diode is shown. The final chip including the contact pads fabricated by optical lithography is shown in e). With permission from [62]. Copyright 2012 [62].

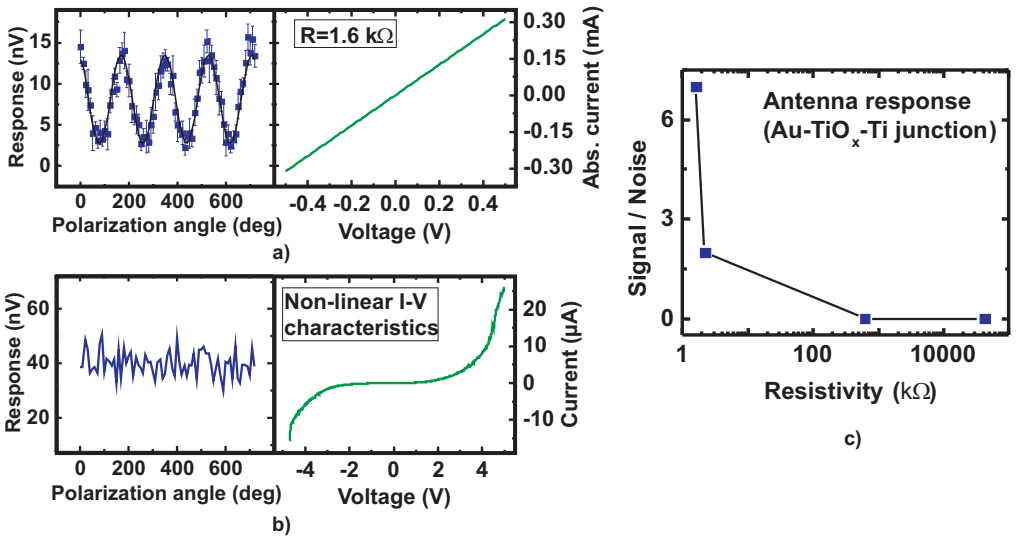

Figure 7.8: a) Polarization-dependent antenna response of a section of the rectenna array that shows linear I-V characteristics with a small resistance. b) In contrast, the antenna response of a section of the rectenna array that shows high-resistance and exponential current-voltage-characteristics is below the noise level. c) The highest signal to noise ratio is attained by a sector with lowest resistivity, which supports the model of a thermal rectification effect in the rectenna array. With permission from [62]. Copyright 2012 [62].

7.4.3 Optoelectronic characterization of rectenna array

In order to determine the rectenna response of several sectors of the antenna array, we connected one sector, as defined by the bonding pads (Fig. 7.7e)), at a time to a voltage amplifier and illuminated the entire array with a linear polarized CO_2 laser operating at 28 THz. A half-wave plate was used to adjust the orientation of the linear polarization of the incident radiation.

We observed a clear polarization dependent antenna response in several sectors: When the linear polarization of the incident electric field was perpendicular to the axis of the antennas, the antenna response was reduced to the noise level of the device. When the polarization of the IR wave was parallel to the dipole antenna, the measured response was seven times larger than the noise level (Figure 7.8a). An antenna array of this size has never been demonstrated before. In addition, optimizing the material combination and the design of the rectenna array, we were able to obtain the highest polarization ratio for unbiased rectennas in this wavelength regime, wherein the polarization ratio is defined as the ratio of the antenna responses to incident radiation with linear polarization parallel and perpendicular to the axis of the antenna.

However, other sectors investigated did not exhibit any radiation response. In order to understand this result, we investigated the I-V characteristics of the diode ensembles without illumination. In those sectors where no antenna response was observed, the expected tunnel-diode-like, non-linear I-V behavior was measured, and had a resistance in the range of MΩ. In contrast, we found that the sectors in which we observed a clear antenna response exhibited a linear I-V characteristic with a small resistance (1 kΩ), that is, the dielectric in several sectors exhibited linear resistive paths rather than tunnel-barrier behavior. In other words, the observed relationship between the I-V characteristics of the MIM junctions and the measured antenna response is exactly opposite to that expected by the original MIM diode theory. This suggests that the operation mechanism of the rectennas is not based on tunneling rectification in the MIM junctions, as was previously thought.

7.4.4 Seebeck effect vs. tunneling rectification

We believe that the Seebeck effect [189] is the dominant mechanism in our devices that do not exhibit a tunnel barrier, leading to the antenna response. Due to IR absorption, the array is heated up, whereas the electrodes furthest away from the array and closest to the contact pads are not heated. The temperature gradient in each of the electrodes creates a voltage drop, which is related to the Seebeck-coefficient of the electrode metals [187]. Further, the Seebeck-effect provides a consistent explanation for the observed relationship between the current-voltage behavior of the sectors of the antenna array and the measured antenna response (quantified by the signal-to-noise ratio) seen in Figure 7.8. Devices with a lower resistivity exhibit a larger signal-to-noise ratio (Figure 7.8c).

In order to verify our findings, our cooperation partners at the University of Notre Dame fabricated test structures of single rectennas consisting of various noble metals in direct contact with one another, i.e. without a tunnel barrier. Since noble metals do not form a native oxide, no insulating layer is present in these rectennas (Figure 7.9a). All antennas were characterized with respect to their optoelectronic (antenna response under illumination) and electronic (I-V characteristics) properties.

We compared the antenna response of several rectennas featuring the same dimensions but different metal combinations (Figure 7.9a) and found a linear dependence of the antenna response on the difference in the Seebeck-coefficients of the two electrodes (Figure 7.9b), in excellent agreement with theory:

$$V = (S_{M1} - S_{M2})\mathrm{x}(\mathrm{T_{hot}} - \mathrm{T_{cold}}) \tag{7.4}$$

where S_{M1} and S_{M2} are the Seebeck-coefficients of the metals, and T_{hot}

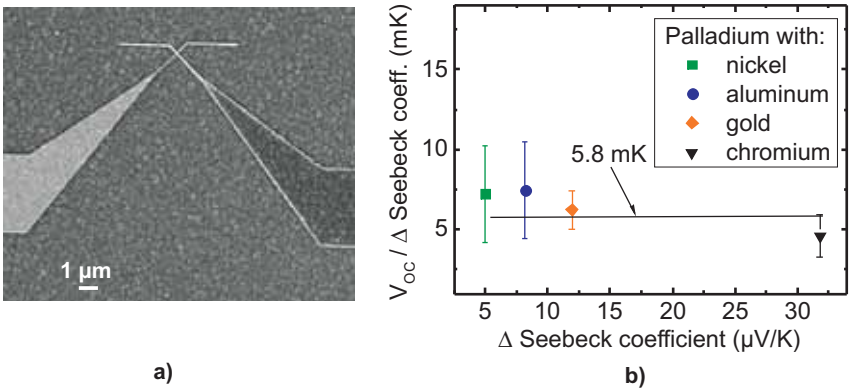

Figure 7.9: a) SEM image of single rectenna consisting of only noble metals without oxide layer. b) A constant ratio between the open circuit voltage (V_{OC}) and relative Seebeck coefficients is obtained, and is equal to the average temperature difference between the junctions. With permission from [62]. Copyright 2012 [62].

and T_{cold} are the temperatures of the metals at the hot and the cold junction. Since we did not incorporate thermometer structures into the antenna array, we infer from Figure 7.9b that the average temperature difference between the two junctions is the same for all of the tests and is approximately 5.8 mK. Invoking the rectification mechanism of rectennas with the Seebeck effect also explains why the response of the functioning rectenna sectors is small. Since the difference in the Seebeck-coefficients of Au and Ti is relatively small, the induced open-circuit voltage is consequently also smaller than for other possible material combinations with a larger difference of their Seebeck coefficients. Also, the array was not designed to maximize temperature differences across the MIM junctions. If rectennas are built based on the Seebeck effect without the need for a tunnel barrier, the fabrication process is drastically simplified, since the manufacture and implementation of the ultra-thin oxide layers represented one of the key challenges for these devices.

Believing that the tunneling mechanism is the dominant rectifying mechanism, several groups proposed to bias the rectenna in order to increase the asymmetry of the tunneling currents around the bias voltage, and thus, to increase the rectified [166, 178], according to the dependence of rectified current on the nonlinearity of the I-V operating point:

$$I_{DC} = \frac{1}{4}\frac{d^2I}{dV^2}\Big|_{V=V_{bias}} V_0^2 \tag{7.5}$$

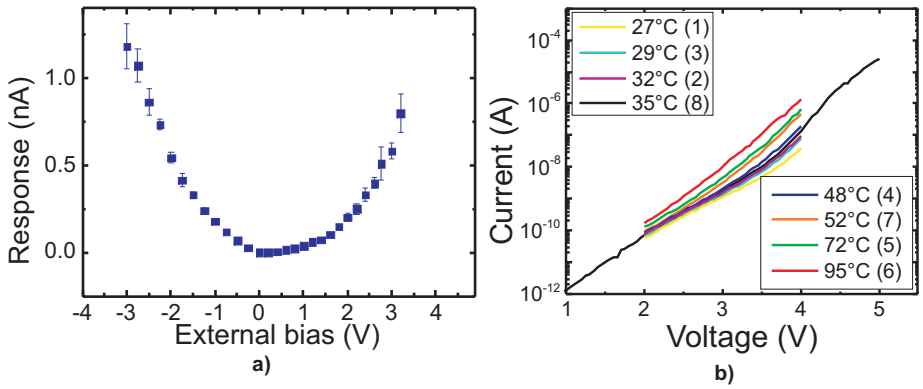

Figure 7.10: a) When externally biasing a sector of the rectenna array that showed no antenna response without an applied bias, a current signal as antenna response is observed. b) Temperature dependent I-V-characteristics of a MIM diode proves that the resistivity of the tunnel current is decreasing for higher temperatures and thus a bolometer effect is achieved. With permission from [62]. Copyright 2012 [62].

where V_0 is the amplitude of the induced voltage and V_{bias} is the applied voltage.

We also followed this principle and biased ensembles of antennas showing nonlinear I-V characteristics and a lack of response to incident IR radiation at zero bias. When applying an external bias, we obtained an antenna response (Figure 7.10a). However, further investigations showed that the response obtained under external bias can also be explained by a standard bolometric effect [57] due to the temperature dependence of the tunnel current. When radiation is incident on the biased rectennas, a resistance change at the MIM junction occurs due to heating. This explanation is supported by our temperature dependent I-V measurements of our MIM junctions (Figure 7.10b). Therefore, the present concept of diode rectification for biased rectennas should be further investigated in light of the contribution due to temperature dependent tunneling.

7.5 Conclusions

In summary, we showed the fabrication and investigation of the antenna arrays with nanotransfer printing. We showed the rectification mechanism in IV sensitive rectennas. Our investigations show that thermal heating of the absorbed incident IR radiation and a consequent temperature gradient in two different metals is the responsible rectification mechanism rather than the unbiased MIM tunneling diode. We further showed a highly efficient fabrication method for the

fabrication of nanoscale solar rectenna arrays of nearly one million elements. Our findings offer a wide range of new possibilities for the design of infrared rectenna detectors and solar rectenna arrays for energy harvesting. We suggest that the response to incident radiation of biased antenna coupled MIM diodes could also be attributed to a thermal effect. However, the main rectification process has not yet been determined and further investigation is required.

Chapter 8

Conclusion and Outlook

8.1 Conclusion

We presented in this work a new industrial orientated fabrication method based on protocols in literature, in order to manufacture microscale and nanoscale devices over large areas in a high quantity and quality, namely a nanotransfer printing process. Material research has been done for finding the optimum material combinations that are suitable for transfer printing. We found that noble metals provide a weak adhesion to almost any surfaces and consequently these metals are excellent candidates for delamination layers that are in contact to the stamp prior transferring. The stamp itself is covered with a hydrophobic SAM for further providing weak adhesion to the metals to be transferred. In order to improve the adhesion between the materials to be transferred and the target surface, namely Si, SiO_2 or glass, the adhesion promoter that is deposited on the materials to be transferred is represented by Ti or Cr. A hydrophilic surface on the adhesion promoter and the target substrate is formed by various dry and wet chemical treatments. During our research, we found that the temperature which is applied during transferring is crucial process parameter. The transfer yield is strongly promoted when applying temperatures in the range between 150°C and 200°C. The reason for this is that we used solid adhesion promoters and target substrates. water is formed, when activated Ti and Si surfaces comprising hydroxyl groups come into physical contact with each other and build a covalent binding. The water is removed by applying high temperatures which results in a higher transfer yield, since this process is reversible. The development of a highly efficient transfer process gave us the possibility to transfer millions of devices in a fast and dry process.

Various material fabrication processes have been carried out for producing efficient MIM diodes. The key material fabrication method with respect to MIM diodes is represented by the oxygen plasma treatment in a RIE for growing a

nanometer-thin dielectric. We were able to grow high quality AlO_x (3.6 nm thick) and TiO_x (2.0 nm thick) on Al and Ti surfaces, respectively. We could show that these dielectrics are suitable tunnel barriers for microscale and nanoscale MIM diodes using sophisticated characterization methods like ellipsometry or conductive-AFM. We showed that a asymmetric tunnel current around zero bias is observed in our microscale and nanoscale MIM junctions which are in line with each. Numerical and kinetic Monte Carlo simulations proved that direct tunneling and Fowler-Nordheim tunneling are the main conduction mechanism and static device parameters were extracted with these simulations. We further observed that the static permittivity of thin dielectrics is lower with respect to bulk dielectrics. For AlO_x and TiO_x, we determined values around 6, whereas bulk Al_2O_3 and TiO_2 feature values of 9 and 60. We think that the reason for the lowering of the permittivity with respect to the dielectric thickness is that the interfaces in which the crystal structure is formed perfectly plays an important role when the dielectric is only a few nanometers thick.

Further, we investigated SAM layers with respect to their application as tunnel barriers. Solely thin organic SAM-insulators are found not to be suitable for providing a tunnel barrier, since linear behaviour in the current-voltage characteristic has been observed which we interpreted as conductive paths in the dielectric. In other words, the arrangement of the molecules in the SAM layer does not provide a compact layer in which the direct contact of the electrodes can be avoided. Indeed, the combination of a plasma grown solid insulator and a SAM layer provides a very compact and quality insulator in which tunnel currents are low. That is why, this hybrid dielectrics are excellent candidates for transistors. For MIM diodes, the solely solid dielectric is the insulator of choice wherein TiO_x represent the best material. These findings are important not only in the field of infrared antennas, but since MIM diodes are also used in various other electronic and optoelectronic fields.

Using the nanotransfer printing process, we fabricated dipole antenna-like structures using two approaches, namely a MBE stamp and a Si wafer stamp transfer printed process. Using the first approach, we fabricated ultra thin antenna structure below 50 nm. With the second approach, the fabrication of large areas of millions of potential antenna structures was obtained. When combining the transfer printed antennas with a thermocouple that have been fabricated via electron beam lithography, an electrical signal was obtained when illuminating the antennas with a CO_2 laser. However, a clear polarization dependence could not be observed, and simulations with HFSS showed that the antennas were positioned to close to each other resulting in destructive interferences in the array. In order to avoid this effect, the spatial distance between the antennas was optimized.

After the optimization of the fabrication process and the individual rectenna components, we designed a fabrication a two-step transfer printing process for manufacturing almost 1 million antennas coupled to MIM tunneling nanodiodes over an area of 6 mm x 6 mm. For characterizing the rectennas, the array was divided into several sectors. The optoelectronic and electronic investigations showed unexpected results. The sectors in which a clear polarization dependence of the antenna response was obtained when illuminating with a CO_2 laser at 28 THz, showed a linear and symmetric I-V characteristic of the MIM junction. The sectors in which no antenna response was present showed an expected non-linear I-V characteristic. This results is in contradiction to theoretical models demonstrated previously in literature. We think that a thermal effect, namely the Seebeck effect, is responsible for the conversion of IR radiation (heat) into a constant voltage signal. These finding is in line with the latest results of our collaborators.

Further, when biasing eternally rectennas that featured a non-linear MIM diode, we found an antenna response under infrared illumination. We showed in this case that the response can be also explained with a standard bolometric effect which is a thermal effect. However, a rectification process of the MIM diodes can not be excluded completely.

In summary, we were able to fabricate rectenna arrays comprising MIM diodes featuring a nanoscale dielectric in a highly efficient nanotransfer printing process. The dipole antennas do not interfere destructively with each other which proves, that the fabrication of a large array of dipole antennas was successful. However, the main rectification process is in our array not due to the electronic rectification of our implemented MIM diode, but due to the formed thermocouple that outputs a constant voltage.

8.2 Outlook

Our work proved that nanotransfer printing is serious competitor to recent nanoscale and microscale fabrication methods. The process is faster, without the need of any polymers and low-cost. The quality of the fabricated structures until 50 nm is comparable with electron beam lithography fabricated structures. In future semiconductor and nanoelectronics applications, this fabrication technique can be implemented without the need for extensive basic research. Possible technical fields in which nanotransfer printing can provide an outstanding fabrication process might be nanomagnets, electrodes in solar cells or mirrors in laser resonators.

With respect to rectennas and rectenna arrays, an exciting future arises. Considering the Seebeck effect to be the dominant effect with respect to ob-

taining a constant antenna signal, new antenna and antenna array designs have to be carried out. The main advantage is that the ultra-thin dielectric can be avoided since metal-metal junction are needed rather than metal-insulator-metal junctions. The fabrication and implementation of that dielectric was the main challenge when fabricating rectennas. Besides the simplification of the antenna design, further investigations with respect to more efficient antennas have to carried out. Recently, a few groups proposed a bowtie antenna in this application which is a good step towards optimization. With respect to material properties, new material combinations have to be investigated in order to find the optimum materials for provided a large difference in their Seebeck coefficients.

When optimizing the materials and design, the performance of these devices can be increased and might be suitable as future detecting devices or even in the field of energy harvesting. A promising device with respect to the latter application would be a hybrid organic solar cell. Instead of using ITO as a conductive electrode, a metal grid could be fabricated on a glass substrate which serves as this electrode. Further, when exchanging this metal grid electrode to our transfer printed antenna array which includes thermocouple for extracting voltage, this array serves either as an electrode for the organic solar cell, and secondly, infrared light can be absorbed directly by the antenna array for which most organic solar cells are not sensitive. At the end, the overall performance of the solar cell is increased in this hybrid structure.

Appendix A

Process Parameters

A.1 Aluminum evaporation in Leybold UNIVEX 350G: Rate-established function

In the usual working mode of the Leybold UNIVEX 350G vacuum evaporator, the shutter above the sources and below the substrate are opened after a certain time. However, for some materials which are evaporated with fast deposition rates, the rate-established function feature advantages with respect to the time dependent mode. One of these materials is aluminum which surface roughness can be decreased when depositing with high rates. In this work, usual deposition rates of 10 A/s. The following amendments in the controller has to be done:

- Amount of Al for thickness of 40 nm: between 10 cm and 15 cm
- Proportional Gain: 5000
- Rate Established Time: 99 (the longest possible time)
- Rate Error: 30 %
- Soak Power: 44 %
- Predeposit Power: 55 %
- Predeposite Time: 5 s

AFM measurements reveal that the roughness is than decreased from 8-12 nm to about 5-6 nm.

A.2 Fabrication of SAM on Ti, Si, SiO_2 and Glass

In order to decrease the hydrophilicity of stamps or other silicon-based surfaces, a self-assembled monolayer (SAM) featuring a hydrophobic tail end, namely **1H,1H,2H,2H-Perflourooctyltrichlorosilane 97 %** (Alfa Aesar, Ward Hill, USA) is used. Since the SAM is in a liquid phase, a vapor depostion process is applied using a dessicator. The SAM can be applied directly on the surface of the sample or a plasma treatment (30 s) can be applied before in order to increase the amount of hydroxil groups on the surface on which the SAM adhere. The detailed deposition process of the SAM on the surface is described here:

- Sample and 3 droplets of SAM (0.5 ml) are placed on two separate Petri glasses
- Placing of the Petri glasses in a desiccator
- Evacuation of the chamber for 1 min (10 mbar)
- Self assembly take place within 15 min
- Annealing of sample on hotplate at 140°C for 30 min

The Petri glasses and the desiccator are cleaning with DI water, since the fluorine-based SAM are sensitive with respect to water (and humidity). IF necessary, the glasses can be cleaned in a subsequent step with acetone.

The SAM can also be applied on surfaces of materials, after the deposition of at least 10 nm of Ti on the surface of the sample.

Care has to be taken, since this SAM is highly toxic!!!.

A.3 Fabrication of SAM on GaAs

For decreasing the surface energy of MBE stamps, a thiol-based SAM, namely octadecylthiol (ODT) is used. The initial substrate for the stamps was a n-GaAs [001] wafer. The ODT should be stored under inert atmosphere, such as nitrogen or argon, since this SAM is also sensitive to humidity. The SAM consists of a powder. After etching, the wafer is rinsed in ethanol. The SAM are solved in ethanol in the following ratio:

ODT = 1.4 mg

EtOH = 3 ml

→ ODT solution = 2 mM

Figure A.1: Photograph of MBE stamp holder for SAM formation

Prior placing the SAM onto the target GaAs wafer, the native oxide of the wafer has to be etched by a HCl/EtOH (1/10 by volume) solution.

- Placing of 1mM ODT solution and sample in a flask under inert atmosphere
- Self assembly takes place during 20 h without any physical movement of flask
- Rinsing in ethanol and DI water
- Drying with nitrogen

Since the ODT SAM adhere well to GaAs, we assumed that this is also the case in AlGaAs alloys since they are lattice matched materials. Contact angle measurements proved this assumption.

In order to place 5 mm by 8 mm small MBE stamps vertically, for not destroying the nanoscale structures thereon, in a ODT solution, a special holder has been used. Figure A.1 shows a photograph of the syringe holder wherein the top has been removed: The plunger of the syringe features two trenches in which the stamps can be placed. In this way, the MBE stamps stand vertically. After pull in the plunger, the ODT solution is placed easily in the cavity featuring the MBE stamp. A cup featuring a ring closes the syringe, and the whole syringe is hanged on a metal bar. In this way, the syringe cannot fall and the ODT can

self assemble on the stamp for 20 h.

Comment: ODT are resistant against ultra sonic baths.

A.4 Optical Lithography

A.4.1 Negative resist

Optical Lithography was used for fabricating several microscale structures on various substrates. Since the goal was usually to deposit metals on the substrates, a negative photolithography process with a subsequent metal deposition and lift-off step was used. The exact process parameters for this process is given here.

Substrate cleaning:

- 10 min Acetone in Ultrasonic bath
- 10 min 2-Propanol in Ultrasonic bath
- drying with nitrogen

Spincoating of the photoresist on the sample (microresist ma-N 1420):

- 3000 rpm for 30 s. The thickness of the resist is 2µm afterwards
- 100°C annealing at a hotplate for 2 min
- cooling down for 5 min

A mask consisting of a transparent foil printed black structures thereon is used. This fabrication of the mask is low-cost and very fast. The UV exposure time was 15 s at a maskaligner with 700 $\frac{mW}{cm^2}$. For development, the ma-D 533s developer was used for 30 s. The development was stopped in DI water and the sample was been dried with nitrogen.

The metals were deposited in a thermal evaporator wherein an adhesion promoter has been always used as initial metal, such as Ti or Cr. This is important, since the lift-off process could also removed the deposited metals when the adhesion is not ideal. Lift-off has been done in acetone:

- duration depending on the size of the structures
- Ultrasonic bath sometimes useful to completely remove the resist

A.4.2 Positive resist

When chemical etching for structuring a surface is applied, a positive photoresist is the polymer of choice. We used the AZ 5214E from microresist. The substrate can be cleaned prior spin coating. After placing the sample on teh spin coater, the resist is dropped via a pipette on the substrate. The process parameters are presented here:

- 3000 rpm for 40 s.
- 100°C annealing at a hotplate for 5 min
- cooling down for 5 min

The sample and a mask (transparent foil featuring black structures thereon) are placed in a maskaligner. The UV exposure time was 60 s at a maskaligner with 700 $\frac{mW}{cm^2}$. For development, the AZ 400K developer was used which was diluted with DI water by 1:5. The development time was 17 s. The development was stopped in DI water and the sample was been dried with nitrogen.

After chemical treatment of the surface, the resist can be removed by acetone and propanol.

A.5 Fabrication of molybdenum shadow mask

Shadow mask for a structured evaporation process feature the advantage that afterwards, no polymer or solvents have to be applied on a surface after the metal deposition. Therefore, an adhesion promoter is not necessary. We fabricated molybdenum (Mo) shadow masks from a 100 µm thick Mo plate (Alfa Aesar). Using scissors, the exact dimensions of the mask that is needed can be just cut out of the plate. Booth sides of the Mo mask are covered with a positive photoresist. A transparent foil featuring black circles thereon with diameters down to 50 µm was placed thereon as a lithographic mask. After structuring the polymer, the Mo was etched in the windows of the resist.

- Acid: $H_2O : H_2SO_4 : HNO_3 = 3 : 1 : 1$
- Dropping of acid on the Mo sample using a pipette
- Exchanging every 5 min the acid using a syringe
- After 45 min, the structures are etched completely through the Mo plate

Finally, the Mo sample is rinsed in Di water and the resist is removed with aceton. As a consequence a Mo shadow mask is obtained. Figure A.2 presents a Si wafer featuring metal dots that were deposited through a shadow mask.

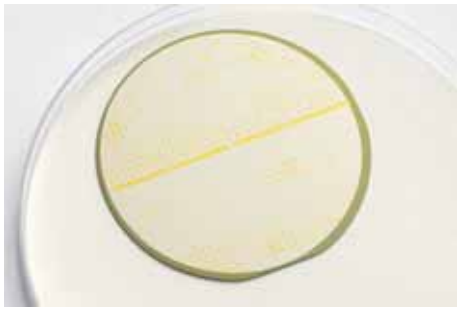

Figure A.2: Si wafer covered with a layer of aluminum (silver) featuring metal dots (gold) deposited through a Mo shadow mask.

A.6 Activation of surfaces (Hydrophilicity)

We transferred metal structures on several surfaces. In order to increase the adhesion between two layers, the surfaces are treated, in order to increase polar molecules on the surface which promotes the adhesion between two materials (activation). An overview on several materials and their activation processes are given in tabular A.1. The activation processes are shown here:

- Plasma treatment:
  - Placing sample in the chamber of the plasma asher
  - Applying vacuum (50 Pa)
  - Oxygen flow of 100 sccm
  - Plasma power at 200 W
- Piranha clean:
  - $H_2O_2 : H_2SO_4 = 1 : 4$ for 10 min.
  - Rinse in DI water
- RCA 1 (short treatment) [190]:
  - $H_2O : H_2O_2 : NH_4OH = 5 : 1 : 1$ for 30 s.
  - Rinse in DI water
- RCA 2 [190]:
  - $H_2O : H_2O_2 : HCl = 6 : 1 : 1$ for 10 min.
  - Rinse in DI water

Material	Activation
Si	plasma (2 min), piranha, RCA 2
SiO_2	RCA 1 + plasma treatment (2 min)
glass, quartz wafer	plasma (2 min), piranha, RCA 2
Ti	plasma (2 min), piranha
Al	plasma (2 min)
Au, AuPd	plasma (2 min)
SAM covered with metals	plasma (1 min)

Table A.1: Several materials are presented including their activation methods.

A.7 Transfer printing with Obducat

Most of the transfers were accomplished on the Obducat Nil-2.5 Nanoimprinter. After covering the stamp with a hydrophobic SAM and the deposition of metals and insulators, the stamp and the substrate were activated. After the activation, the substrate and the stamp were placed in the nanoimprinter wherein the side of the stamp comprising the structures was facing the activated side of the substrate. The larger sample is placed on the bottom and the smaller one thereon. The stack of samples is covered by 2 or 10 aluminum foils when using thicker or thinner foils, respectively. The subsequent process parameters in the Obducat Nanoimprinter are presented here:

Temperature (°C)	Pressure (bar)	Time (s)	UV
35	30	60	0
200	30	240	0
0	0	0	0

Table A.2: Transfer parameters for Obducat Nanoimprinter

After the transfer, the samples should be demolded when being still hot. In the case that an additional transfer is needed, the Obducat Nanoimprinter should be cooled down to room temperature again. In order to increase the cooling speed, liquid nitrogen can be added to the machine. The following recipe should be run in order to cool the machine:

Temperature (°C)	Pressure (bar)	Time (s)	UV
35	0	10	0
0	0	0	0

Table A.3: Cooling process of Obducat Nanoimprinter

Appendix B

P&ID of Leybold UNIVEX 350G

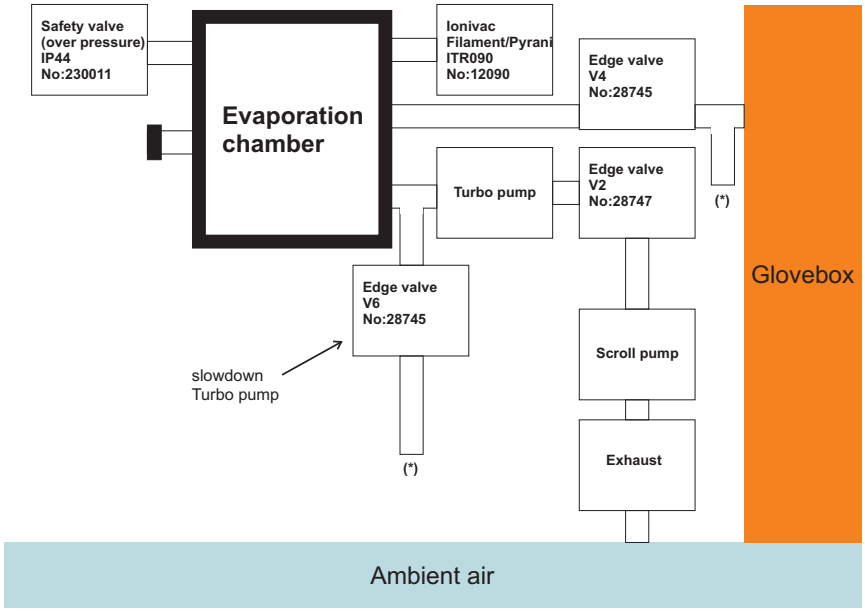

Figure B.1: The piping and instrumentation diagram (P&ID) of the thermal evaporator Leybold UNIVEX 350G is shown.

Appendix C

Stamp Designs

C.1 GaAs/AlGaAs MBE stamps for antenna structures

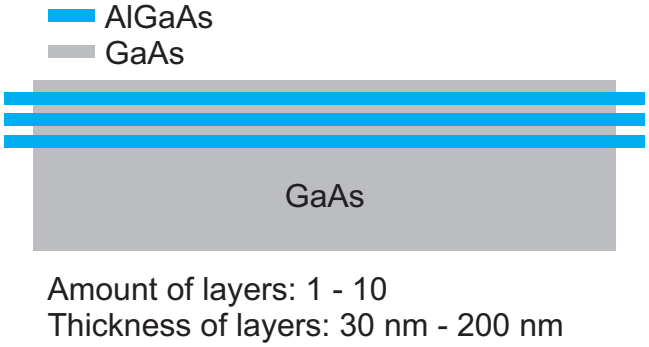

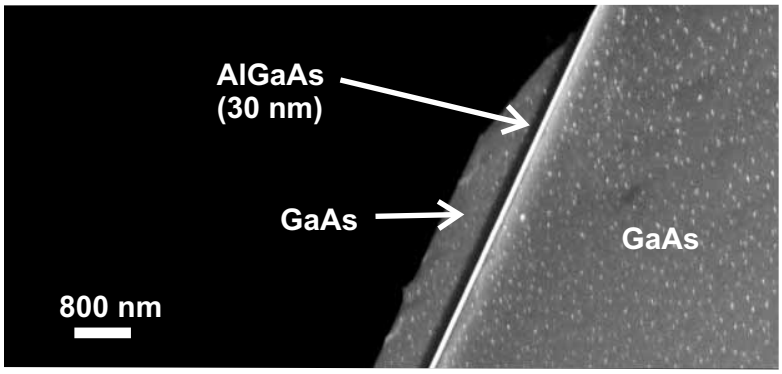

Figure C.1: Stamp Design GaAs (Antenna structure)

C.2 Si wafer stamps

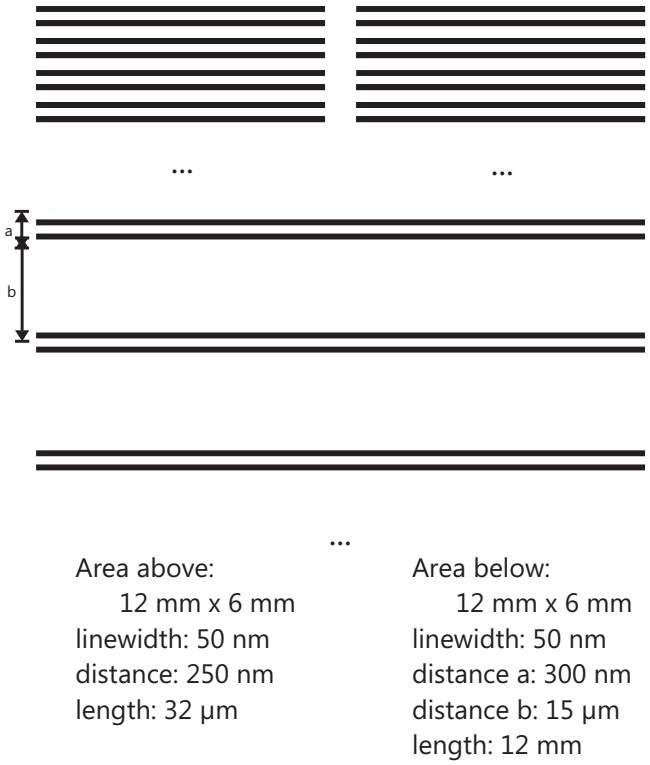

Figure C.2: Stamp Design A (Antenna structure)

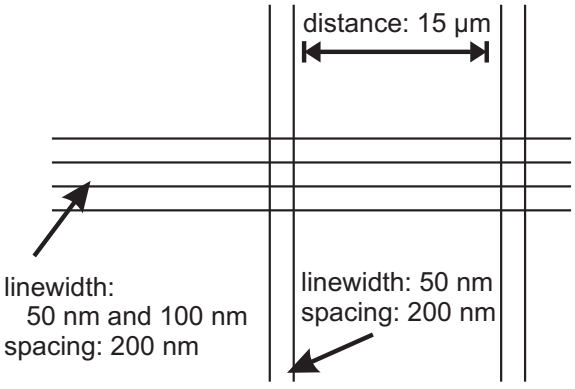

Figure C.3: Stamp Design B (Antenna structure)

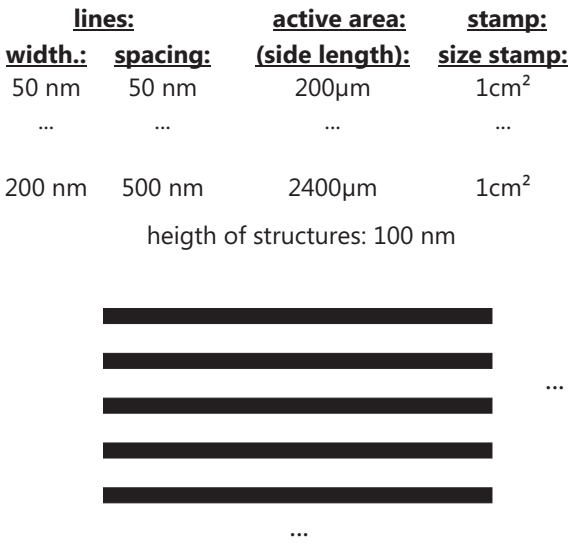

Figure C.4: Stamp Design C (Antenna structure)

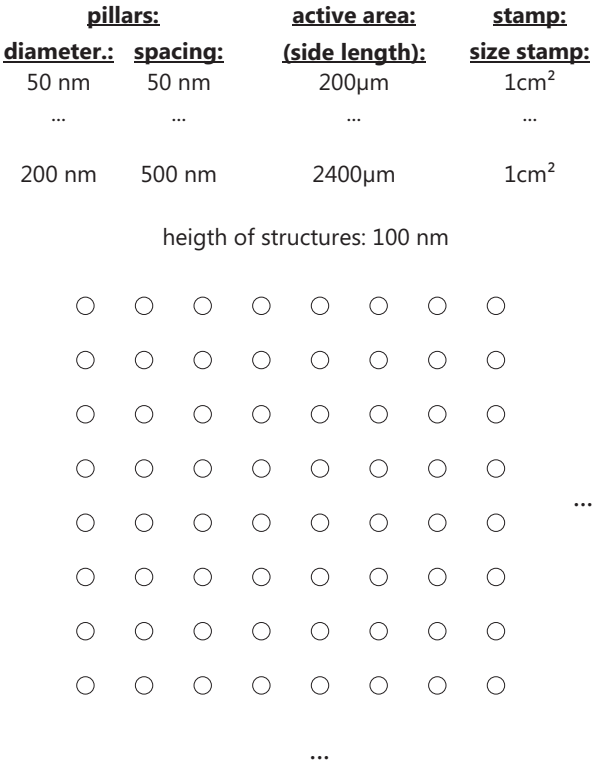

Figure C.5: Stamp Design D (MIM structure)

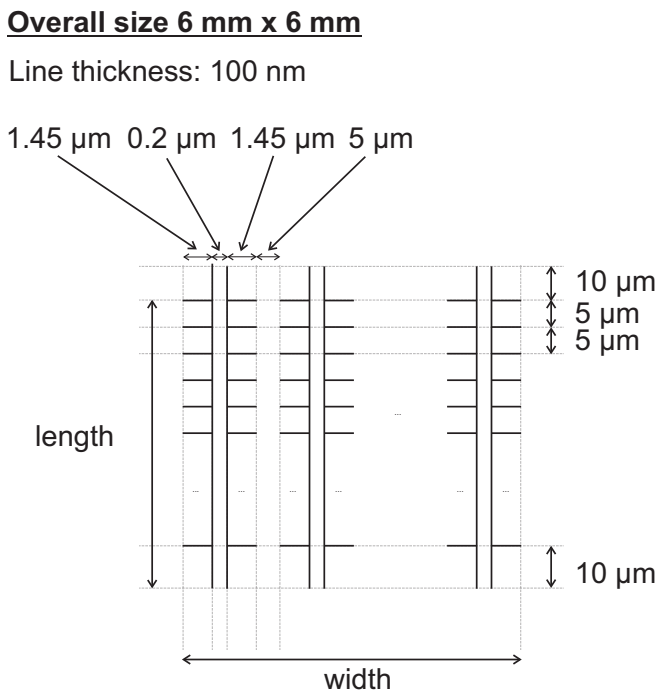

Figure C.6: Stamp Design E (rectenna array)

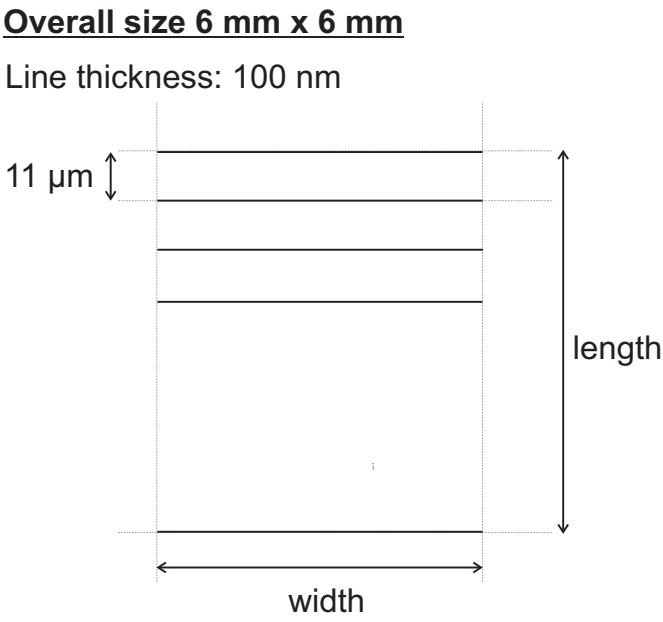

Figure C.7: Stamp Design F (rectenna array)

Publications

Results from this work have been presented previously in these Journals:

- Mario Bareiß, Peter M. Krenz, Gergo P. Szakmany, Daniel Kälblein, Alexei O. Orlov, Gary H. Bernstein, Giuseppe Scarpa, Bernhard Fabel, Ute Zschieschang, Hagen Klauk, Wolfgang Porod, and Paolo Lugli
  Infrared Nanoantenna Array fabricated by a Nanotransfer Printing Technique
  To be sbmitted

- Mario Bareiß, Peter M. Krenz, Gergo P. Szakmany, Daniel Kälblein, Alexei O. Orlov, Gary H. Bernstein, Giuseppe Scarpa, Bernhard Fabel, Ute Zschieschang, Hagen Klauk, Wolfgang Porod, and Paolo Lugli
  Rectennas Revisited
  Under review

- Mario Bareiß, Daniel Kälblein, Christian Jirauschek, Armin Exner, Ida Pavlichenkp, Bettina Lotsch, Ute Zschieschang, Hagen Klauk, Giuseppe Scarpa, Bernhard Fabel, Wolfgang Porod, and Paolo Lugli
  Ultra-Thin Titanium Oxide
  Applied Physics Letters (accepted) (2012)

- Mario Bareiß, Frederik Ante, Daniel Kälblein, Gunther Jegert, Christian Jirauschek, Giuseppe Scarpa, Bernhard Fabel, Edward M. Nelson, Gregory Timp, Ute Zschieschang, Hagen Klauk, Wolfgang Porod, and Paolo Lugli
  High-Yield Transfer Printing of Metal–Insulator–Metal Nanodiodes
  ACS Nano 6, 2853-2859 (2012)

- Mario Bareiß, Muhammad Atyab Imtaar, Bernhard Fabel, Giuseppe Scarpa, and Paolo Lugli
  Temperature enhanced large area nano transfer printing on Si/SiO2 substrates using Si wafer stamps
  Journal of Adhesion 87, 893-901 (2011)

- Mario Bareiß, Badri N. Tiwari, Andreas Hochmeister, Gunther Jegert, Ute Zschieschang, Hagen Klauk, Bernhard Fabel, Giuseppe Scarpa, Gregor Koblmüller, Gary H. Bernstein, Wolfgang Porod, and Paolo Lugli

Nano Antenna Array for Terahertz Detection
IEEE Transactions on Microwave Theory and Techniques 59, 2751-2757 (2011)

- Mario Bareiß, Andreas Hochmeister, Gunther Jegert, Ute Zschieschang, Hagen Klauk, Rupert Huber, Dirk Grundler, Wolfgang Porod, Bernhard Fabel, Giuseppe Scarpa, and Paolo Lugli
  Printed array of thin-dielectric metal-oxide-metal (MOM) tunneling diodes
  Journal of Applied Physics 110, 044316 (2011)

Results from this work have been presented previously in these book chapters:

- Mario Bareiß, Daniel Kälblein, Peter M. Krenz, Ute Zschieschang, Hagen Klauk, Giuseppe Scarpa, Bernhard Fabel, Wolfgang Porod, and Paolo Lugli
  Rectenna Solar Cells
  Large-Area Fabrication of Antennas and Nanodiodes
  Garret Moddel (Editor)
  Springer (2013)

- Mario Bareiß, Andreas Hochmeister, Gunther Jegert, Gregor Koblmüller, Ute Zschieschang, Hagen Klauk, Bernhard Fabel, Giuseppe Scarpa, Wolfgang Porod, and Paolo Lugli
  Nanoelectronic Device Applications Handbook
  Nano Antennas for Energy Conversion
  James E. Morris and Krzysztof Iniewski (Editors)
  Taylor and Francis Group (2012)

Results from this work have been presented previously in Conference proceedings:

- Benedikt Weiler, Mario Bareiß, Daniel Kälblein, Ute Zschieschang, Hagen Klauk, Giuseppe Scarpa, Bernhard Fabel, Wolfgang Porod, and Paolo Lugli
  Conductive AFM of transfer printed nano devices
  IEEE NANO 2012 Conference (Birmingham, UK 2012)

- Mario Bareiß, Benedikt Weiler, Daniel Kälblein, Ute Zschieschang, Hagen Klauk, Giuseppe Scarpa, Bernhard Fabel, Paolo Lugli, and Wolfgang Porod
  Nano-Transfer Printing of Functioning MIM Tunnel Diodes
  2012 IEEE Silicon Nanoelectronics Workshop (Honolulu, USA 2012)

- Mario Bareiß, Andreas Hochmeister, Gunther Jegert, Gregor Koblmüller, Ute Zschieschang, Hagen Klauk, Bernhard Fabel, Giuseppe Scarpa, Wolfgang Porod, and Paolo Lugli
  Energy Harvesting using Nano Antenna Array
  IEEE NANO 2011 Conference (Portland, USA 2011)

- Mario Bareiß, Andreas Hochmeister, Gunther Jegert, Ute Zschieschang, Hagen Klauk, Bernhard Fabel, Giuseppe Scarpa, Wolfgang Porod, and Paolo Lugli
  Quantum carrier dynamics in ultra-thin MIM tunneling diodes
  17th International Conference on Electron Dynamics in Semiconductors, Optoelectronics and Nanostructures (Santa Barbara, USA 2011)

- Johannes A. Russer, Paolo Lugli, Mario Bareiß, Yury Kuznetsov, Wolfgang Porod, Hristomir Yordanov, and Peter Russer
  Si and SiGe Based Monolithic Integrated Antennas for Electromagnetic Sensors and for Wireless Communications
  IEEE 11th Topical Meeting on Silicon Monolithic Integrated Circuits in RF Systems (SiRF), (Phoenix, USA 2011)

Results from this work have been presented previously in Conference and Workshops:

- Mario Bareiß, Andreas Hochmeister, Muhammad Atyab Imtaar, Gregor Koblmüller, Bernhard Fabel, Giuseppe Scarpa, and Paolo Lugli
  Infrared light absorbing devices fabricated by Nano Transfer Printing
  Nanosystems Initiative Munich Winter School (St. Christoph, Austria 2011)

- Andreas Hochmeister, Mario Bareiß, Ute Zschieschang, Hagen Klauk, Bernhard Fabel, Giuseppe Scarpa, and Paolo Lugli
  Thin isolators consisting of aluminum oxide and self-assembled monolayers for tunnel diodes
  75th Annual Meeting of the DPG and DPG Spring Meeting (Dresden, Germany 2011)

- Mario Bareiß, M. Atyab Imtaar, Anandi Yadav, Kuan Zhang, Andreas Hochmeister, Bernhard Fabel, Giuseppe Scarpa, Wolfgang Porod, Gregor Koblmüller, Gerhard Abstreiter and Paolo Lugli *Nanotransfer technology for device fabrication* 4th IGSSE Forum (Raitenhaslach, Germany 2010)

Reviewer for manuscripts related to this topic:

- Advanced Materials
  2012

List of Figures

Bibliography

[1] S. Keller, B. Schrader, A. Hoffmann, W. Schrader, K. Metz, A. Rehlaender, J. Pahnke, M. Ruwe, and W. Budach, Application of near-infrared-Fourier transform Raman spectroscopy in medical research, *Journal of Raman Spectroscopy* **25**, 663 (1994).

[2] M. Bareiss, B. Tiwari, A. Hochmeister, G. Jegert, U. Zschieschang, H. Klauk, B. Fabel, G. Scarpa, G. Koblmüller, G. Bernstein, W. Porod, and P. Lugli, Nano Antenna Array for Terahertz Detection, *IEEE Transactions on Microwave Theory and Techniques* **59**, 2751 (2011).

[3] M. Bareiss, A. Hochmeister, G. Jegert, G. Koblmüller, U. Zschieschang, H. Klauk, B. Fabel, G. Scarpa, W. Porod, and P. Lugli, Energy Harvesting using Nano Antenna Array, *11th IEEE Conference on Nanotechnology* (pp. 218–221) (2011).

[4] M. Bareiss, A. Hochmeister, G. Jegert, U. Zschieschang, H. Klauk, B. Fabel, G. Scarpa, W. Porod, and P. Lugli, Quantum carrier dynamics in ultra-thin MIM tunneling diodes, *EDISON17, Santa Barbara, USA* (2011).

[5] L. Hongzhong, C. Bangdao, L. Xin, L. Weihua, D. Yucheng, and L. A. Bingheng, Metal/Insulator/Metal Field-Emission Cannon, *Nanotechnol.* **22**, 455302 (2011).

[6] R. Waser and M. Aono, Nanoionics-Based Resistive Switching Memories, *Nat.Mater.* **6**, 833 (2007).

[7] M. Bareiss, F. Ante, D. Kälblein, G. Jegert, C. Jirauschek, G. Scarpa, B. Fabel, E. M. Nelson, G. Timp, U. Zschieschang, H. Klauk, W. Porod, and P. Lugli, High-Yield Transfer Printing of Metal–Insulator–Metal Nanodiodes, *ACS Nano* **6**, 2853 (2012).

[8] A. Hochmeister, *Nano Transfer Printing of Metal-Oxide-Metal Diodes for Energy Harvesting*, Diplomarbeit, Technische Universität München (2011).

[9] C. Kim, M. Prada, and R. H. Blick, Coulomb Blockade in a Coupled Nanomechanical Electron Shuttle, *ACS Nano* **6**, 651 (2012).

[10] M.-G. Kang and L. J. Guo, Semitransparent Cu electrode on a flexible substrate and its application in organic light emitting diodes, *Journal of Vacuum Science Technology B: Microelectronics and Nanometer Structures* **25**, 2637 (2007).

[11] M. Bareiss, D. Kälblein, C. Jirauschek, A. Exner, I. Pavlichenko, B. Lotsch, U. Zschieschang, H. Klauk, G. Scarpa, B. Fabel, W. Porod, and P. Lugli, Ultra-thin titanium oxide, *J. Appl. Phys.* **accepted** (2012).

[12] A. Rizzo, M. Mazzeo, M. Palumbo, G. Lerario, S. D'Amone, R. Cingolani, and G. Gigli, Hybrid Light-Emitting Diodes from Microcontact-Printing Double-Transfer of Colloidal Semiconductor CdSe/ZnS Quantum Dots onto Organic Layers, *Advanced Materials* **20**, 1886 (2008).

[13] M. Bareiss, D. Kälblein, P. M. Krenz, U. Zschieschang, H. Klauk, G. Scarpa, B. Fabel, W. Porod, and P. Lugli, Rectenna Solar Cells, Springer) (2013).

[14] M. A. Meitl, Y. Zhou, A. Gaur, S. Jeon, M. L. Usrey, M. S. Strano, and J. A. Rogers, Solution Casting and Transfer Printing Single-Walled Carbon Nanotube Films, *Nano Letters* **4**, 1643 (2004).

[15] X. Liang, Z. Fu, and S. Y. Chou, Graphene Transistors Fabricated via Transfer-Printing In Device Active-Areas on Large Wafer, *Nano Letters* **7**, 3840 (2007).

[16] R. R. Schaller, Moore´s law: past, present, and future, *IEEE Spectrum* **34**, 52 (1997).

[17] W. Shockley, The Path to the Conception of the Junction Transistor, *IEEE Trans. Electron Dev.* **23**, 597 (1976).

[18] G. E. Moore, Cramming more components onto integrated circuits, *Electronics* **38**, 1 (1965).

[19] C. Li, W. Fan, B. Lei, D. Zhang, S. Han, T. Tang, X. Liu, Z. Liu, S. Asano, M. Meyyappan, J. Han, and C. Zhou, Multilevel memory based on molecular devices, *Appl. Phys. Lett.* **84**, 1949 (2004).

[20] S. E. Thompson, M. Armstrong, C. Auth, M. Alavi, M. Buehler, R. Chau, S. Cea, T. Ghani, G. Glass, T. Hoffman, C.-H. Jan,

C. Kenyon, J. Klaus, K. Kuhn, Z. Ma, B. Mcintyre, K. Mistry, A. Murthy, B. Obradovic, R. Nagisetty, P. Nguyen, S. Sivakumar, R. Shaheed, L. Shifren, B. Tufts, S. Tyagi, M. Bohr, and Y. El-Mansy, A 90-nm Logic Technology Featuring Strained-Silicon, *IEEE Trans. Electron Dev.* **51**, 1790 (2004).

[21] P. Qi, A. Javey, M. Rolandi, Q. Wang, E. Yenilmez, and H. Dai, Miniature Organic Transistors with Carbon Nanotubes as Quasi-One-Dimensional Electrodes, *J. AM. CHEM. SOC.* **126**, 11774 (2004).

[22] O. Wood, C.-S. Koay, K. Petrillo, H. Mizuno, S. Raghunathana, J. Arnold, D. Horak, M. Burkhardt, G. Mcintyre, Y. Deng, B. L. Fontaine, U. Okoroanyanwu, A. Tchikoulaeva, T. Wallow, J. H.-C. Chen, M. Colburn, S. S.-C. Fan, B. S. Haran, and Y. Yin, Integration of EUV lithography in the fabrication of 22-nm node devices, *Proc. of SPIE* **7271**, 727104 (2009).

[23] S. Harrer, *Next-generation nanoimprint lithography: Innovative approaches towards improving flexibility and resolution of nanofabrication in the sub-15-nm region*, Ph.D. thesis, Technical University Munich (2008).

[24] A. K.-K. Wong, Resolution Enhancement Techniques in Optical Lithography, *SPIE-The International Society of Optical Engineering* (2001).

[25] T. L. Andrew, H.-Y. Tsai, and R. Menon, Confining Light to Deep Subwavelength Dimensions to Enable Optical Nanopatterning, *Science* **324**, 917 (2009).

[26] G. Pirio, P. Legagneux, D. Pribat, K. B. K. Teo, M. Chhowalla, G. A. J. Amaratunga, and W. I. Milne, Fabrication and electrical characteristics of carbon nanotube field emission microcathodes with an integrated gate electrode, *Nanotechnology* **13**, 1 (2002).

[27] C. Reese, M. Roberts, M. mang Ling, and Z. Bao, Organic thin film transistors, *Materials Today* **7**, 20 (2004).

[28] Y.-K. Choi, T.-J. King, and C. Hu, Nanoscale CMOS spacer FinFET for the terabit era, *Electron Device Letters, IEEE* **23**, 25 (2002).

[29] C. Vieu, F. Carcenac, A. Pépin, Y. Chen, M. Mejias, A. Lebib, L. Manin-Ferlazzo, L. Couraud, and H. Launois, Electron beam lithography: resolution limits and applications, *Applied Surface Science* **164**, 111 (2000).

[30] S. T. Bartsch, A. Lovera, D. Grogg, and A. M. Ionescu, Nanomechanical Silicon Resonators with Intrinsic Tunable Gain and Sub-nW Power Consumption, *ACS Nano* **6**, 256 (2012).

[31] I. Martini, J. Dechow, M. Kamp, A. Forchel, and J. Koeth, GaAs field effect transistors fabricated by imprint lithography, *Microelectronic Engineering* **60**, 451 (2002).

[32] S. Y. Chou, P. R. Krauss, and P. J. Renstrom, Imprint of sub-25 nm vias and trenches in polymers, *Applied Physics Letters* **67**, 3114 (1995).

[33] S. Y. Chou, P. R. Krauss, and P. J. Renstrom, Nanoimprint lithography, *The 40th international conference on electron, ion, and photon beam technology and nanofabrication* **14**, 4129 (1996).

[34] S. Harrer, S. Strobel, G. Scarpa, G. Abstreiter, M. Tornow, and P. Lugli, Room Temperature Nanoimprint Lithography Using Molds Fabricated by Molecular Beam Epitaxy, *IEEE Transactions on Nanotechnology* **7**, 363 (2008).

[35] A. M. Saleem, J. Berg, V. Desmaris, and M. S. Kabir, Nanoimprint lithography using vertically aligned carbon nanostructures as stamps, *Nanotechnology* **20**, 375302 (2009).

[36] L. J. Guo, Recent progress in nanoimprint technology and its applications, *Journal of Physics D: Applied Physics* **37**, R123 (2004).

[37] L. Guo, Nanoimprint Lithography: Methods and Material Requirements, *Advanced Materials* **19**, 495 (2007).

[38] D. Mijatovic, J. C. T. Eijkel, and A. van den Berg, Technologies for nanofluidic systems: top-down vs. bottom-up-a review, *Lab Chip* **5**, 492 (2005).

[39] W. Lu and C. M. Lieber, Nanoelectronics from the bottom up, *Nat Mat* **6**, 841 (2007).

[40] G. B. Sigal, C. Bamdad, A. Barberis, J. Strominger, and G. M. Whitesides, A Self-Assembled Monolayer for the Binding and Study of Histidine-Tagged Proteins by Surface Plasmon Resonance, *Analytical Chemistry* **68**, 490 (1996).

[41] E. Ben-Jacob, Z. Hermon, and S. Caspi, DNA transistor and quantum bit element: Realization of nano-biomolecular logical devices, *Physics Letters A* **263**, 199 (1999).

[42] P. Stadler, K. Oppelt, T. B. Singh, J. G. Grote, R. Schwödiauer, S. Bauer, H. Piglmayer-Brezina, D. Bäuerle, and N. S. Sariciftci, Organic field-effect transistors and memory elements using deoxyribonucleic acid (DNA) gate dielectric, *Organic Electronics* **8**, 648 (2007).

[43] R. T. Weitz, U. Zschieschang, F. Effenberger, H. Klauk, M. Burghard, and K. Kern, High-Performance Carbon Nanotube Field Effect Transistors with a Thin Gate Dielectric Based on a Self-Assembled Monolayer, *Nano Letters* **7**, 22 (2007).

[44] M. Bareiss, M. A. Imtaar, B. Fabel, G. Scarpa, and P. Lugli, Temperature Enhanced Large Area Nano Transfer Printing on Si/SiO2 Substrates Using Si Wafer Stamps, *The Journal of Adhesion* **87**, 893 (2011).

[45] J. Zaumseil, M. A. Meitl, J. W. P. Hsu, B. R. Acharya, K. W. Baldwin, Y.-L. Loo, and J. A. Rogers, Three-Dimensional and Multilayer Nanostructures Formed by Nanotransfer Printing, *Nano Letters* **3**, 1223 (2003).

[46] Y.-L. Loo, R. L. Willett, K. W. Baldwin, and J. A. Rogers, Interfacial Chemistries for Nanoscale Transfer Printing, *Journal of the American Chemical Society* **124**, 7654 (2002).

[47] Y.-L. Loo, D. V. Lang, J. A. Rogers, and J. W. P. Hsu, Electrical Contacts to Molecular Layers by Nanotransfer Printing, *Nano Letters* **3**, 913 (2003).

[48] R. Enzmann, M. Bareiss, D. Baierl, N. Hauke, G. Böhm, R. Meyer, J. Finley, and M.-C. Amann, Design and realization of low density InAs quantum dots on AlGaInAs lattice matched to InP, *Journal of Crystal Growth* **312**, 2300 (2010).

[49] J. G. C. Veinot, H. Yan, S. M. Smith, J. Cui, Q. Huang, and T. J. Marks, Fabrication and Properties of Organic Light-Emitting "Nanodiode" Arrays, *Nano Letters* **2**, 333 (2002).

[50] B. Liu, K. Y. Kim, Y. Huang, and S.-T. Ho, Nanophotodetector Array for Near-Field Imaging, in: *Frontiers in Optics*, (p. FThL4) (Optical Society of America, 2008).

[51] A. Hohenau, H. Ditlbacher, B. Lamprecht, J. R. Krenn, A. Leitner, and F. R. Aussenegg, Electron beam lithography, a helpful tool for nanooptics, *Microelectronic Engineering* **83**, 1464 (2006), ¡ce:title¿Micro- and Nano-Engineering MNE 2005¡/ce:title¿ ¡xocs:full-name¿Proceedings of the 31st International Conference on Micro- and Nano-Engineering¡/xocs:full-name¿.

[52] Q. Feng, On Determining Specifications and Selections of Alternative Technologies for Airport Checked-Baggage Security Screening, *Risk Analysis* **27**, 1299 (2007).

[53] F. Pristera, M. Halik, A. Castelli, and W. Fredericks, Analysis of Explosives Using Infrared Spectroscopy, *Analytical Chemistry* **32**, 495 (1960).

[54] R. Wood, C. Han, and P. Kruse, Integrated uncooled infrared detector imaging arrays, in: *Solid-State Sensor and Actuator Workshop, 1992. 5th Technical Digest., IEEE*, (pp. 132 –135) (1992).

[55] Y. Tawada, M. Kondo, H. Okamoto, and Y. Hamakawa, Hydrogenated amorphous silicon carbide as a window material for high efficiency a-Si solar cells, *Solar Energy Materials* **6**, 299 (1982).

[56] A. Rogalski, Infrared detectors: an overview, *Infrared Physics and Technology* **43**, 187 (2002).

[57] J. Yan, M.-H. Kim, J. A. Elle, A. B. Sushkov, G. S. Jenkins, H. M. Milchberg, M. S. Fuhrer, and H. D. Drew, Dual-gated bilayer graphene hot-electron bolometer, *Nat. Nanotechnol.* **7**, 472 (2012).

[58] L. Hocker, D. Sokoloff, V. Daneu, A. Szoke, and A. Javan, FREQUENCY MIXING IN THE INFRARED AND FAR-INFRARED USING A METAL-TO-METAL POINT CONTACT DIODE, *Appl. Phys. Lett.* **12**, 401 (1968).

[59] C. Fumeaux, W. Herrmann, F. Kneubühl, H. Rothuizen, B. Lipphardt, and C. Weiss, Nanometer thin-film Ni-NiO-Ni diodes for mixing 28 THz CO2-laser emissions with difference frequencies up to 176 GHz, *Applied Physics B: Lasers and Optics* **66**, 327 (1998), 10.1007/s003400050396.

[60] J. Bean, B. Tiwari, G. Szakmany, G. Bernstein, P. Fay, and W. Porod, Long wave infrared detection using dipole antenna-coupled metal-oxide-metal diodes, in: *Infrared, Millimeter and Terahertz Waves, 2008. IRMMW-THz 2008. 33rd International Conference on*, (pp. 1 –2) (2008).

[61] B. A. Slovick, J. A. Bean, P. M. Krenz, and G. D. Boreman, Directional control of infrared antenna-coupled tunnel diodes, *Opt. Express* **18**, 20960 (2010).

[62] M. Bareiss, P. M. Krenz, G. P. Szakmany, B. Tiwari, D. Kälblein, A. O. Orlov, G. H. Bernstein, G. Scarpa, B. Fabel, U. Zschieschang, H. Klauk, W. Porod, and P. Lugli, Rectennas Revisited, *under review* (2012).

[63] M. Razeghi, Current status and future trends of infrared detectors, *Opto-Electron. Rev.* **6**, 155 (1998).

[64] S. Grover and G. Moddel, Applicability of Metal/Insulator/Metal (MIM) Diodes to Solar Rectennas, *Photovoltaics, IEEE Journal of* **1**, 78 (2011).

[65] M. Bareiss, A. Hochmeister, G. Jegert, U. Zschieschang, H. Klauk, R. Huber, D. Grundler, W. Porod, B. Fabel, G. Scarpa, and P. Lugli, Printed array of thin-dielectric metal-oxide-metal (MOM) tunneling diodes, *Journal of Applied Physics* **110**, 044316 (2011).

[66] J. A. Bean, A. Weeks, and G. D. Boreman, Performance Optimization of Antenna-Coupled Al-AlO_x-Pt Tunnel Diode Infrared Detectors, *IEEE Journal of Quantum Electronics* **47**, 126 (2011).

[67] S. M. George, Atomic Layer Deposition: An Overview, *Chemical Reviews* **110**, 111 (2010).

[68] C. Seidel, *Charakterisierung von InP–basierten Quantenpunkten und Nano–Resonatoren für effiziente Einzelphotonenerzeugung*, Diplomarbeit, Technische Universität München (2008).

[69] M. Bareiss, *InAs Quantenpunkte auf Inp-Substrat für eine Einzelphotonenquelle bei 1,55 m*, Diplomarbeit, Technische Universität München (2009).

[70] C.-W. Wu, T. Aoki, and M. Kuwabara, Electron-beam lithography assisted patterning of surfactant-templated mesoporous thin films, *Nanotechnology* **15**, 1886 (2004).

[71] C. Vieu, F. Carcenac, A. Päpin, Y. Chen, M. Mejias, A. Lebib, L. Manin-Ferlazzo, L. Couraud, and H. Launois, Electron beam lithography: resolution limits and applications, *Applied Surface Science* **164**, 111 (2000).

[72] C. S. Torres, S. Zankovych, J. Seekamp, A. Kam, C. C. Cedeäo, T. Hoffmann, J. Ahopelto, F. Reuther, K. Pfeiffer, G. Bleidiessel, G. Gruetzner, M. Maximov, and B. Heidari, Nanoimprint lithography: an alternative nanofabrication approach, *Materials Science and Engineering C* **23**, 23 (2003).

[73] S. H. Kim, K.-D. Lee, J.-Y. Kim, M.-K. Kwon, and S.-J. Park, Fabrication of photonic crystal structures on light emitting diodes by nanoimprint lithography, *Nanotechnology* **18**, 055306 (2007).

[74] M. D. Austin, W. Zhang, H. Ge, D. Wasserman, S. A. Lyon, and S. Y. Chou, 6 nm half-pitch lines and 0.04 m static random access memory patterns by nanoimprint lithography, *Nanotechnology* **16**, 1058 (2005).

[75] K. J. Morton, G. Nieberg, S. Bai, and S. Y. Chou, Wafer-scale patterning of sub-40 nm diameter and high aspect ratio ($> 50 : 1$) silicon pillar arrays by nanoimprint andÂ etching, *Nanotechnology* **19**, 345301 (2008).

[76] H. Yoo, H. Shin, B. Sim, S. Kim, and M. Lee, Parallelized laser-direct patterning of nanocrystalline metal thin films by use of a pulsed laser-induced thermo-elastic force, *Nanotechnology* **20**, 245301 (2009).

[77] S. Strobel, S. Harrer, G. Penso Blanco, G. Scarpa, G. Abstreiter, P. Lugli, and M. Tornow, Planar Nanogap Electrodes by Direct Nanotransfer Printing, *Small* **5**, 579 (2009).

[78] S. Kulinich and M. Farzaneh, Hydrophobic properties of surfaces coated with fluoroalkylsiloxane and alkylsiloxane monolayers, *Materials Science and Engineering C* **573**, 379 (2004).

[79] D. Suh, J. Rhee, and H. H. Lee, Bilayer reversal imprint lithography: direct metal-polymer transfer, *Nanotechnology* **15**, 1103 (2004).

[80] D. Li and L. J. Guo, Organic thin film transistors and polymer light-emitting diodes patterned by polymer inking and stamping, *Journal of Physics D: Applied Physics* **41**, 105115 (2008).

[81] J. ho Choi, K.-H. Kim, S.-J. Choi, and H. H. Lee, Whole device printing for full colour displays with organic light emitting diodes, *Nanotechnology* **17**, 2246 (2006).

[82] J. Rhee and H. H. Lee, Patterning organic light-emitting diodes by cathode transfer, *Applied Physics Letters* **81**, 4165 (2002).

[83] M. C. Huang, Y. Zhou, and C. J. Chang-Hasnain, A surface-emitting laser incorporating a high-index-contrast subwavelength grating, *Nat Photonics* **1**, 119 (2007).

[84] E. L. Tan, K. O. Aung, R. Sbiaa, S. K. Wong, H. K. Tan, W. C. Poh, S. N. Piramanayagam, and C. C. Chum, Nanoimprint mold fabrication and duplication for embedded servo and discrete track recording media, *Journal of Vacuum Science & Technology B: Microelectronics and Nanometer Structures* **27**, 2259 (2009).

[85] S. Y. Chou, P. R. Krauss, and P. J. Renstrom, Imprint Lithography with 25-Nanometer Resolution, *Science* **272**, 85 (1996).

[86] S. Shibuichi, T. Yamamoto, T. Onda, and K. Tsujii, Super Water- and Oil-Repellent Surfaces Resulting from Fractal Structure, *Journal of Colloid and Interface Science* **208**, 287 (1998).

[87] H. Sun, J. Liu, P. Gu, and D. Chen, Anti-sticking treatment for a nanoimprint stamp, *Applied Surface Science* **254**, 2955 (2008).

[88] Y. H. D. K. Masatoshi Nakamura, Toru Aoki and J. Engemann, Comparison of hydrophilic properties of amorphous TiO x films obtained by radio frequency sputtering and plasma-enhanced chemical vapor deposition., *Journal of Materials Research* **16**, 621 (2001), 10.1557/JMR.2001.0089.

[89] M. R. Alexander, S. Payan, and T. M. Duc, Interfacial interactions of plasma-polymerized acrylic acid and an oxidized aluminium surface investigated using XPS, FTIR and poly(acrylic acid) as a model compound, *Surface and Interface Analysis* **26**, 961 (1998).

[90] A. Nylund and I. Olefjord, Surface analysis of oxidized aluminium. 1. Hydration of Al_2O_3 and decomposition of $Al(OH)_3$ in a vacuum as studied by ESCA, *Surface and Interface Analysis* **21**, 283 (1994).

[91] M. R. Alexander, G. E. Thompson, and G. Beamson, Characterization of the oxide/hydroxide surface of aluminium using x-ray photoelectron spectroscopy: a procedure for curve fitting the O 1s core level, *Surface and Interface Analysis* **29**, 468 (2000).

[92] S.-H. Hur, D.-Y. Khang, C. Kocabas, and J. A. Rogers, Nanotransfer printing by use of noncovalent surface forces: Applications to thin-film transistors that use single-walled carbon nanotube networks and semiconducting polymers, *Applied Physics Letters* **85**, 5730 (2004).

[93] G. Kissinger and W. Kissinger, Hydrophilicity of Silicon Wafers for Direct Bonding, *physica status solidi (a)* **123**, 185 (1991).

[94] G. Bellussi, A. Carati, M. G. Clerici, G. Maddinelli, and R. Millini, Reactions of titanium silicalite with protic molecules and hydrogen peroxide, *Journal of Catalysis* **133**, 220 (1992).

[95] J. A. jr. and K. Wickersheim, Near infrared characterization of water and hydroxyl groups on silica surfaces, *Surface Science* **2**, 252 (1964).

[96] G. Csaba and W. Porod, Simulation of Field Coupled Computing Architectures Based on Magnetic Dot Arrays, *Journal of Computational Electronics* **1**, 87.

[97] G. Csaba, A. Imre, G. H. Bernstein, W. Porod, and V. Metlushko, Nanocomputing by field-coupled nanomagnets, *IEEE Transactions on Nanotechnology* **1**, 209 (2002).

[98] A. H. Bobeck, R. F. Fischer, and A. J. Perneski, A new approach to memory and logic-cylindrical domain devices, in: *Proceedings of the November 18-20, 1969, fall joint computer conference*, AFIPS '69 (Fall), (pp. 489–498) (ACM, New York, NY, USA, 1969).

[99] C. Baatar, W. Porod, and T. Roska, Cellular Nanoscale Sensory Wave Computing, Springer Publishing Company (2009).

[100] J. G. Simmons, Generalized Formula for the Electric Tunnel Effect between Similar Electrodes Separated by a Thin Insulating Film, *Journal of Applied Physics* **34**, 1793 (1963).

[101] R. H. Fowler and L. Nordheim, Electron Emission in Intense Electric Fields, *Proceedings of the Royal Society of London. Series A, Containing Papers of a Mathematical and Physical Character* **119**, 173 (1928).

[102] A. Sommerfeld and H. Bethe, *Handbuch der Physik von Geiger und Scheel*, vol. 24/2 (Julius-Springer-Verlag Berlin, 1933).

[103] M. Heiblum, S. Wang, T. Gustafson, and J. Whinnery, IIb-7 edge-MOM diode: An integrated, optical, non-linear device, *IEEE Transactions on Electron Devices* **24**, 1199 (1977).

[104] H. M. Gupta and R. J. V. Overstraeten, Role of trap states in the insulator region for MIM characteristics, *Journal of Applied Physics* **46**, 2675 (1975).

[105] G. Jegert, A. Kersch, W. Weinreich, and P. Lugli, Monte Carlo Simulation of Leakage Currents in TiN/ZrO_2/TiN Capacitors, *IEEE Transactions on Electron Devices* **58**, 327 (2011).

[106] D. Diesing, M. Merschdorf, A. Thon, and W. Pfeiffer, Identification of multiphoton induced photocurrents in metal-insulator-metal junctions, *Applied Physics B: Lasers and Optics* **78**, 443 (2004).

[107] T. W. Hickmott, Temperature-dependent Fowler–Nordheim tunneling and a compensation effect in anodized Al-Al_2O_3-Au diodes, *Journal of Applied Physics* **97**, 104505 (2005).

[108] N. F. Mott, Conduction in non-crystalline materials, *Philosophical Magazine* **19**, 832 (1969).

[109] G. D. Wilk, R. M. Wallace, and J. M. Anthony, High-kappa gate dielectrics: Current status and materials properties considerations, *Journal of Applied Physics* **89**, 5243 (2001).

[110] J. A. Bean, B. Tiwari, G. H. Bernstein, P. Fay, and W. Porod, Thermal infrared detection using dipole antenna-coupled metal-oxide-metal diodes, *Journal of Vacuum Science & Technology B: Microelectronics and Nanometer Structures* **27**, 11 (2009).

[111] P. Periasamy, J. J. Berry, A. A. Dameron, J. D. Bergeson, D. S. Ginley, R. P. O'Hayre, and P. A. Parilla, Fabrication and Characterization of MIM Diodes Based on Nb/Nb2O5 Via a Rapid Screening Technique, *Advanced Materials* **23**, 3080 (2011).

[112] T. Sekitani, U. Zschieschang, H. Klauk, and T. Someya, Flexible organic transistors and circuits with extreme bending stability, *Nat Mater* **9**, 1015 (2010).

[113] D. K. Schwartz, MECHANISMS AND KINETICS OF SELF-ASSEMBLED MONOLAYER FORMATION, *Annual Review of Physical Chemistry* **52**, 107 (2001).

[114] U. Zschieschang, F. Ante, M. Schlärholz, M. Schmidt, K. Kern, and H. Klauk, Mixed Self-Assembled Monolayer Gate Dielectrics for Continuous Threshold Voltage Control in Organic Transistors and Circuits, *Advanced Materials* **22**, 4489 (2010).

[115] M. Lafkioti, B. Krauss, T. Lohmann, U. Zschieschang, H. Klauk, K. v. Klitzing, and J. H. Smet, Graphene on a Hydrophobic Substrate: Doping Reduction and Hysteresis Suppression under Ambient Conditions, *Nano Letters* **10**, 1149 (2010).

[116] R. Maboudian and R. T. Howe, Critical Review: Adhesion in surface micromechanical structures, *Journal of Vacuum Science & Technology B: Microelectronics and Nanometer Structures* **15**, 1 (1997).

[117] W. Lee, R. Ji, C. Ross, U. Gäsele, and K. Nielsch, Wafer-Scale Ni Imprint Stamps for Porous Alumina Membranes Based on Interference Lithography, *Small* **2**, 978 (2006).

[118] P. Russer, N. Fichtner, P. Lugli, W. Porod, J. Russer, and H. Yordanov, Nanoelectronics-Based Integrated Antennas, *IEEE Microwave Magazine* **2010**, 58 (2010).

[119] R. T. Weitz, U. Zschieschang, A. Forment-Aliaga, D. Kälblein, M. Burghard, K. Kern, and H. Klauk, Highly Reliable Carbon Nanotube Transistors with Patterned Gates and Molecular Gate Dielectric, *Nano Letters* **9**, 1335 (2009).

[120] H. Ryu, D. Kälblein, R. T. Weitz, F. Ante, U. Zschieschang, K. Kern, O. G. Schmidt, and H. Klauk, Logic circuits based on individual semiconducting and metallic carbon-nanotube devices, *Nanotechnology* **21**, 475207 (2010).

[121] Surface modification of titanium oxide in pulse-modulated induction thermal plasma, *Thin Solid Films* **390**, 20 (2001).

[122] G. Jegert, A. Kersch, W. Weinreich, U. Schroder, and P. Lugli, Modeling of leakage currents in high-kappa dielectrics: Three-dimensional approach via kinetic Monte Carlo, *Applied Physics Letters* **96**, 062113 (2010).

[123] R. Tsu and L. Esaki, Tunneling in a finite superlattice, *Applied Physics Letters* **22**, 562 (1973).

[124] J. Robertson, Band offsets and work function control in field effect transistors, vol. 27, (pp. 277–285) (AVS, 2009).

[125] J. Robertson, Band offsets of wide-band-gap oxides and implications for future electronic devices, vol. 18, (pp. 1785–1791) (AVS, 2000).

[126] T. W. Hickmott, Temperature-dependent Fowler–Nordheim tunneling and a compensation effect in anodized Al–Al_2O_3–Au diodes, *Journal of Applied Physics* **97**, 104505 (2005).

[127] V. K. Gueorguiev, P. V. Aleksandrova, T. E. Ivanov, and J. B. Koprinarova, Hysteresis in metal insulator semiconductor structures with high temperature annealed ZrO_2/SiO_x layers, *Thin Solid Films* **517**, 1815 (2009).

[128] T. D. Lin, H. C. Chiu, P. Chang, L. T. Tung, C. P. Chen, M. Hong, J. Kwo, W. Tsai, and Y. C. Wang, High-performance self-aligned inversion-channel $In_{0.53}Ga_{0.47}As$ metal-oxide-semiconductor field-effect-transistor with $Al_2O_3/Ga_2O_3(Gd_2O_3)$ as gate dielectrics, *Applied Physics Letters* **93**, 033516 (2008).

[129] M. Groner, J. Elam, F. Fabreguette, and S. George, Electrical characterization of thin Al_2O_3 films grown by atomic layer deposition on silicon and various metal substrates, *Thin Solid Films* **413**, 186 (2002).

[130] T. W. Hickmott, Interface states at the anodized Al_2O_3-metal interface, *Journal of Applied Physics* **89**, 5502 (2001).

[131] C. A. Mead, Anomalous Capacitance of Thin Dielectric Structures, *Phys. Rev. Lett.* **6**, 545 (1961).

[132] P. V. Kamat, Quantum Dot Solar Cells. Semiconductor Nanocrystals as Light Harvesters, *The Journal of Physical Chemistry C* **112**, 18737 (2008).

[133] M. G. Sung, H. Lee, K. Heo, K.-E. Byun, T. Kim, D. H. Seo, S. Seo, and S. Hong, Scanning Noise Microscopy on Graphene Devices, *ACS Nano* **5**, 8620 (2011).

[134] C. Jirauschek, Accuracy of Transfer Matrix Approaches for Solving the Effective Mass Schrödinger Equation, *Quantum Electronics, IEEE Journal of* **45**, 1059 (2009).

[135] N. S. Wingreen, K. W. Jacobsen, and J. W. Wilkins, Resonant Tunneling with Electron-Phonon Interaction: An Exactly Solvable Model, *Phys. Rev. Lett.* **61**, 1396 (1988).

[136] D. Baierl, B. Fabel, P. Lugli, and G. Scarpa, Efficient indium-tin-oxide (ITO) free top-absorbing organic photodetector with highly transparent polymer top electrode, *Organic Electronics* **12**, 1669 (2011).

[137] J. Robertson, High dielectric constant gate oxides for metal oxide Si transistors, *Rep. Prog. Phys.* **69**, 327 (2005).

[138] Y. H. Lee, K. K. Chan, and M. J. Brady, Plasma enhanced chemical vapor deposition of TiO2 in microwave radio frequency hybrid plasma reactor, *J. Vac. Sci. Technol. A* **13**, 596 (1995).

[139] B. H. Lee, Y. Jeon, K. Zawadzki, W.-J. Qi, and J. Lee, Effects of interfacial layer growth on the electrical characteristics of thin titanium oxide films on silicon, *Appl. Phys. Lett.* **74**, 3143 (1999).

[140] S. K. Kim, S. Y. Lee, M. Seo, G.-J. Choi, and C. S. Hwang, Impact of O3 feeding time on TiO2 films grown by atomic layer deposition for memory capacitor applications, *J. Appl. Phys.* **102**, 024109 (2007).

[141] H. Klauk, U. Zschieschang, J. Pflaum, and M. Halik, Ultralow-power organic complementary circuits, *Nature* **445**, 745 (2007).

[142] H. G. Tompkins, T. Zhu, and E. Chen, Determining thickness of thin metal films with spectroscopic ellipsometry for applications in magnetic random-access memory, *J. Vac. Sci. Technol. A* **16**, 1297 (1998).

[143] D. Yugang, Z. Yuan, T. Yiping, and L. Dichen, Nano-TiO2-modified photosensitive resin for RP, *Rap. Prot. J.* **17**, 247 (2011).

[144] J. N. Hilfiker, N. Singh, T. Tiwald, D. Convey, S. M. Smith, J. H. Baker, and H. G. Tompkins, Survey of methods to characterize thin absorbing films with Spectroscopic Ellipsometry, *Thin Solid Films* **516**, 7979 (2008).

[145] N. Rausch and E. Burte, Thin High-Dielectric TiO2 Films Prepared by Low Pressure MOCVD, *Microelectron. Eng.* **19**, 725 (1992).

[146] M. D. Stamate, Dielectric properties of TiO2 thin films deposited by a DC magnetron sputtering system, *Thin Solid Films* **372**, 246 (2000).

[147] Q. Xie and Y.-L. Jiang, Atomic layer deposition of TiO2 from tetrakis-dimethyl-amido titanium or Ti isopropoxide precursors and H2O, *J. Appl. Phys.* **102**, 083521 (2007).

[148] M. Irimia-Vladu, E. D. Glowacki, P. A. Troshin, G. Schwabegger, L. Leonat, D. K. Susarova, O. Krystal, M. Ullah, Y. Kanbur, M. A. Bodea, V. F. Razumov, H. Sitter, S. Bauer, and N. S. Sariciftci, Indigo - A Natural Pigment for High Performance Ambipolar Organic Field Effect Transistors and Circuits, *Advanced Materials* **24**, 375 (2012).

[149] S. X. Zhang, D. C. Kundaliya, W. Yu, S. Dhar, S. Y. Young, L. G. Salamanca-Riba, S. B. Ogale, R. D. Vispute, and T. Venkatesan, Niobium doped TiO2: Intrinsic transparent metallic anatase versus highly resistive rutile phase, *J. Appl. Phys.* **102**, 013701 (2007).

[150] Y.-H. Chang, C.-M. Liu, Y.-C. Tseng, C. Chen, C.-C. Chen, and H.-E. Cheng, Direct probe of heterojunction effects upon photoconductive properties of TiO2 nanotubes fabricated by atomic layer deposition, *Nanotechnol.* **21**, 225602 (2010).

[151] D. J. Dumin, S. K. Mopuri, S. Vanchinathan, R. S. Scott, R. Subramomiam, and T. G. Lewis, IEEE Trans. Electron Devices, *Nanotechnol.* **4**, 760 (1995).

[152] F. Gonzalez, M. Gritz, C. Fumeaux, and G. Boreman, Two Dimensional Array of Antenna-Coupled Microbolometers, *J. of Infrared and Millimeter Waves* **23**, 785 (2002).

[153] B. Rakos, Investigation of Metal-oxide-metal Structures for Optical Sensor Applications, *Ph.D. Notre Dame* (2006).

[154] J. Bean, THERMAL INFRARED DETECTION USING ANTENNA-COUPLED METAL-OXIDE-METAL DIODES, *Ph.D. Notre Dame* (2008).

[155] M. Bareiss, A. Hochmeister, G. Jegert, G. Koblmüller, U. Zschieschang, H. Klauk, B. Fabel, G. Scarpa, W. Porod, and P. Lugli, Nanoelectronic Device Application Handbook, CRC Press (Taylor & Francis Group) (2009).

[156] S. Barbieri, J. Alton, C. Baker, T. Lo, H. Beere, and D. Ritchie, Imaging with THz quantum cascade lasers using a Schottky diode mixer, *Opt. Expr.* **13**, 6497 (2005).

[157] K. Choi, M. Dagenais, and M. Peckerar, Solar Spectrum Rectification Using Nano-Antennas and Tunneling Diodes, *Proceedings of the SPIE* **7605**, 76050E (2010).

[158] S. K. M. Chin and R. Osgood, *ARL Technical Report* **ARL-TR-5128** (2010).

[159] A. Sanchez, C. F. Davis, K. C. Liu, and A. Javan, The MOM tunneling diode: Theoretical estimate of its performance at microwave and infrared frequencies, *J. Appl. Phys.* **49**, 5270 (1978).

[160] R. Bailey, A proposed new concept for a solar-energy converter, *Eng. Power* **94**, 73 (1972).

[161] T. K. Gustafson and T. J. Bridges, Radiation of difference frequencies produced by mixing in metal-barrier-metal diodes, *Applied Physics Letters* **25**, 56 (1974).

[162] J. G. Small, G. M. Elchinger, A. Javan, A. Sanchez, F. J. Bachner, and D. L. Smythe, ac electron tunneling at infrared frequencies: Thin-film M-O-M diode structure with broad-band characteristics, *Appl. Phys. Lett.* **24**, 275 (1974).

[163] W. Brown, Optimizationof the efficiency and other properties of the rectenna element, *Proc. IEEE-MTT-S Int. Microw. Symp.* (pp. 142–144) (1976).

[164] W. Brown, The history of wireless power transmission, *Solar Energy* **56**, 3 (1996).

[165] E. Wiesendanger and F. Kneubühl, Thin-Film MOM-Diodes for Infrared Detection, *Appl. Phys. A* **13**, 343 (1977).

[166] C. Fumeaux, W. Herrmann, F. K. Kneubühl, H. Rothuizen, B. Lipphardt, and C. O. Weiss, Nanometer thin-film ni-nio-ni diodes for mixing 28 thz co2-laser emissions with difference frequencies up to 176 ghz, *Appl. Phys. B* **66**, 327 (1998).

[167] H. H. Klingenberg and C. O. Weiss, Rectification and harmonic generation with metal-insulator-metal diodes in the mid-infrared, *Applied Physics Letters* **43**, 361 (1983).

[168] H. H. Klingenberg, Properties and bias dependence of metal-insulator-metal point-contact diodes as harmonic mixers in the mid-infrared, *Applied Physics B: Lasers and Optics* **37**, 145 (1985), 10.1007/BF00692077.

[169] A. M. Marks, Device for conversion of light power to electric power, *U.S. Patent* (p. 4445050) (1984).

[170] M. Kale, Electron tunneling devices in optics, *Opt. Eng.* **24**, 267 (1985).

[171] T.-W. Yoo and K. Chang, Theoretical and experimental development of 10 and 35 GHz rectennas, *Microwave Theory and Techniques, IEEE Transactions on* **40**, 1259 (1992).

[172] B. Strassner and K. Chang, Rectifying antennas (rectennas), *Encyclopedia of RF and Microwave Engineering* (p. 4445050) (2005).

[173] S. Masalmeh, H. Stadermann, and J. Korving, Mixing and rectification properties of MIM diodes, *Physica B* **218**, 256 (1996).

[174] C. Fumeaux, J. Alda, and G. D. Boreman, Lithographic antennas at visible frequencies, *Opt. Lett.* **24**, 1629 (1999).

[175] R. Corkish, M. Green, and T. Puzzer, Solar energy collection by antennas, *Solar Energy* **73**, 395 (2002).

[176] B. Berland, Photovoltaic Technologies Beyond the Horizon: Optical Rectenna Solar Cell, *NREL Subcontractor Report* (2001-2003).

[177] D. Goswami, S. Vijayaraghavan, S. Lu, and G. Tamm, New and emerging developments in solar energy, *Solar Energy* **76**, 33 (2004), ¡ce:title¿Solar World Congress 2001¡/ce:title¿.

[178] P. C. D. Hobbs, Laibowitz, R. B, and F. R. Libsch, Ni-NiO-Ni tunnel junctions for terahertz and infrared detection, *Appl. Optics* **44**, 6813 (2005).

[179] P. C. D. Hobbs, R. B. Laibowitz, F. R. Libsch, N. C. LaBianca, and P. P. Chiniwalla, Efficient waveguide-integrated tunnel junction detectors at 1.6 µm, *Opt. Express* **15**, 16376 (2007).

[180] M. Sarehraz, K. Buckle, T. Weller, E. Stefanakos, S. Bhansali, Y. Goswami, and S. Krishnan, RECTENNA DEVELOPMENTS FOR SOLAR ENERY COLLECTION, *Photovoltaic Specialists Conference, 2005. Conference Record of the Thirty-first IEEE* (pp. 78–81) (2005).

[181] S. Krishnan, H. L. Rosa, E. Stefanakos, S. Bhansali, and K. Buckle, Design and development of batch fabricatable

metal–insulator–metal diode and microstrip slot antenna as rectenna elements, *Sensors and Actuators A: Physical* **142**, 40 (2008), ¡ce:title¿Special Issue: Eurosensors XX The 20th European conference on Solid-State Transducers¡/ce:title¿ ¡ce:subtitle¿Eurosensors 2006¡/ce:subtitle¿ ¡xocs:full-name¿Eurosensors 20th Edition¡/xocs:full-name¿.

[182] D. K. Kotter, S. D. Novack, W. D. Slafer, and P. Pinhero, Solar nantenna electromagnetic collectors, *Proc. ASME Conf.* **2008**, 409 (2008).

[183] K. Choi, M. Dagenais, and M. Peckerar, Fabrication of a thin film asymmetric tunneling diode using geometric field enhancement, in: *Semiconductor Device Research Symposium, 2009. ISDRS '09. International*, (pp. 1 –2) (2009).

[184] R. Osgood, B. Kimball, and J. Carlson, Nanoantenna-coupled MIM nanodiodes for efficient vis/nir energy conversion, *Proceedings of the SPIE* **6652**, 665203 (2007).

[185] S. Grover, O. Dmitriyeva, M. Estes, and G. Moddel, Traveling-Wave Metal/Insulator/Metal Diodes for Improved Infrared Bandwidth and Efficiency of Antenna-Coupled Rectifiers, *Nanotechnology, IEEE Transactions on* **9**, 716 (2010).

[186] P. Esfandiari, G. Bernstein, P. Fay, W. Porod, B. Rakos, A. Zarandy, B. Berland, L. Boloni, G. Boreman, B. Lail, B. Monacelli, and A. Weeks, Tunable Antenna-Coupled Metal-Oxide-Metal (MOM) Uncooled IR Detector .

[187] P. M. Krenz, B. Tiwari, G. P. Szakmany, A. O. Orlov, F. J. Gonzalez, G. D. Boreman, and W. Porod, Response Increase of IR Antenna-Coupled Thermocouple Using Impedance Matching .

[188] J. A. Bean, B. Tiwari, G. Szakmany, G. H. Bernstein, P. Fay, and W. Porod, Antenna length and polarization response of antenna-coupled MOM diode infrared detector, *Infrared Phys. Technol.* **53**, 182 (2009).

[189] G. Szakmany, P. M. Krenz, A. O. Olov, G. H. Bernstein, and W. Porod, Antenna-Coupled Thermocouples for Infrared Detection, *11th IEEE Conference on Nanotechnology* **Under review** (2012).

[190] W. Kern and D. A. Puotinen, Cleaning Solutions Based on Hydrogen Peroxide for use in Silicon Semiconductor Technology, *RCA Rev.* **31**, 187 (1970).

Acknowledgment

This thesis has been performed at the Lehrstuhl für Nanoelektronik at the Technische Universität München in close cooperation with the University of Notre Dame in Indiana (USA). I started my research in November 2009 under the principle supervision of Prof. Dr. Paolo Lugli and the supervision of Prof. Dr. Wolfgang Porod in Munich. From June 2011 until August 2011 and in April 2012 I researched at the Notre Dame.

First of all, I want to thank Prof. Dr. Paolo Lugli for giving me as the principle advisor the great opportunity of performing my thesis in this exciting topic at his chair. He always supported me in all fields of research. I am very thankful for his ability to find excellent cooperation partners and his overall project management. His knowledge in a high amount of research topics were always a great support. I always found an open door when having questions or when needing support, not only with respect to research related topics, but also from a social perspective. There is no doubt that without Prof. Dr. Paolo Lugli, my research would not have been gone so far.

I am very grateful for my second advisor Prof. Wolfgang Porod who invited me to work in his facility in the USA. During my thesis, he was always present when there was need for technical or social support regardless of other events or time shifts. He integrated me directly into his group when working in Notre Dame and gave me the unique possibility to get to know fabrication techniques in his great facility. His knowledge in the experimental and theoretical field of rectennas was one reason for the success of this thesis. I cannot imaging having better supervisors than I had in my Ph.D. thesis and I am very thankful for that.

I also want to thank Dr. Giuseppe Scarpa for his administrative support in the frame of the International Graduate School of Science and Engineering (IGSSE).

I thank my students for given me a great support during my research. Especially Andreas Hochmeister who did a great work in the field of structure fabrication using MBE stamps. I also thank Kuan Zhang, and Ken Chin and Kiat Keng from the Singapore Polytechnic.

I want especially thank Dr. Bernhard Fabel and Rosi Heilmann for their technical support in the labs which did also extend into the late evening. But not only with respect to technical aspects I want to thank them, they are two people who knew how create an excellent environment in the university and also further the university. Thank you for that.

I am very glad that I had the possibility to have two such outstanding colleges, Muhammad Atyab Imtaar and Anandi Yadav, who could always help me with

technical and administrative issues. I also enjoyed the time passing together outside the university when getting to know new places in the world.

I special thank has to be send to the "dielectric" group at the Max Planck Institute in Stuttgart. Dr. Hagen Klauk, Dr. Ute Zschieschang, Dr. Frederik Ante, and Dr. Daniel Kälblein are unique in the field of ultra-thin and high quality dielectric films. Their outstanding support could guarantee a fast device development. I felt very well integrated in their group and luckily, we had always a good cake for gaining new energy.

My stay in Notre Dame was outstanding with respect to technical and cultural experiences. Especially Dr. Peter M. Krenz provided great support. He is real expert in doing almost ten lithography steps in the same position on one single chip. But also with respect to antenna related issues, he is a real expert. Gergo P. Szakmany was a great help in the field of Seebeck effect related devices and gave a very valuable help during my thesis. Thank you also to Louisa Schneider and Golnaz Karbasian who created a an excellent environment at Notre Dame.

I also want to thank Prof. Gary H. Bernstein who is a real expert in all fabrication related technologies and paper writing, Prof. Dr. Alexei O. Orlov and Tatyana Orlova. They gave me the possibility to research in Notre Dame and offered me always their help.

Luckily, I was able to work with the best people in the field of device simulation. Thank you Dr. Gunther Jegert and Dr. Christian Jirauschek.

I thank also Omar Fakhr for his ideas and help in transfer printing and related topics. Thanks Omar.

Thank you Daniela Baierl and Tobias Häberle for their support.

Thank you to Prof. Dr. Gregory Timp and Dr. Edward M. Nelson for providing their conductive AFM setup.

Since our new labs have been in the ZNN in Garching, we worked closely together with the people of the Walter Schottky Institute. I want to thank there Dr. Gregor Koblmüller and May Bichler for the fabrication of MBE stamps.

I thank Rupert Huber, Stephan Albert and Prof. Dr. Dirk Grundler, for providing their ALD system for the investigation of thin dielectric layers and for introducing me in their bonding system. During the establishment of the ZNN, they provide me also the possibility to use their plasma system which was essential for my work. Thanks also for the time outside the university.

Further, I thank Armin Exner, Ida Pavlichenko and Prof. Dr. Bettina Lotsch for their help with ellipsometry measurements.

I am deeply thankful for the outstanding support from our secretary´s office. Thank you very much Lucia Weik and Rita von Grafenstein.

Thank you to all technicians of the ZNN, especially Peter Weiser and Hubert Riedl.

Naima Hutter helped me in the formation of SAM on GaAs substrates. Thanks a lot.

A further want to thank to all former and recent members of the Institute for Nanoelectronics for a great time at the chair.

I want to thank International Graduate School of Science and Engineering (IGSSE), the Insitute for Advanced Study (IAS) and the Nanoinitiative Munich (NIM) for their support.

I thank my parents Carmen and Alexander and my brother Kay for their overall support during my whole career at the university in the social support in my whole life.

Finally, I thank my girlfriend Agnes who is always on my side and gave me encouragement during my thesis and during the search for a new job. Thank you very much.

Munich, Oktober 1, 2012.

Statement

Ich erkläre an Eides statt, dass ich die der Fakultät für Physik der Technischen Universität München zur Promotionsprüfung vorgelegte Arbeit mit dem Titel:

Nanodiodes and Nanoantennas Fabricated by Transfer Technology

am Lehrstuhl für Nanoelektronik unter der Anleitung und Betreuung durch Prof. Dr. Paolo Lugli und Prof. Dr. Wolfgang Porod ohne sonstige Hilfe erstellt und bei der Abfassung nur die gemäß § 6 Abs. 5 angegebenen Hilfsmittel benutzt habe.

Ich habe die Dissertation in dieser oder ähnlicher Form in keinem anderen Prüfungsverfahren als Prüfungsleistung vorgelegt.
Die Promotionsordnung der Technischen Universität München ist mir bekannt.

München, den 1. Oktober 2012

gez. Mario Bareiß